# Intelligent Microwaves-Based Modalities for Breast Cancer Detection

by
Maged Aldhaeebi

A thesis
presented to the University of Waterloo
in fulfilment of the
thesis requirement for the degree of
Doctor of Philosophy
in
Electrical and Computer Engineering

Waterloo, Ontario, Canada, 2020

**Examining Committee Membership**

The following served on the Examining Committee for this thesis. The decision of the Examining Committee is by majority vote.

| | |
|---|---|
| External Examiner | Mohamed Bakr<br>Professor |
| Supervisor(s) | Omar Ramahi<br>Professor |
| Internal Member | Raafat Mansour<br>Professor |
| Internal Member | Amir Khandani<br>Professor |
| Internal-external Member | Mustafa Yavuz<br>Professor |

I hereby declare that I am the sole author of this thesis. This is a true copy of the thesis, including any required final revisions, as accepted by my examiners.

I understand that my thesis may be made electronically available to the public.

## Abstract

Breast cancer is considered to be one of the major causes of mortality in women worldwide. Detection of breast tumors in their early stage is the key factor for possible successful treatment and can significantly reduce mortality rates. In recent years, microwaves have emerged as a potential technique for breast cancer detection one that avoids the discomfort, risks and costs associated with x-rays and excessive cost and availability of MRI. Microwave technique is simpler to use, much less expensive to generate, and is non-ionizing. The microwave detection used in earlier works relied on the sharp contrast in the electrical properties between tumors and healthy tissue. In such methods, the breast was scanned by microwaves of various frequencies and the reflection recorded. An image depicting the electrical properties of the breast was then developed. The challenge, however, is that female breasts contain a complex network of fat and fibrous tissues, the electrical properties of which can very well resemble those of cancerous or benign tumors. Also, the electrical properties of the breast vary with frequency, requiring the earlier techniques to employ complex receptors. Motivated by these drawbacks, this thesis addresses the development of an inexpensive, non-ionizing and highly sensitive microwave technique for detecting early-stage breast tumors.

In the first part of this dissertation, anatomically-realistic numerical breast phantom models are constructed using computer simulation technology (CST). The phantoms are anatomically realistic three dimensional (3D) numerical models that are realistic in both structural and dielectric properties.

In the second part of the thesis, first a single electric probe and then a magnetic probe are individually combined with classification algorithms to help in detecting the presence of breast tumors. A key feature of our proposed detection concept is the almost simultaneous sensing of both a woman breasts, since right and left healthy breasts are morphologically and materially identical except amongst very small percentage of women. The two tests then can be compared to reveal any tissues property discrepancies. The concept employs a near-field resonant probe with an ultra-narrow frequency response. The resonant probe is highly sensitive to any changes in the electromagnetic properties of breast tissues, such that the presence of a tumor can be gauged by determining the changes in the magnitude and phase response of the sensor's reflection coefficient. Once the probe response is recorded for both breasts, Principle Component Analysis (PCA) method is employed to emphasize any difference in probe responses. For validation of the concept, tumors embedded in realistic breast phantoms were simulated. To provide additional confidence in the detection modality introduced here, experimental results of three different sizes of metallic spheres, mimicking tumors, inserted inside chicken and beef meat were detected, first by using an

electric probe and then using a magnetic probe, operating at 200 and 528 MHz respectively. The results obtained from the numerical tests and experiments strongly suggest that the detection modality presented here might lead to inexpensive and portable modality for early and regular breast tumor detection.

A novel modality proposed in the third part of the thesis significantly enlarges the sensitivity area beyond that of a single probe. This modality, based on a sensor we developed, relies on a 4-element identical antenna array fed with a single port. The use of this senor array improves the sensitivity area as compared to a single sensor, resulting in better detection of tumors located deeply inside breast tissues. Two different sensors are developed in this part,a dipole sensor and a loop sensor. The dipole sensor comprises a 4-element identical dipole antenna array fed with a single port. Numerical simulations have been conducted using a numerical breast model with and without tumor cells placed in the near-field of the sensor. The sensor is capable of detecting a breast tumor inserted at four different locations and of various sizes. Experimental validation was conducted using chicken meat and metallic and dielectric spheres that resemble healthy and tumourous breast tissues. The simulation and experimental results show that the array sensor has a high sensitivity for detecting various sizes of breast tumor inserted at different locations. The developed loop sensor comprises a 4-element identical loop antenna array fed with a single port. Numerical simulations have been conducted using a numerical breast model with and without tumor cells placed in the near-field of the sensor. The sensor is capable of detecting various sizes of tumor inserted at five different locations. Experimental validation was conducted using a glass box filled with vegetable oil and metallic spheres that resemble healthy and tumourous breast tissues, respectively. The simulation and experimental results show that the array sensor has a high sensitivity for detecting a metallic sphere placed at five different locations inside a dielectric medium as well as for detecting variable sizes of metallic sphere.

In the fourth part of this thesis, a near-field metasurface sensor is introduced whereby a near-field array sensor operating in the microwave regime is used statically to identify the presence of a breast tumor. In a departure from conventional near-field sensors, the sensor is a metasurface comprising an array of 8×8 electrically-small resonating elements. The elements of the metasurface are designed to respond to both electric and magnetic fields. This capability enables the metasurface to emphasize seemingly small changes in the composition of the electric and magnetic fields in its environment, thus leading to higher overall sensor sensitivity. Furthermore, unlike previous near-field probes, the overall metasurface sensor is not electrically small, which means that it provides a larger sensing surface while maintaining the effectiveness of near-field probes in the sense of detecting material changes in the near proximity of the sensor. Numerical and experimental tests

were used to validate the proposed detection methodology. This was achieved by testing the metasurface with a breast phantom having tumor placed at single location at three different stand off distances and with a breast phantom having tumors placed at different locations. Measurements were carried out on a realistic phantom that mimic a real female breast in terms of electric properties. The results showed high sensitivity of the metasurface which can indicate the existence of an anomaly that resembles a tumor inside a breast phantom having inhomogeneous material composition. The advantage of the proposed metasurface sensor array as compared to previously introduced sensors is that the proposed array sensor is fed by a single-feed point. Unlike multiple-feed points sensors, this single feeding port sensor array significantly reduces the computational cost and complexity caused by processing the data from multiple feeds.

The thesis then discusses the idea of using machine learning approaches to improve the performance of the proposed microwave detection system. The machine learning methods proposed discriminated between normal and abnormal breast phantoms in different sizes and classes of breasts, then also significantly improved the accuracy, sensitivity and specificity of the proposed detection system.

As future work, the last part introduces several ideas for solving challenges in various aspects of the proposed sensors and the classification logarithms introduced in the developed system. The first idea is introduced to improve the sensitivity of the metasurface sensor by using multiple polarization sensors. The metasurface sensor, presented in chapter seven has one diploe in the middle of the loop, which will be extended to have two cross dipoles for vertical and horizontal polarization excitations. The second idea is to improve the sensitivity area of the proposed system by using multiple metasurface sensors that cover the whole breast and therefore eliminate the use of mechanical motors to move the sensor all over a breast. The third idea is to develop a portable detection system and integrate of the standalone VNA and the sensor into one miniaturized unit. The VNA circuitry will be positioned at the back of the sensor and will be connected with a laptop.

**Acknowledgments**

In the name of Allah the All-Merciful, The Ever-Merciful.

First and foremost, I would like to thank Allah ,the Almighty, for giving me the strength to successfully accomplish this thesis and for blessing me with great family and friends, whom have been my greatest support in both my personal and professional life.

I want to express my sincere gratitude to my supervisor Prof. Omar M. Ramahi. I cannot thank him enough for his support, guidance, friendly advice and excellent supervision. Thanks to him for the discussions that we had which always sparked novel ideas. I also like to extend my gratitude to my committee members, Prof. Raafat Mansour, Prof. Amir Khandani, Prof. Mustafa Yavuz, and Prof. Mohamed Bakr for spending their time to read my thesis and give valuable comments and feedback.

I like to express my deepest gratitude and appreciation to my dear parents Abdullah Althiipi and Fatima Guiod for their love, support and sincere advice. They supported me in all aspects of this life and I would always be indebted to them. I would also like to thank my siblings, my uncles, my aunts and all my family members for being there for me in hard situations before the pleasant once. My apologies to them for being away for a long time.

Special thanks to my wife and best friend Madihah Guiod. I cannot thank her enough for her continuous support and patience during this journey. Thanks to Allah for blessing me with my cute and lovely children, my sun Abdullah, my daughter Fatima and my sun Malek. They indeed were an important factor in making my life in Canada more enjoyable, especially whenever I come back to my home.

I would like to express my most sincere appreciation towards to my brother and best friend Dr. Thamer S. Almoneef for his unconditional support, patience, endless, guidance and advice, encouragement, professionalism and kindness throughout the last three years have made this one of the most enjoyable and challenging experiences of my life. I will be forever grateful for his guidance and trust in me towards the achievement of this degree. I am also thankful to my brother and best friend Dr. Saeed M. Bamatraf for his enthusiasm, endless, guidance and advice to complete this thesis. The combination of his friendship with his professionalism has been of utter importance to me.

I would like to express my most sincere appreciation towards to my best friend Eng. Alskik Abdullah Bugshan for his unconditional support, patience, endless, guidance and advice. I would like to express my acknowledge to the financial support of Hadhramout Establishment for Human Development, Hadhramout, Yemen. I am sincerely grateful to

the staff in the Department of Electrical and Computer Engineering, UW, in particular Eng. Stephen Utter and Eng. Phil Regier.

I would like to thank my current and former electromagnetic research group members at the University of Waterloo. I am very lucky to be part of this active and friendly group. Specifically, I would like to thank Dr. Hussein Attia, Dr. Zhao Ren, Dr. Khawla Alzoubi, Dr. Miguel Ruphuy, Dr. Abdulbaset Ali, Dr. Faruk Erkmen, Dr. Ahmed Ashoor, Dr. Mohamed El Badawe, Dr. Ali Albishi, Dr. Toa, Maled Olaimat, Dawood Alsaedi, Seyed Mirjahanmardi, Mohammed Aldosari, and Abdurhman Alorien . My apologies to those whom I forgot to mention here. Their friendship will always be remembered.

I would like to acknowledge Prof. Susan Hagness group at the University of Wisconsin for providing the numerical breast phantoms

**Dedication**

To my dear parents and siblings, my beloved Madihah Guiod and my children Abdullah, Fatima and Malek

# Table of Contents

# List of Tables

# List of Figures

# Chapter 1

# Introduction

## 1.1 Background and Motivation

Breast cancer is one of the most common types of cancer among women worldwide. In 2019, the American Cancer Society reported that more than 40,000 women died due to breast cancer in the US [1]. In addition, it is expected that more than 250,000 new cases of invasive female breast cancer patients will be diagnosed in the US [1]. Detecting breast tumors during its early stage of development is a fundamental factor for successful treatment and can significantly reduce mortality rates [1,2]. The most common clinical imaging and detection modalities used for breast cancer detection are X-ray mammography, ultrasound scanning and magnetic resonance imaging (MRI) [2–4].

Mammography is the only USA-FDA approved exam to be used to screen for breast cancer in women with no symptoms. Mammography, however, has recently been subjected to immense scrutiny because of relatively high false negative and false positive results [4]. Furthermore, women who use mammography as a screening test have higher chance of developing cancer because of the ionizing radiation associated with X rays [5, 6]. Discomfort

to women undergoing mammography is another drawback of this imaging technique [7].

Breast ultrasound, which sends high-frequency sound waves to image to the breast tissues. Ultrasound provides excellent contrast resolution; however, it lacks spatial resolution of conventional mammography. Therefore, ultrasound is not approved by the FDA as a screening tool for breast cancer. Rather, ultrasound is used to investigate an abnormality detected by mammography or during a physician performed breast exam [8–10].

MRI is highly sensitive in detecting invasive and small abnormalities compared with mammography and ultrasound and can be used effectively for women with dense breasts. Because breast density shows up as a white region on a mammogram film just as cancer would, it is often difficult to find abnormalities on mammograms if the breasts are dense. However, MRI has been shown to produce a moderate amount of false-positive results. In other words, the results of an MRI sometimes show that a suspicious abnormality is present in the breast when, in fact, cancer is not present. Additionally, the high cost of MRI makes it less available to a large segment of the population [11].

The disadvantages and limitations of the current clinical detection techniques motivated researchers to investigate and develop imaging techniques based on microwaves. Microwaves imaging (MI) and detection modalities present an attractive alternative to the available clinical detection techniques for the primary reason that it requires inexpensive technology and is non-ionizing. The core principle behind all MI modalities is the contrast in the dielectric properties between normal and malignant breast tissues. Therefore, the significant differentiation in the dielectric properties of normal and malignant breast tissues can be used as the underlying principle for detection using electromagnetic waves. Research performed over the past 25 years confirms that malignant breast cancer tumors show sharp variation in their dielectric properties where the value of the permittivity and

conductivity of the tumor tissues are higher than normal (healthy) tissues.

A review of the microwaves-based detection techniques for breast cancer detection is introduced in this chapter. The review focuses on the two types of microwave detection, namely microwave tomography and radar-based techniques. A survey of some clinical prototype systems that developed for breast tumors detection are provided.

## 1.2 Microwave Imaging for Breast Cancer Detection

The concept of using microwaves for breast cancer detection received significant attention and extensive investigation from several research groups over the past two decades, this is mainly due to the several advantages microwave techniques can offer such as inexpensive, non-invasive, non-ionizing, and comfortable treatment [10,12–15]. In addition, microwave imaging techniques provide higher sensitivity and the ability to detect small breast tumors as these techniques are based on the electrical properties contrast between normal and tumors breast tissues [14]. Such detection techniques are based on the hypothesis that the electrical properties, namely the permittivity and conductivity of malignant breast tissues differ from those of the healthy breast tissues within the microwaves band [14, 15]. In literature, there are three modalities that have been explored for microwaves-based breast detection. As seen in Fig. 1.1, these methods can be categorized as passive, hybrid and active methods. [2, 13–16].

In the passive approach, a radiometry device is utilized to measure the differences in temperature between healthy and malignant breast tissues. Tumorous tissues exhibit higher temperature compared to the surrounding normal tissues due to the differences in the electrical properties [16, 17]. Hybrid techniques, which are also known as thermoacoustic methods, employ microwaves sensors and ultrasonic transducers to detect the presence

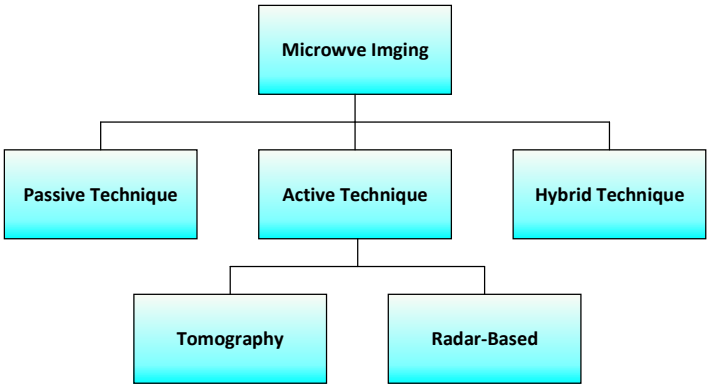


Figure 1.1: Block diagram showing the different modalities that have been explored for microwaves-based breast cancer detection.

of a tumor. In the hybrid techniques, the breast tissues are illuminated by microwaves which are then absorbed by the breast tissue. Malignant tissues significantly absorb more energy than normal tissues and radiate stronger acoustic waves due to their higher electrical conductivity than that of the surrounding normal tissues. An ultrasound transducer located close to the breast then measures the reflected acoustic signals which are then processed to reconstruct an image [16–18]. Active microwaves imaging employs microwaves signals to illuminate the breast tissues. The variation in the dielectric properties between malignant and normal breast tissues is then measured within specific microwaves frequency range [19]. Such technique estimates the backscattered signals from the breast tissues to reconstruct an image which indicates the presence of a tumor by virtue of stronger reflected signals than that of a healthy tissues [19–21].

Techniques for breast cancer imaging using active microwaves methods are extensive, including tomography and radar-based techniques [21–24]. The tomography approach is usually performed iteratively and it can be represented by a nonlinear inverse problem that requires significant computational resources for producing the dielectric properties of the breast.

Imaging of the breast tissues can be constructed from the recovered microwave data file through inverse scattering algorithms that estimate the constitutive parameters of the breast tissues by analyzing the absorbed and reflected microwave signals [25–30]. The radar-based approaches utilize an external microwaves source to illuminate the breast tissues with ultrawideband (UWB) signals. The backscattering signals from the breast are used for detecting breast tumors [31–33].

### 1.2.1 Microwave Tomographic Imaging

Microwave tomography (MT) applies microwave signals that illuminate the breast tissue to reconstruct the permittivity and conductivity of the breast. This approach aims at the complete reconstruction profile of the dielectric properties of the imaged object. It generally leads to an ill-posed nonlinear inverse scattering problem which reconstructs the image by estimating the scattered fields and compares it with the signals obtained from normal breast [34, 35]. MT has been investigated in theoretical and experimental studies for breast cancer detection by several research groups [35]– [40].

MT uses three steps to reconstruct an image of the breast tumors: collecting microwave tomogram data, analyzing the data, and finally displaying the images [35, 36]. The acquisition of the microwaves data is performed by exposing the breast tissue to a microwaves signal and then producing the microwaves tomogram data file. The microwaves tomogram data analysis part is performed by using inverse scattering algorithms that calculate the dielectric properties of the normal and tumor breast tissues from microwave tomogram data files. The data visualizing part is achieved by utilizing 2D or 3D tomogram images that show the presence, location, and size of the tumor [40]. The MT system for breast cancer detection combines both a hardware part which includes microwaves sensors and probes, and a software part that includes image reconstruction approaches and algorithms.

The first clinical prototype for the near-field tomography MI system for breast cancer detection was reported in [38]. The system consisted of a cylindrical array of a transceiving monopole antenna array (16 elements) in the 300-1000 MHz frequency range. The microwave clinical exam was conducted to five women and the scan time sessions have been taken between 10-15 min per breast [38]. Son et al. developed a preclinical prototype MT system for breast cancer detection [39]. In this system, a 16-element circular array is placed into an imaging bath having a matching liquid. Each antenna is used for signal transmission and reception over a frequency band from 500 MHz to 3,000 MHz. A matching liquid was used to fill the MI bath to reduce reflections from the breast surface. The 2D tomography system is convenient for trials on patients and phantoms. The reported prototype system was used to detect a 10 mm tumor inside a phantom at 1700 MHz [39]. In 2016,Jeon et al. introduced a clinical trial prototype MT system for detecting breast tumors. This clinical trial prototype system was designed to work from 3 GHz to 6 GHz with an Fast Forward Solver (FFS) algorithm [40]. The clinical trial prototype system was used for investigating 15 women ranging in age from 40 to 68 years old [40]. Clinical trial results illustrated that a tumor with a size of 25 mm can be detected in the left breast [40].

### 1.2.2 Radar-Based Microwave Imaging

Bridges et al. proposed the first radar-based MI system in 1997 [41]. It avoids using nonlinear inverse scattering algorithms for recovering all the profile of the breast's dielectric properties to construct an image for the breast [41–43]. Bridges' method utilized microwaves signals to illuminate the breast tissues using an antenna array placed at different locations surrounding the breast [41]. The backscattered microwaves signals are then received by the same antennas and processed by radar-based MI methods

to detect the tumor's location and size. These backscattered signals indicate the presence of the tumor because of the contrast in the dielectric properties between the normal and tumor tissue at microwaves frequencies. Radar-based MI techniques involve radar-based MI methods and radar-based MI beam-forming algorithms [42]. Radar-based MI methods are based on different radar configurations that employ elements of an antenna array which transmits or receives (separately or simultaneously) microwaves signals into or from the breast. The beam-forming algorithms are used to reconstruct images from the reflected signals [43].

Radar-based MI techniques can be classified into five approaches: Confocal Microwave (CM), Tissue Sensing Adaptive Radar (TSAR), Microwave Imaging Via Space-Time (MIST), Multi-Static Adaptive (MSA), and Time-Domain Data Adaptive (TDDA) [44].

Klemm et al. introduced a prototype UWB frequency-domain radar-based MI system. The system consists of an aperture array of UWB antennas that are positioned on a section of the hemisphere that conforms to the curved breast shape [45]. The UWB array is positioned with the breast comfortably resting on the spherical shell. The signals are captured by a data acquisition module and transferred to a computer [45]. Clinical imaging results show that the system can detect an 8 mm breast tumor [45].

Zhurbenko et al. reported a radar-based frequency-domain system. The architecture of the system consists of 32 monopole antennas, a measurement unit, a data acquisition system and a computer. The antennas are used to measure the amplitude and phase of the scattered fields in the 3D imaging domain using electronic scanning in the frequency range from 0.3 to 3 GHz [46]. Fear et al. developed a 3D UWB tissue sensing adaptive radar (TSAR) MI prototype system for breast cancer detection which consists of a patient interface employing a padded table with a hole through which the breast drops into a cylindrical container. The mono-static approach is used to collect data and filtering is used to reduce the reflections from the skin

Table 1.1: Summary of some clinical MI studies

| Research group | Scan time | Number of patients | Coupling medium | Antenna array type | Acquisition and Imaging |
|---|---|---|---|---|---|
| Dartmouth College [28, 29, 38] | 5 min | 175 | Yes | Monopole synthetic | Frequency Tomography |
| University of Calgary [47, 48] | 30 min | 8 | Yes | Vivaldi synthetic | Frequency DAS |
| McGill University [49] | 5 min | 13 | Yes | Microstrip stationary | Time DAS |
| Bristol University [50] | 10 S | 267 | Yes | Slot Hardware | frequency IDAS |
| Shizuoka University [51, 52] | 3 min | 2 | Yes | stacked patch Hardware | Frequency DAS |
| Southern University [53] | 4 min | 11 | Yes | Horn synthetic | Frequency DAS |
| Hiroshima [54] University | 5 min | 14 | Yes | Planar slot synthetic | Time DAS |
| London University [55] | 5 min | 45 | Yes | Planar | Frequency |

tissues. In this work, the system was tested on eight volunteers ranging in age from 32 to 47 years [46]. The system was able to detect of 5 mm diameter breast tumor [46]. Summary of some clinical radar-based microwave imaging studies as shown in Table 1.1. The table is subdivided into six categories: the research group, the acquisition and imaging, the scan time, the Maximum number of patients, and the coupling medium.

## 1.3 Research Problem and Contributions

A key interest behind our work here is to provide an alternative detection technique that is not only reliable for early stage cancer detection but especially, inexpensive, comfortable/non-invasive, non-ionizing and highly accessible to a wide sector of the populations in different countries. Therefore, reliability of detection and low cost are two cornerstones of the new modality proposed in this work.

While this work is concerned with the detection of breast cancer, it also related to the specific detection modalities that use microwave-based systems. These modalities have gained significant attention over the past 15 years. The research proposed here builds on the viability of the microwave-based modalities and proposes mitigating the fundamental challenges of these modalities. Therefore, the course of this work is focused on the following:

1. **Introducing** the development of three dimensional anatomically realistic numerical breast - phantoms models in computer simulation technology (CST)
2. **Introducing** the concept of using an electrically-small near-field probe based on a single electric and a magnetic dipole for breast tumor detection.
3. **Developing** an array sensor comprised of 1×4 electrically small printed dipole antennas with identical dimensions excited by a single port for detecting breast tumors at different locations.
4. **Introducing** the concept of developing an array sensor comprised of 1×4 electrically small printed loop antennas with identical dimensions excited by a single port for detecting breast tumors at different locations.

5. **Introducing** the concept of using a metasurface sensor for enhancing the sensitivity area of near-field microwave detection systems.

6. **Examining** the metasurface with a breast phantom having a tumor placed at single location at three different stand - off distances and with a breast phantom having tumors placed at different locations.

7. **Applying** machine learning techniques to accentuate the variance in the sensor's responses for both healthy and tumorous cases.

8. **Examining** the developed metasurface sensor to discriminate between normal and abnormal breast phantoms representing different sizes and classes of breasts phantoms.

9. **Estimating** the accuracy, sensitivity and specificity of the proposed microwave detection system .

## 1.4 Dissertation Outline

The remainder of this dissertation is outlined as follows:

Chapter 2 proposes a novel methodology for using the anonymous breast MRI datasets obtained from the University of Wisconsin online repository for construction of 3D realistic numerical breast phantoms in CST Microwave Studio. The chapter also review the literature on dielectric properties of normal and tumourous breast tissues in the microwave regime .

Chapter 3 and Chapter 4 respectively introduce the concept of using 1) an electric dipole probe and 2) magnetic dipole probe both an ultra-narrow band electrically small with principal component analysis (PCA) technique. The breast tumors exhibit both high permittivity and permeability compared with surrounding healthy breast tissue. The single dipole probe employed is considered as an electric probe, and is highly sensitive

to changes in the permittivity of tumors. This sensitivity is due to the interaction of the confined electric field in the dipole gap with the permittivity of the breast tissues. The single loop probe is considered to be a magnetic-probe, and is highly sensitive to any changes in the conductivity of the breast tissues. The magnetic probe exhibits a higher magnetic field than the electric probe. Because breast tumors exhibit higher conductivity than permittivity values, than those normal in breast tissues, the magnetic probes will be more sensitive than electric probes in detecting tumors.

Chapter 5 presents a methodology to further improve the sensitivity area of the detection system. Using an array of elements instead of a single element enlarges the sensitivity area of the sensor, resulting in covering the whole breast and therefore eliminating the use of mechanical motors to move the sensor all over the breast. Therefore, the sensitivity of the proposed array sensor is based on the aggregate effect of all elements to form one single but highly sensitive sensor. A sensor array comprises of $1\times4$ electrically small printed dipoles antennas of identical dimensions, excited by a single port, is introduced in this chapter. The simulation results show that the array sensor has a high sensitivity for detecting a breast tumor placed at four different locations inside the breast phantom model. Moreover, experimental results show that the array sensor has a high sensitivity for detecting metallic and dielectric spheres placed at five different locations inside a dielectric medium, as well as for detecting variable sizes of spheres.

Chapter 6 introduces a loop array sensor comprised of a 4-element identical electrically small loop antenna array excited by a single port. Numerical simulations have been conducted using a numerical breast model with and without tumor cells placed in the near-field of the sensor. The sensor is capable of detecting a 7 mm breast tumor inserted at five different locations. This experiment was then repeated with other various sizes of tumors. Experimental validation was conducted using a glass box filled with vegetable oil and metallic spheres that resemble healthy and tumors breast tissues,

respectively. The simulation and experimental results show that the array sensor has high sensitivity for detecting a metallic sphere placed at five different locations inside a dielectric medium, as well as for detecting variable sizes of the metallic spheres.

Chapter 7 expands the concept of the array sensor using electrically small elements. In this chapter, the sensor array is a metasurface comprising an array of 8×8 electrically-small resonating elements. The elements of the metasurface are designed to respond to both electric and magnetic fields. This approach enables the metasurface to emphasize seemingly small changes in the composition of the electric and magnetic fields in its environment, thus leading to a higher overall sensor sensitivity. In addition, this chapter presents the idea of testing the metasurface sensor with a breast phantom having tumor placed at single location at three different stand off distances and with a breast phantom having tumors placed at different locations.

Chapter 8 presents a detection technique that combines a machine learning technique with microwave near-field sensors for breast tumor detection. The detection technique consists of two main parts including metasurface microwave near-field sensors and machine learning classification logarithms. The metasurface is extend to the metasurface sensor which introduced in Chapter 7. The sensor, a metasurface comprising an array of 8×8 electrically-small resonating elements, operates at 1.3 GHz.

The proposed technique uses the metasurface sensor to identify the differences between normal and abnormal breasts. Distinguishing between healthy and non-healthy breast is based on estimating the differences in the reflection coefficient of the sensor response for both normal and abnormal breasts. The machine learning methods proposed discriminated between normal and abnormal breast phantoms in different sizes and classes of breasts, then also significantly improved the accuracy, sensitivity and specificity of the proposed detection system.

Finally, the accomplished work, list of publications, and possible future directions are summarized in Chapter 9.

# Chapter 2

# Construction of 3D Realistic Numerical Breast Phantoms in CST Microwave Studio

## 2.1 Introduction

Computational electromagnetic simulations softwares are useful tools to study the interactions of electromagnetic waves with the human breast tissues and improve design concepts related to microwave breast cancer detection and treatment. The advancement in numerical breast phantoms designs improved the effectiveness of computational tools to evaluate new detection or treatment concepts for breast cancer [56, 57].

In this chapter, we used the anonymous breast MRI datasets which were obtained from the University of Wisconsin online repository to build realistic breast phantoms in the computer simulation technology (CST) [58–60]. These phantoms are an anatomically realistic three dimensional (3D) numerical model with dielectric properties derived from the T1-weighted MRI images using a piecewise-linear mapping between MRI voxel intensity and the dielectric properties of the breast.

## 2.2 Anatomy of a female human breast

A healthy human female breast consists of two tissue types including fat tissues (or adipose tissue), and fibroglandular tissues. The fibroglandular is consists of glandular tissue and connective tissue. The healthy human female breast consists of different sections including 15 and 25 lobes, ducts, dilated sections of duct to hold milk, nipple, fat, pectoralis major muscle and chest wall. Fig. 2.1 shows the anatomy of the healthy breast [61, 62].

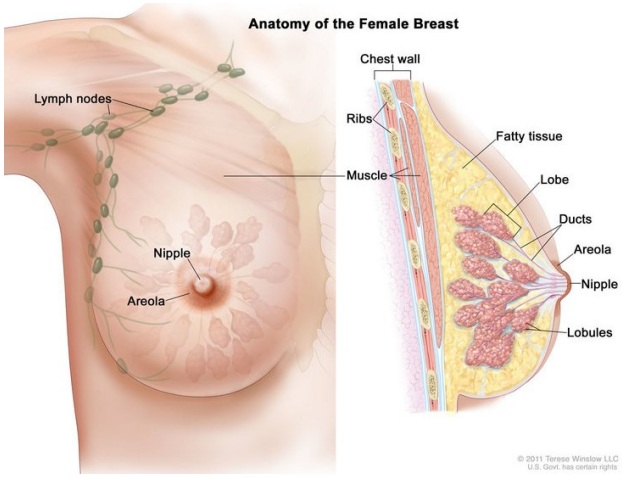


Figure 2.1: The anatomy of a female breast shows the fatty tissue and the glandular lobes. For the National Cancer Institute © 2011 Terese Winslow LLC, U.S. Govt. has certain rights. Used with permission.

Breast tumors can be divided into main two types including benign (Non-invasive) and malignant tumors (Invasive), which defined by an unusually rapid cells growth inside the normal breast tissues. Regarding benign tumors, the growth is controlled whereas the growth is out of control for malignant tumors. There are four Stages of breast tumors which classifies or describes tumors size and tumors spread inside the breast tissues. In the

early stage, the breast tumor is 2 cm or less in diameter and has not yet spread deeply into the chest wall.

## 2.3 Microwave Dielectric Properties of Breast Tissues

Knowledge of the dielectric properties of breast tissues is essential for the understanding of the interactions between the electromagnetic waves and the breast tissues. The dielectric properties of breast tissues are represented by a complex permittivity where the real part represents the ability of the material to store microwave energy whereas the imaginary part, or the loss factor indicates the ability of the material to absorb microwave energy [63].

Microwaves-based detection modalities are mainly based on the observation of high variation of the dielectric properties between normal and tumors breast tissues [64, 65]. Therefore, the significant differentiation in dielectric properties of breast tissues can be used as the underlying principle for a detection method using electromagnetic wave.

Research performed in the past years confirms that breast tumors show sharp variation in their dielectric properties in comparison to nearby healthy breast tissue. Several research groups studied the dielectric properties of normal and tumors breast tissues in the microwaves region. These studies showed that tumors breast tissues have significant differences in their dielectric properties in comparison to surrounding normal breast tissues. [65]–[76].

Based on the dielectric contrast between tumors and healthy breast tissue, the possibility of using microwave for tumors detection was postulated many years ago by Mallard and Lawn [77]. Earlier research claimed that normal breast tissues are mostly homogeneous, whether it has higher fat content or not; therefore, tumors present a dielectric anomaly in the homogeneity which translates into an object with a dielectric contrast.

Campbell and Land [67] studied healthy and cancerous tissues over the frequency of 3.2 GHz [67]. In the most comprehensive, important and most recent study of normal, benign and malignant breast tissue by Lazebnik et al. [70] , exhaustive measurements were performed to conclude that due to the complex network of glandular adipose and fibroconnective tissue in the breast, there is a significant heterogeneity of dielectric properties in normal breast tissue. More specifically, this critical study showed that the contrast in the microwaves dielectric properties between malignant and normal adipose-dominated tissues in the breast is considerable, as large as 10 to 1, while the contrast in the microwaves dielectric properties between malignant and normal glandular/fibroconnective tissues in the breast is no more than about 10%. The study in [70],which is most likely the most comprehensive to date dealing directly with human female breast tissue (unlike other earlier studies which included different mammalian species), shows conclusively that a microwave-based cancer detection scheme that relies on imaging of the dielectric contrast between breast tissues cannot be effective in general.

Table 2.2 gives a chronological summary of several published studies of the dielectric properties' contrast between normal and tumors human breast tissues [65]– [76].

The table is subdivided into four categories: the year of study and the author name, the operating frequency, the probe used in the measurements, and the number of samples. The accuracy of difference between the normal and tumor tissues of each repotted study is based on many factors such as,frequency range for fitting model, tissue type and size, number of sample that used for study, sensing depth and volume, time from excision to measurement of tissues in the study, type of the using fitting data model and the environment of the testing is in vivo or ex vivo states [78]– [82].

In summary, a thorough review of data reported in the literature reveals that the most constant difference between normal and tumors tissues is the

increased water content of the latter. And for this reason the conductivity of tumor tissues at microwave frequencies will be higher than that of normal tissues. As a consequence, at microwave frequencies, tumor tissues will exhibit larger dielectric constant and conductivity profiles than most of normal tissues. Thus, the conclusion of these earlier works is that normal breast tissue is homogeneous, whether it has higher fat content or not; therefore, tumors present an anomaly in the homogeneity and they represent a sharp dielectric contrast object. It is this very fact, namely the dielectric properties change in the cancerous tissues that is the backbone of our proposed detection modality in this study.

## 2.4 Design Methodology

The American College of Radiology (ACR) defines four categories of breast composition according to the radiographic density of breast fibrous and glandular tissues as shown in Table. 2.2 [83, 84].

University of Wisconsin-Madison online repository provided a database of anatomically realistic numerical breast phantoms which accurately mimic both the spatial distribution of the different types of breast tissues including skin, adipose tissue (fat), and fibrous-connective-glandular (ductal and lobular) tissues and the dielectric properties of those tissues relevant to microwave interactions with the phantom [84]. These anatomically realistic breast phantoms are realistic in both structural heterogeneity and dielectric properties information. The information anatomical structure of these breast phantoms is provided using Magnetic resonance images (MRIs). In addition, the normal and malignant breast tissues dielectric properties of these phantoms are provided by large-scale dielectric study of the University of Wisconsin and the University of Calgary [58, 59, 85].

We used the database of anatomically realistic the breast phantoms which

were obtained from the University of Wisconsin UWCEM online repository to build the breast phantom in the computer simulation technology (CST). Each realistic numerical breast phantom consists of a 3D grid of cubic voxels, where each voxel is 0.5mm x 0.5mm x 0.5mm. Each phantom has data set of three ASCII text files including breastInfo.txt, mtype.txt, and pval.txt. [59]. The breastInfo.txt file provides the basic information about the numerical phantom,dimensions of the grid in units of grid cells ["s1", "s2", "s3"], and the classification of breast composition. The mtype.txt file contains data of different voxels in the grid. The pval.txt file provides the dielectric properties of the breast phantom [59].

To import the numerical breast phantoms using the database from the University of Wisconsin repository into Computer Simulation Technology (CST) Microwave Studio following procedures are used:

1. Generate a voxel file which contains the material numbers using MATLAB [86].
2. Generate a material file that maps material numbers.
3. Generate a Visual Basic macro file containing material redefinitions for each of the numbered material types to include frequency-dependent dielectric properties.
4. Import the generated 3D breast voxel model into CST Microwave Studio.

MATLAB software is used to generate the voxel file, the material file and the macro file to integrate the breast phantoms into CST [86]. The material file is generated by using the single Cole-Cole model equation for the frequency-dispersive tissues properties as shown below.

$$\epsilon(\omega) = \epsilon^{'}(\omega) - j\epsilon^{''}(\omega) = \epsilon_{\infty} + \frac{\Delta\epsilon}{1 + (j\omega\tau)^{1-\alpha}} + \frac{\sigma_s}{j\omega\epsilon_o} \tag{2.1}$$

where $\omega$ is the angular frequency, $\epsilon^{'}(\omega)$ is the frequency-dependant dielectric constant, $\epsilon^{''}(\omega)$ is the frequency-dependant dielectric losses and $\epsilon_o$ is the free space permittivity. The $\epsilon_\infty$, $\sigma_s$, $\tau$ and $\alpha$ are the Cole-Cole model parameters obtained from the clinical experimental data. The breast model has the physical shape of a real human female breast. Moreover, with a high resolution of 0.5 mm, the model also includes the following eight tissue types: skin, muscle, glandular-1,2,3, and fat-1,2,3 [59, 84].

Fig. 2.2 shows the four American College of Radiology classes of breast density of the numerical breast phantoms fatty, scattered fibroglandular, heterogeneously dense, and extremely dense in a cross section of an MRI-derived model highlighting the correlated distribution of tissue within the breast integrated in CST. The color visualizations show the permittivity grid for the reconstruction where the adipose (blue) and fibroglandular (red/ orange) regions of the heterogeneous interior of the phantoms.

In order to investigate the detection of the breast tumors in the realistic environments, we inserted different sizes of the breast tumors at different locations inside the developed healthy breast phantoms. The tumors's dielectric properties were obtained from cancer surgery as documented in [70, 84, 86] as shown in Fig. 2.3.

## 2.5 Conclusion

We constructed and integrated four classes of three dimensional (3D ) anatomically realistic numerical human female breast phantoms in the CST full wave simulation. The realistic phantoms are an anatomically realistic (3D) numerical model with dielectric properties derived from T1-weighted MRI images using a piecewise-linear mapping between MRI voxel intensity and the dielectric properties of the breast. The 3-D realistic numerical human female breast phantoms have been utilized for investigating a new

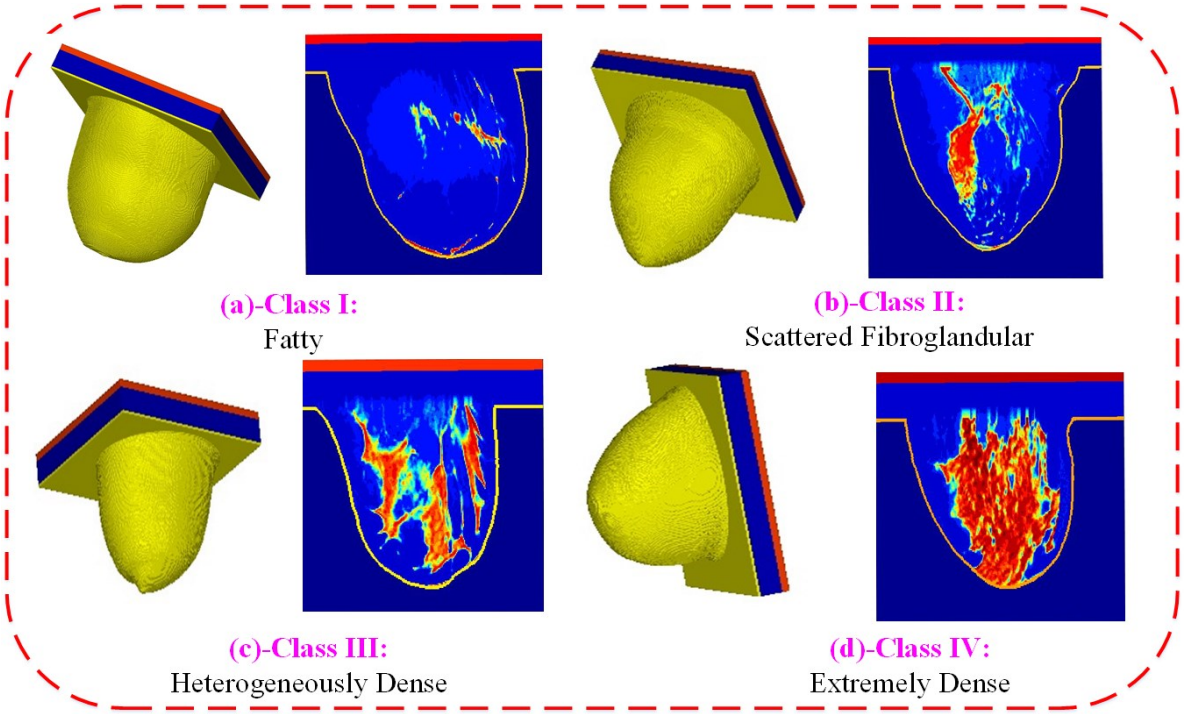


Figure 2.2: Representative numerical healthy human female breast phantoms from the University of Wisconsin repository. The phantoms represent the four American College of Radiology classes: (a) fatty, (b) scattered fibroglandular, (c) heterogeneously dense, and (d) extremely dense. (a) Three-dimensional view. (b) z cross section. The color visualizations show the permittivity grid for the reconstruction where the adipose (blue) and fibroglandular (red/ orange) regions of the heterogeneous interior of the phantoms.

microwave technique for breast cancer detection.

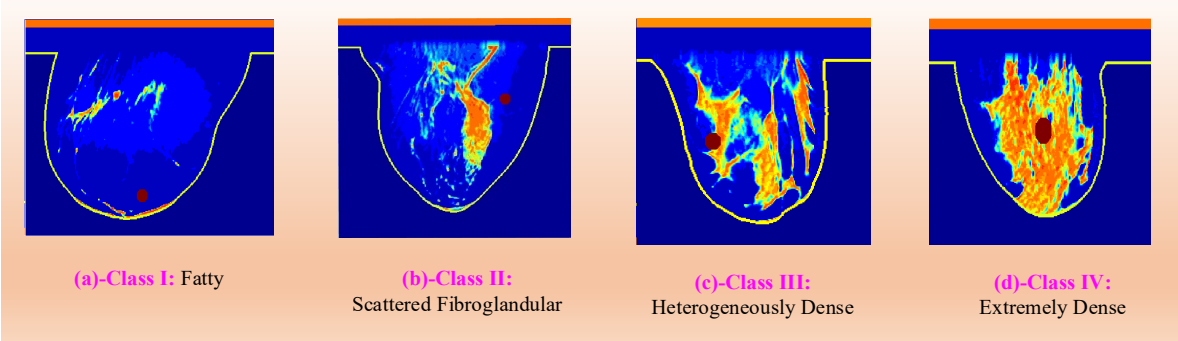


Figure 2.3: Representative numerical abnormal human female breast phantoms view from xy plane. The phantoms represent the four American College of Radiology classes of breast density : (a) fatty, (b) scattered fibroglandular, (c) heterogeneously dense, and (d) extremely dense. The color visualizations show the permittivity grid for the reconstruction where the adipose (blue) and fibroglandular (red/ orange) regions of the heterogeneous interior of the phantoms

.

Table 2.1: Chronological Summary of Several Studies of the Dielectric Properties of Human Female Breast Tissues.

| Year and Author | Frequency Range | Probe Type | Number of Samples (patients) |
|---|---|---|---|
| 1984 Chaudhary et al. [65] | 3 MHz-3 GHz | Open-ended coaxial probe | 15 |
| 1988 Surowiec et al. [66] | 20 KHz-100 MHz | End-of-the-line capacitive probe | 7 |
| 1992 Campbell and Land [67] | 3.2 GHz | Resonant cavity probe | 37 |
| 1994 Joines et al. [68] | 50-900 MHz | Flat-ended coaxial probe | 12 |
| 2004 Choi et al. [69] | 0.5-30 GHz | Open-ended coaxial probe | 12 |
| 2007 Lazebnik et al. [70] | 0.5-20 GHz | Open-ended coaxial probe | 196 |
| 2009 Halter et al. [71] | 100 Hz-8.5 GHz | Electrical Impedance Spectroscopy probe | 6 |
| 2014 Sugitani et al. [72] | 1-6 GHz | Open-ended coaxial probe | 102 |
| 2015 Martellosio et al. [73] | 0.5-50 GHz | Open-ended coaxial probe | unspecified |
| 2017 Martellosio et al. [74] | 0.5-50 GHz | Open-ended coaxial probe | 220 |
| 2018 Cheng et al. [75] | 0.5-8 GHz | Open-ended coaxial probe | 509 |
| 2019 Hussein et al. [76] | 200 MHz- 13.6 GHz | Open-ended coaxial probe | 48 |

Table 2.2: The four classes of numerical breast phantom according to their radiographic density

| Class | Name of Phantom | Percentage of Glandular Tissue |
|---|---|---|
| 1 | Mostly fat | $< 25\%$ |
| 2 | Scattered fibroglandular | 25% -50% |
| 3 | Heterogeneously dense | 51%-75% |
| 4 | Very dense | $> 75\%$ |

# Chapter 3

# Near Field Breast Tumor Detection Using Ultra-Narrow Band Electric Probe with Machine Learning Techniques

## 3.1 Introduction

In this chapter, we propose a near-field microwave sensing modality that uses a single probe combined with a classification algorithm to help in detecting the presence of tumors in the human female breast. The concept employs a near-field resonant probe with an ultra-narrow frequency response. The resonant probe is highly sensitive to the changes in the electromagnetic properties of the breast tissues such that the presence of the tumor is gauged by determining the changes in the magnitude and phase response of the sensor's reflection coefficient. A key feature of our proposed detection concept is the simultaneous sensing of tissue property changes to the two female breasts since the right and left healthy breasts are morphologically and materially identical. Once the probe response is recorded for both breasts, the Principle Component Analysis (PCA) method is employed to emphasize the

difference in the probe responses. For validation of the concept, tumors embedded in a realistic breast phantoms were simulated. To provide additional confidence in the detection modality introduced here, experimental results of three different sizes of metallic spheres, mimicking tumors, inserted inside chicken and beef meat were detected using an electrically-small probe operating at 200 MHz. The results obtained from the numerical tests and experiments strongly suggest that the detection modality presented here might lead to an inexpensive and portable early and regular screening for breast tumor.

## 3.2 Microwave Sensors for Microwave Breast Detection Systems

Developing microwave sensors is an important part of designing the microwave detection system for breast cancer detection. The microwave detection system employs microwave sensors to transmit microwave signals to illuminate the breast tissues and measure the backscattered reflection signals from the breast under test [15].

The microwave sensors should meet the specific design requirements, including operating frequency, directivity, sensitivity, accuracy, and compact size. Design the microwave sensor at specific operating frequencies for the MI system is a significant task due to higher frequencies the attenuation of microwave signals increases which case a lower penetration depth. Several antennas have been developed as microwave sensors for breast cancer detection, including dipole antennas, patch antennas, dielectric resonator antennas, slot antennas, horn antennas, Vivaldi antennas, open-ended coaxial probes, tapered slot antennas (TSAs), bow-tie antennas, and monopole antennas [10, 15, 44].

Near-field (NF) microwave probes that are sensitive to the electromag-

netic properties of materials are actively applied to medical imaging devices. The most important feature in a microwave near-field probe is its ability to confine the fields to regions that are significantly smaller than the wavelength of the operating frequency of the probe as well as having the advantage of larger penetration depth. Therefore, microwave near-field probes are able to resolve sub wavelength features, improving the overall resolution. [87, 88]

Several studies developed NF microwave probes that have been used for detection. The work by Ren et al has introduced a near-field antenna probe based on the concept of enhancing the evanescent fields with the primary objective of detection using split-ring resonators [89]. A tapered rectangular waveguide probe was used for cancer detection [90]. Zhang et al proposed a parallel-plate waveguide probe for non-invasive breast cancer detection [91].

## Probe design and simulation

The probe used in this chapter is a dipole antenna small enough to confine most of the near-field radiation into the breast tissue to increase its sensitivity to variation in the dielectric properties of the tissues that are interrogated. Other types of antennas could be used such as loops or even patch antennas. However, we emphasize that the specificity of the probe topology is not of prime interest here but rather the entire system concept. Nevertheless, study of the sensitivity of different probes will be considered in a future separate study. For sufficient field penetration into the breast tissue, the operating frequency must be chosen carefully to ensure enough penetration level inside the dense breast. Without loss of generality, we select the frequency of operation to be 200 MHz which ensures sufficient field penetration in the human female breast.

The probe was designed as a printed dipole of length 92 mm and trace

width of 2 mm hosted on a RO4003 Rogers material with a thickness of 1.52 mm and a dielectric substrate of a relative permittivity of $\epsilon_r$=3.38 as shown in Fig.3.1. The electrical length of the dipole is $\lambda/12$, (where $\lambda$ is the wavelength in free space) which makes its radiation efficiency very low implying a flat, or near unity reflection coefficient ($S_{11}$) response, which in turn, makes it highly insensitive to breast material changes. To enable the probe to be highly sensitive, the probe must be made an efficient radiator which leads to a highly defined ultra-narrow band-stop filter response by using a lossless matching network. The network was designed using the full-wave numerical simulation tool CST Microwave Studio [60]. The optimized matching network consisted of a series and parallel inductors having inductances of 0.36 uH and 0.49 uH, respectively with specific placement of the elements as shown in Fig.3.1(a). We emphasize that both the values of the inductors and their location and orientation were optimized using CST.

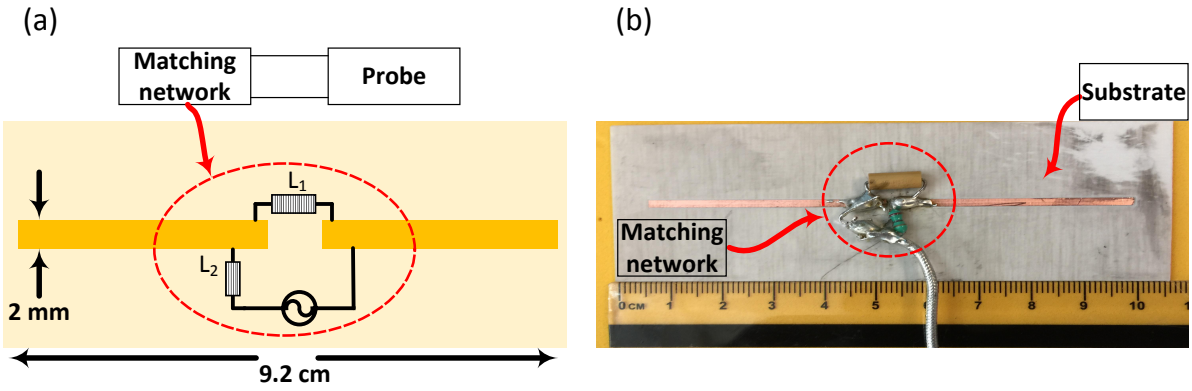


Figure 3.1: The printed electrically-small probe hosted on a dielectric substrate. (a) Schematic showing probe and the location of the matching network elements, where L1 and L2 are inductances of values of 0.36 uH and 0.49 uH respectively. (b) Photo of the fabricated probe and the matching network.

The probe was fabricated and tested yielding strong agreement between the measurements and the simulations as can be observed from Fig. 3.2. Specifically, the agreement was very strong for the resonance frequency but

we observe a deviation in the bandwidth which we attribute to non-ideal behavior of the elements and particularly the dispersive nature of all material involved in the fabrication of the probe (for instance, the inductance of real inductors is frequency dependent whereas the simulated ones have frequency independent inductance). The slight broadening of the bandwidth of the fabricated (real-world) probe in comparison with the ideal (numerical) probe has the advantage of providing additional features that enhance the detection discrimination when using the principle component analysis as will be shown below.

The proposed probe was then simulated with a breast phantom which constructed in CST in chapter two to test its ability to detect the presence of tumors. The model used in this chapter without loss of generality, the model used in this work is the Heterogeneously Dense Breast ID: 062204" ACR classification: Class 3. The model has $0.5 \times 0.5 \times 0.5$ resolution with $219 \times 243 \times 273$ voxels.

The probe was calibrated with the numerical realistic breast phantom where the proposed probe is placed at a distance of 5 mm away from the healthy breast phantom as shown in Fig. 3.3(a). The magnitude and phase of the reflection coefficient of the probe were then recorded at 201 different frequencies spanning the range 100 to 300 MHz. Next, a tumor is inserted inside the same breast phantom with three different diameter sizes namely: 9 mm, 13 mm, and 17 mm, as shown in Fig. 3.3(b). The tumor's dielectric properties were obtained from cancer surgery as documented in [70]. The magnitude and phase information were then recorded for the breast with the tumor. The data is then analysed with and without the tumor to decide whether or not a tumor is present.

The key aspect of the tumor detection modality introduced here is based on two findings. The first is the material and topological symmetry between the two healthy breasts of a woman [92, 93]. The second is the unlikelihood that a woman would develop breast tumors in both breasts at the same

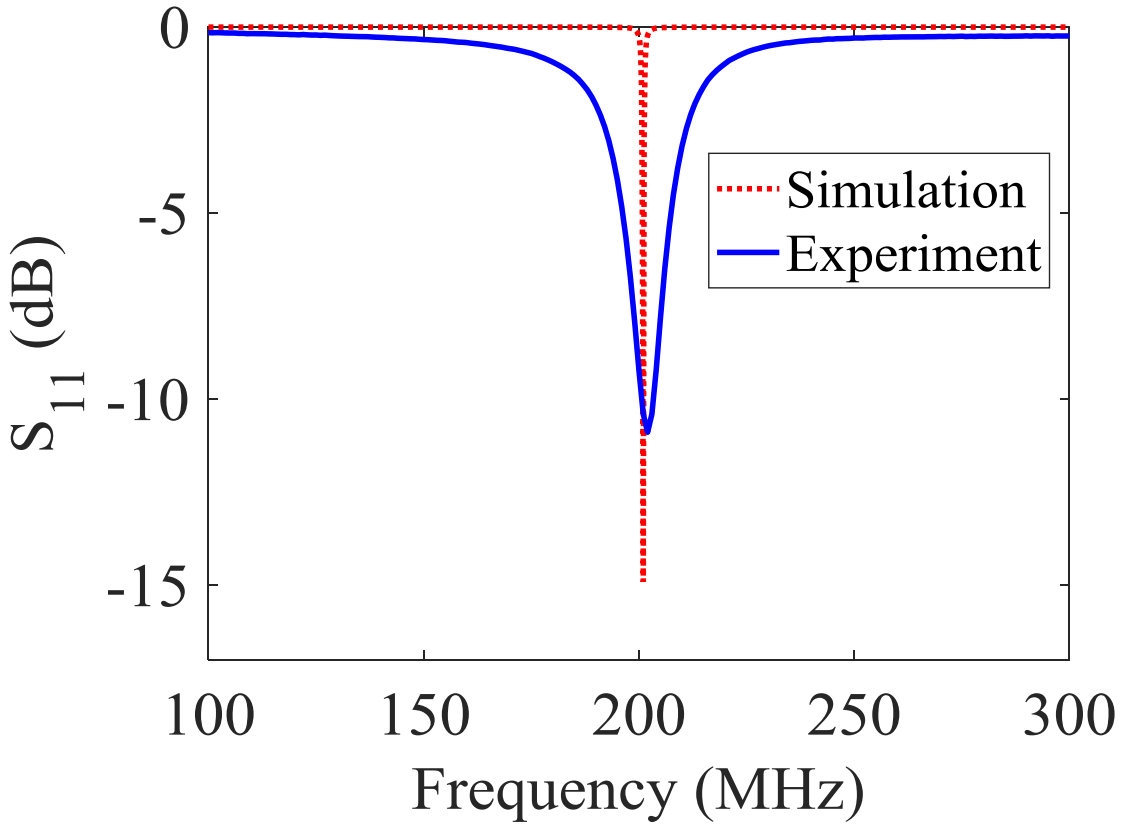


Figure 3.2: Response of the probe over the 100-300 MHz frequency band. The broadening of the bandwidth in the measurements arises form the dispersive nature of the material and circuit elements used in the construction of the probe.

time and the unlikelihood that a woman would develop identical breast tumors in both breasts at the same time [93]. The detection modality introduced here calls for the detection test to employ two identical probes positioned symmetrically with respect the two breasts. The responses of the two probes were then recorded (phase and magnitude of the reflection coefficients) and processed using the PCA method to decide whether or not a tumor is present. If the response of the probes from both breasts are

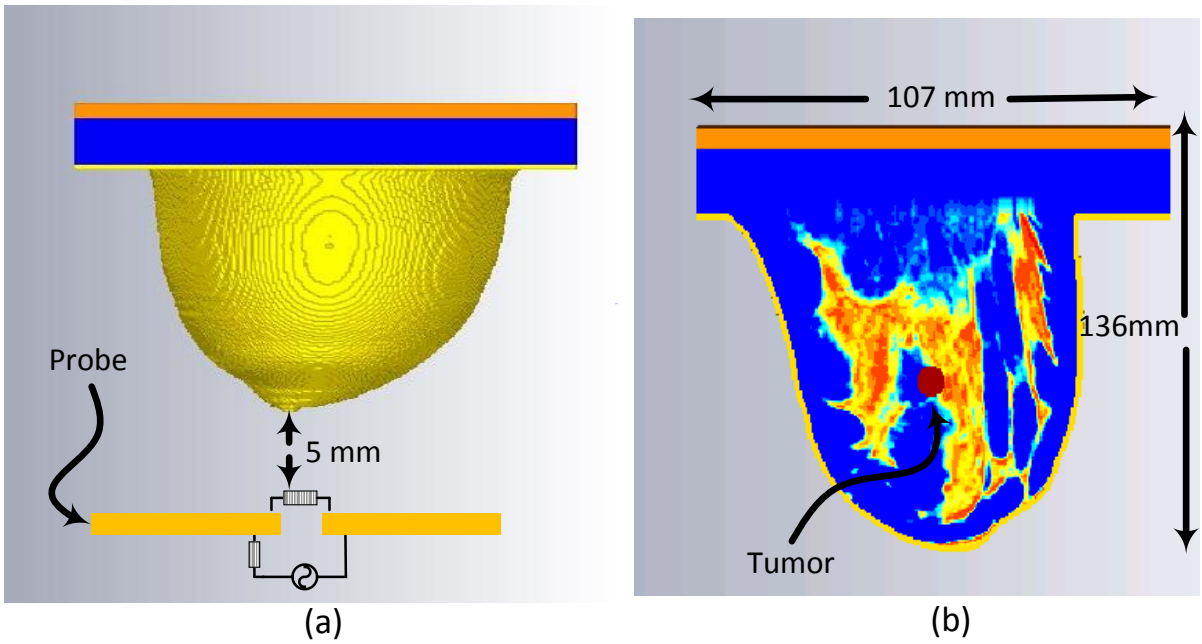


Figure 3.3: Simulation setup: (a) Ultra-narrow band probe with a stand-off distance of 5 mm from a 3D realistic numerical breast phantom model. (b) The embedded tumor in the numerical breast phantom.

identical, then the woman breasts are most likely free of tumors; otherwise, there is a likelihood of the presence of a tumor that can be either benign or cancerous. We fully realize that a discrepancy between the two does not conclusively determine which breast contains the tumor. Nevertheless, it is conceived that when such a device is realized, the outcome of such tests allows the healthcare provider to refer the women to additional screening using more expensive techniques if needed.

In the proposed detection method, the scattering parameters of the probe which contain the magnitude and phase features are extracted. Here, the feature vectors prior to applying the PCA analysis method are the magnitude and phase of reflection coefficient of the probe (the S11 or the scattering parameter of the probe). The feature vectors are then tabulated in

a table containing 3 columns and 201 rows (not included in the paper for brevity). Each discrete value of the magnitude and phase changes with the frequency response. The magnitude and phase of the reflection coefficient of the probe were recorded at 201 different frequencies spanning the range 100 to 300 MHz. The two feature vectors: the magnitude and phase have dimensions of 201 rows and 3 columns. The first feature, the magnitude, is described by the first and second column which contains the frequency and magnitude points, respectively. The second feature, the phase, is described by the first and third column which comprises the frequency and phase points, respectively. The data was then entered into the PCA analysis method code to indicate the presence of a tumor inside a breast.

Next,we employ the PCA method to reduce the dimensionality of the problem by implementing a vector space transform [94]. The objective of PCA is to extract critical information from the scattering parameter response data set and to express this information as a set of orthogonal variables called principal components [94]. The eigen-decomposition of positive semi-definite matrices and the singular value decomposition of rectangular matrices are used for finding the principal components. [94]. Thus, via mathematical projection, high dimensional original datasets can be reduced to small number of variables without losing much of the original information to analyze trends, patterns and outliers [95].

Once the probe response of the two probes are recorded (mimicking the scenario where a single probe is used for each of the two breasts), the PCA feature extraction method is applied for both the healthy and the tumourous cases. The results of Fig. 3.4(a), Fig. 3.4(b) the magnitude of $S_{11}$ using PCA, Fig. 3.4(c) the phase of $S_{11}$ and Fig. 3.4(d) the phase of $S_{11}$ using PCA show that the probe is capable of detecting breast tumors as small as 9 mm. Clearly the probe is more sensitive to larger tumor sizes as indicated by the more pronounced separation between the cases with and without tumors. We also observe that for the 9 mm tumor, the magnitude response

was more effective than the phase response in the sense of providing higher discrimination.

## Experimental Validation

In light of the preliminary and encouraging simulation results obtained above, an experiment was carried out to test the feasibility of the proposed concept in an environment that have resemblance to female breast tissues. The experiment setup consisted of the proposed electrically-small dipole probe, a keysight 8.5 GHz VNA, metallic spheres with different diameter sizes (mimicking a tumor), chicken breast tissue and a slice of a beef steak. The experiment apparatus was contained in a wooden box with an opening in one of the box sides to allow for easily placing and changing the position of the material under test inside the box as shown in Fig. 3.5. The experiment was performed inside an anechoic chamber to ensure that no energy is bouncing back from the surrounding environment and effecting the measured probe response.

Initially, the material under test is scanned horizontally at 6 different positions as shown in Fig. 3.6(a). The main reason for performing such a scan is to determine the location where the probe sensitivity is highest (highest sensitivity refers to the highest shift experienced by the magnitude and phase of the $S_{11}$ of the probe when compared to the original case). For instance, the $S_{11}$ of the probe in the presence of an object placed at the edge of the dipole probe compared to that of the same object placed at the center of the probe is quite different. This is mainly due to the fact that a high electric field is confined within the gap of the dipole at the resonance frequency. When an object is placed in the vicinity of the gap, the probe's response experiences higher shift in both the magnitude and phase than the case where the object is placed further away from the gap. Hence, the

probe is highly sensitive to an object placed above or close to the gap. Once the position of highest sensitivity was found, (see Fig. 3.6(a)), the probe response was then recorded for this high sensitivity position. Although, the middle of the probe experienced the highest sensitivity, other locations away from the gap have a reasonable shift which can lead to a successful differentiation between the normal and the tumor breast tissue. Therefore, In a real-world detection scenario, the patient can position the probe in any location in front of the breast to perform the self examination.

Next, three different tests were performed: 1) with chicken breast, 2) a slice of beef, and 3) a hybrid of both. In each test, two main variables were changed. First, multiple metallic spheres, which will be embedded inside the material under test with different diameter sizes were used. Three different diameter sizes were used: 9 mm, 13 mm, and 17 mm to test the ability of the probe to detect various tumor sizes. For each tumor size, two different stand-off vertical distances were used as shown in Fig. 3.6(b). In the experiment, the scattering parameters seen from the port of the probe were recorded for both the phase and the magnitude. The phase and magnitude of the scattering parameters were analyzed with and without the PCA method for two vertical distances of 5 mm and 10 mm as shown in Fig. 3.6(b). The results are presented in Fig. 3.7 and Fig. 3.8. It is evident from the results that the plots of the reflection coefficient of the probe in the presence of the metallic sphere for both the magnitude and phase as shown in Fig. 3.7(a), Fig. 3.7(c), Fig. 3.8(a) and Fig. 3.8(c), experience a very slight shift that is hard to detect for the various locations labelled 0 - 5 (see Fig. 3.6(a)). Here, the difficulty in detecting the difference between the tumerous breast compared to a healthy one refers to the fact that a human eye cannot easily distinguish the change in either the magnitude or the phase of the probe. Additionally, by direct inspection of the magnitude and phase of the reflection coefficient, it is extremely difficult, if not impossible, to differentiate the healthy breast from the tumourous one, even if the

process is automated, without additional classification procedure. However, when the data were plotted using the PCA method as shown in Fig. 3.7(b), Fig. 3.7(d), Fig. 3.8(b) and Fig. 3.8(d), a clear and obvious distinction is observed between the healthy breast tissue (no sphere) compared to that of the malignant case (with an embedded sphere).

For the first experiment a chicken breast which includes skin, fat and meat was used as a testing material. The chicken was positioned at the fixed horizontal distance labeled 3 in Fig. 3.6(a). Then the magnitude and phase of the probe were extracted with two stand-off distance, namely 5 mm and 10 mm, as shown in Fig. 3.6(b). The experiment was then repeated after inserting a metallic sphere inside the same chicken breast. Please note that during the experiment, we labeled the location where the spheres were embedded inside the chicken to ensure a fair and identical comparison. The results obtained from this experiment is shown in Fig. 3.9. The second experiment was conducted with a slice of meat instead of chicken to test the strength of the probe to detect the variation inside the material with different electrical properties. Similarly, the test was done for different stand-off distances and different sphere sizes. The results obtained from this case is shown in Fig. 3.10. In the last experiment, a hybrid medium consisting of a chicken breast sandwiched between two slices of meat were used to test material with higher degree of heterogeneity than the previous two cases. The results are plotted in Fig. 3.11.

In all of the three experiments, the PCA analyzer provides a spatial separation between the normal and tumorous cases. In addition, it is noticeable that as the tumor size increases, the separation between the normal and the tumorous case increases, which indicates a more pronounced detection. Moreover, the separation between the cases with and without the tumor is more pronounced for the magnitude as compared to the phase of the $S_{11}$ of the probe, which is similar to the behavior observed when interrogating the numerical breast phantom.

## Discussion

Since the realistic female breasts are of a hemispherical shape, is it critical to test the ability of the probe to detect tumors located at varies positions within a curved shape breast model. Therefore, an experiment was conducted consisting of a chicken meat placed on a Styrofoam of a hemispherical shape. Then a 9 mm metallic sphere was inserted in three locations consecutively inside the breast as shown in Fig. 3.12 (b). The probe was then placed at a distance of 5 mm and 10 mm away from the breast. The experimental results are summarized in Fig. 3.13 (i) and Fig. 3.13 (ii) for a distance off of 5 mm and 10 mm respectively. Fig. 3.13 (a) and Fig. 3.13 (b) show the magnitude and phase of $S_{11}$ at distance off 5 mm respectively. Fig. 3.13 (c) and Fig. 3.13 (d) show the magnitude and phase of $S_{11}$ at distance off 10 mm respectively. It is evident from the results that there is a clear distinction in the magnitude and phase of the probe between the breast without tumor and the breast with tumor for all of the three locations. In the experiment, the locations of the tumors were selected to cover the outer peripheral and the middle parts of the breast. Such experiment proves the ability of the probe to detect tumors placed at different locations of a breast having a hemispherical shape regardless of the location of the tumor within the breast.

In all of the experiments performed thus far, we used metallic spheres to represent a tumor inside a breast. This is due to the fact that our main objective is to test the ability of the proposed probe to detect the dielectric variation within the breast. To study the ability of the probe to detect a realistic tumor which is not purely conductive, an experiment was conducted using tumors made of an oil and gelatine mixture as shown in Fig. 3.14. Such mixture is proven to yield dielectric properties similar to that of a realistic tumor [96–99].

The experimental procedures used for the high conductivity sphere was

repeated for the lossy dielectric spheres. We inserted a 9 mm high dielectric sphere at the same three different locations inside the hemisphere breast chicken. The probe response of the two testing without and with tumor at the different locations are recorded at standoff distance of 5 mm and 10 mm. Then the probe response was analyzed using the PCA as shown in as shown in Fig. 3.15. Fig. 3.15 (i) and Fig. 3.15 (ii) show the magnitude and phase of S11 at distance off 5 mm and 10 mm respectively. Fig. 3.15 (a) and Fig. 3.15 (b) show the magnitude and phase of $S_{11}$ at stand off 5 mm respectively. Fig. 3.15 (c) and Fig. 3.15 (d) show the magnitude and phase of $S_{11}$ at stand off 10 mm respectively.

In the last experiment, three different diameter sizes 9 mm, 13 mm and 17 mm of high conductive and high dielectric spheres were embedded inside the chicken meat. Two different measurements were conducted using spheres made of metal and the oil gelatine mixture. In both measurements, the probe was placed at two standoff distances, 5 mm and 10 mm, away from the phantom. The results are shown in Fig. 3.16 and Fig. 3.17 for both the metallic based tumor and the oil-gelatine based tumor, respectively.

Fig. 3.16 (i) and Fig. 3.16 (ii) show the magnitude and phase of $S_{11}$ of the three high conductivity sphere sizes at standoff of 5 mm and 10 mm respectively. Fig. 3.16 (a) and Fig. 3.16 (b) show the magnitude and phase of S11 at distance off 5 mm respectively. Fig. 3.16 (c) and Fig. 3.16 (d) show the magnitude and phase of S11 at distance off 10 mm respectively. Fig. 3.17 (i) and Fig. 3.17 (ii) show the magnitude and phase of $S_{11}$ of the three high dielectric sphere sizes at standoff of 5 mm and 10 mm respectively. Fig. 3.17 (a) and Fig. 3.17 (b) show the magnitude and phase of $S_{11}$ of the three high dielectric tumor sizes at stand off 5 mm respectively. Fig. 3.17 (c) and Fig. 3.17 (d) show the magnitude and phase of $S_{11}$ at stand off 10 mm respectively. From the results, it is clear that the probe can detect the metallic based tumor and the oil-gelatine based tumor with different diameter sizes. From the results, it is clear that the probe can detect the

metallic sphere and the oil-gelatine spheres with different diameter sizes.

## Conclusion

In this chapter, an alternative microwave modality for breast tumor detection using a single electric probe for each of the two human female breasts is presented . The sensing mechanism is simple and has the advantage of providing portability and comfort for the user. Our numerical results have demonstrated the ability of sensing a tumor that is as small as 9 mm buried inside breast tissues. In addition, experimental results show the high sensitivity of the probe which can detect the presence of a tumor inside a chicken breast having inhomogeneous dielectric variations. The feature extraction algorithm, the principle component analysis, was used to enhances the changes in the scattering parameters of the probe which aid in distinguishing between a healthy and tumorous breast.

The sensing modality conceived here is sharply different from other microwaves-based modalities that were based on reconstructing the dielectric properties profile of the breast. The modality presented here is fundamentally based on the complex interaction between the near-field of an electrically-small probe and the highly heterogeneous human female breast. The overall detection schemed is intended to provide women with regular initial stage breast tumor screening that is portable and comfortable. In this work, the feasibility of the concept was demonstrated by using human female breast phantoms and experimentally using chicken and beef tissues. Future work will focus on replacing the measurements' devices with compact circuits to ensure full portability.

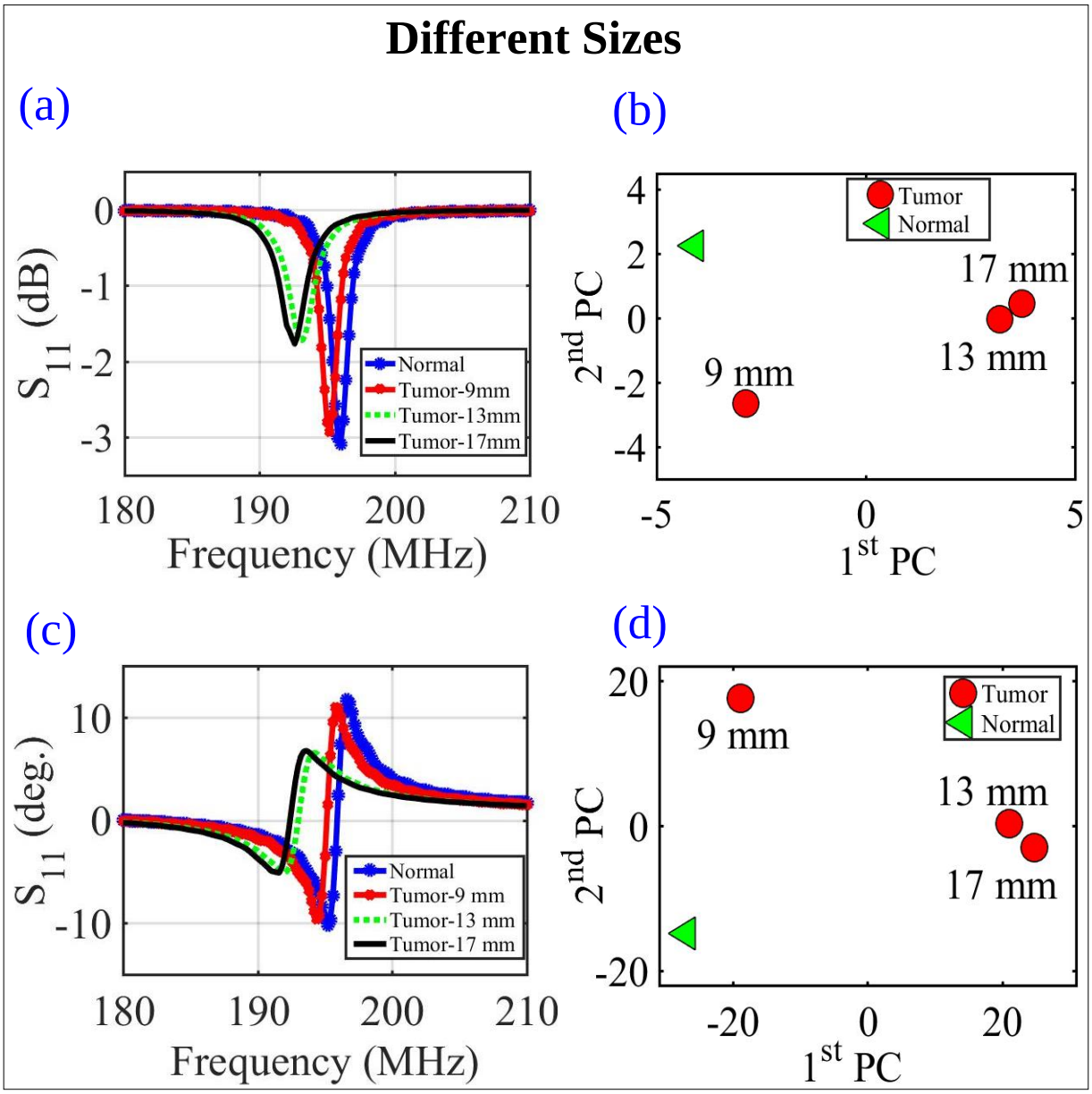


Figure 3.4: The probe response for normal breast tissue and breast tissue with different tumor sizes of 9 mm, 13 mm and 17 mm using the PCA feature extraction method. (a) the magnitude of $S_{11}$, b) the magnitude of $S_{11}$ using PCA, c)the phase of $S_{11}$ and d) the phase of $S_{11}$ using PCA.


Figure 3.5: Experiment setup: (a) The ultra-narrow band probe with chicken breast. (b) The ultra-narrow band probe with two slice of meat.

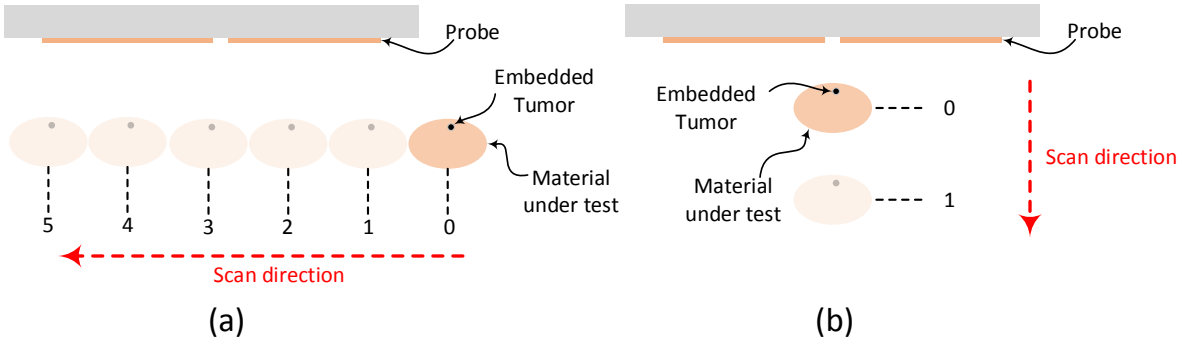


Figure 3.6: A schematic showing the experimental procedures. (a) Horizontal scan. (b) Vertical scan.

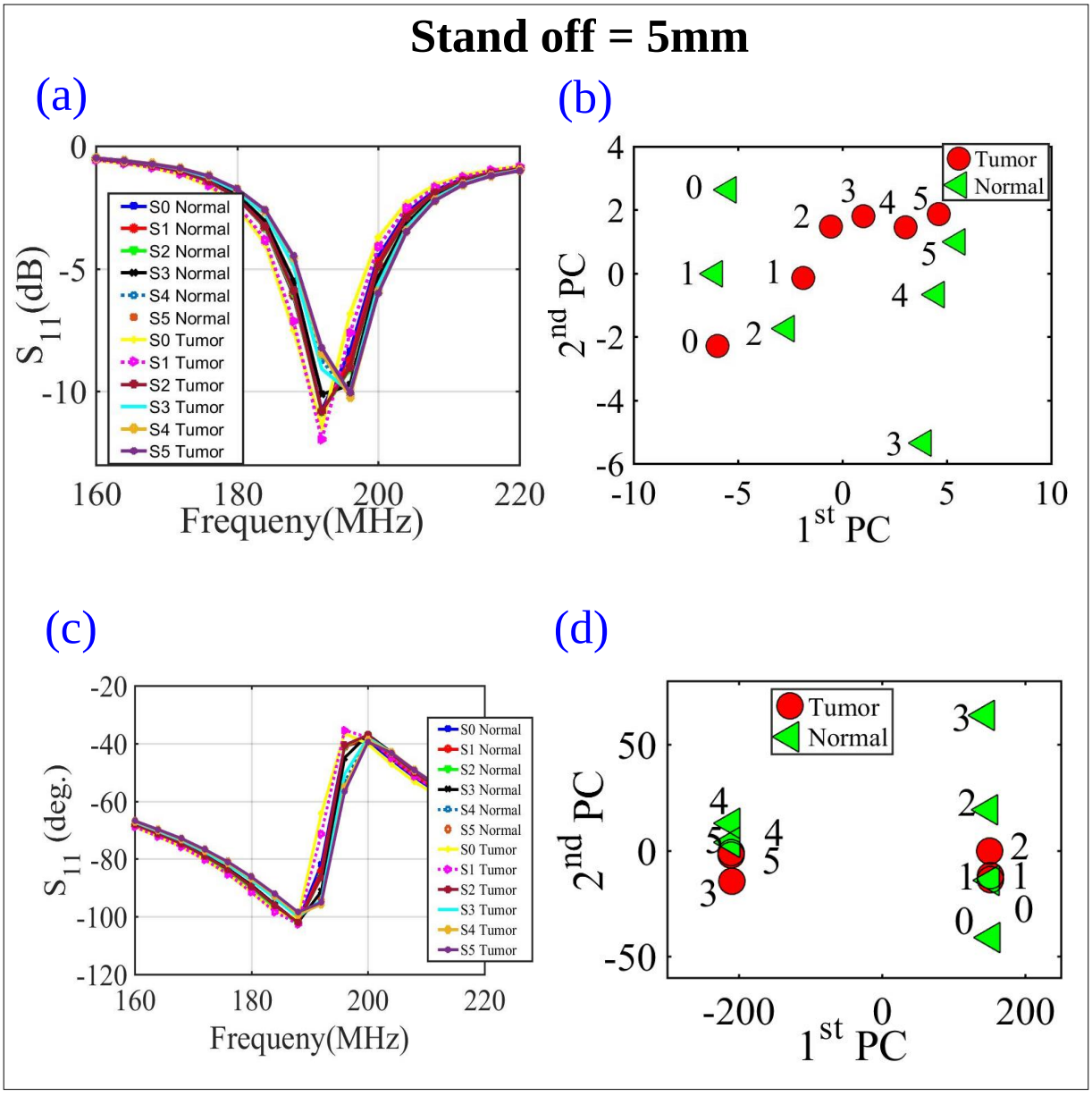


Figure 3.7: Experiment results of a chicken breast with an without an embedded metallic sphere of size 9 mm for all the horizontal scans (showing in Fig. 3.6(a)) and a stand-off distance of 5 mm (showing in Fig. 3.6(b)). The response of the probe was extracted and analyzed for (a) the magnitude of $S_{11}$, (b) the magnitude of $S_{11}$ using PCA, (c) the phase of $S_{11}$ and (d) the phase of $S_{11}$ using PCA.

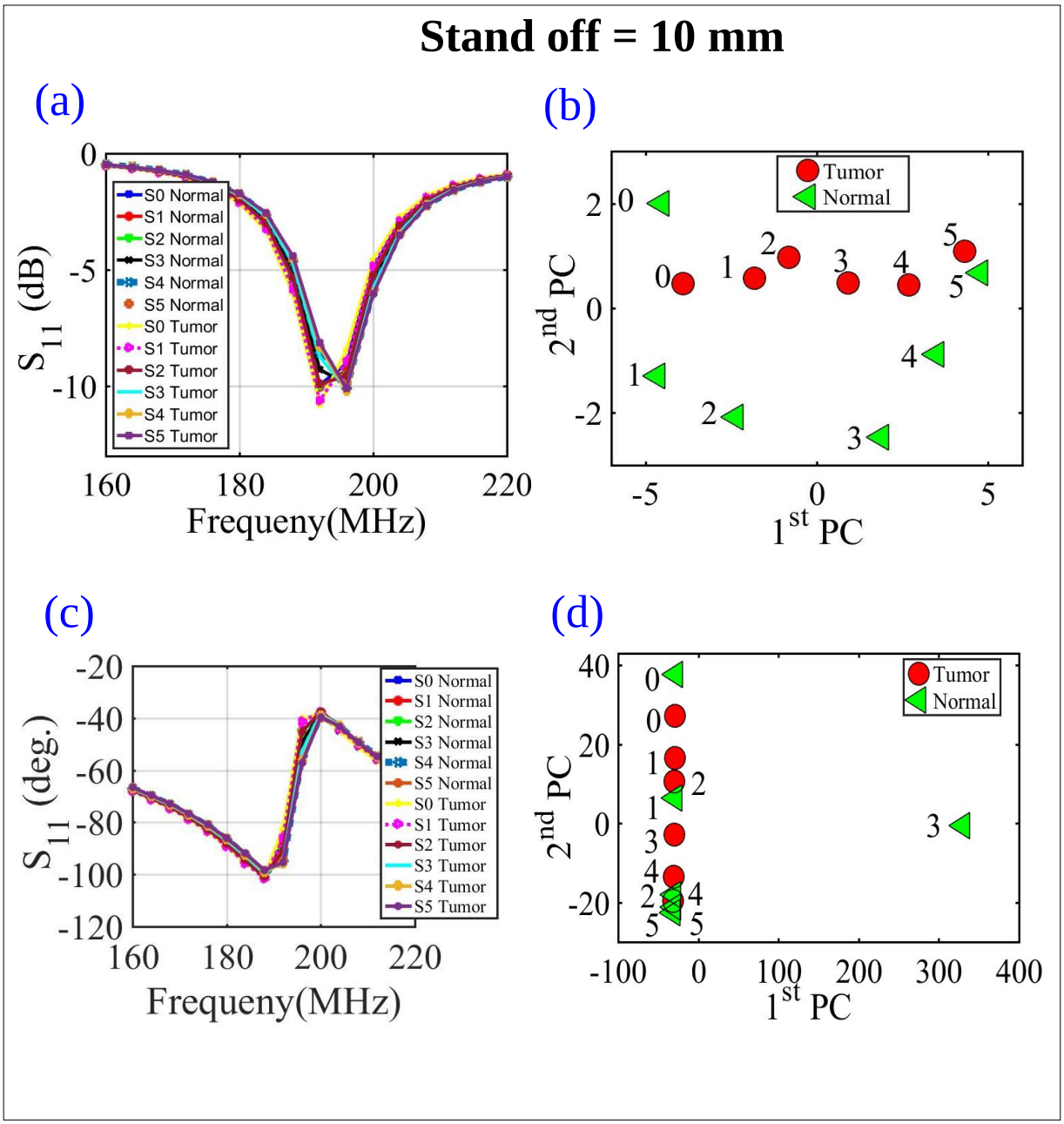


Figure 3.8: Experiment results of a chicken breast with an without an embedded metallic sphere of size 9 mm for all the horizontal scans (showing in Fig. 3.6(a)) and a stand-off distance of 10 mm (showing in Fig. 3.6(b)). The response of the probe was extracted and analyzed for (a) the magnitude of $S_{11}$, (b) the magnitude of $S_{11}$ using PCA, (c) the phase of $S_{11}$ and (d) the phase of $S_{11}$ using PCA.

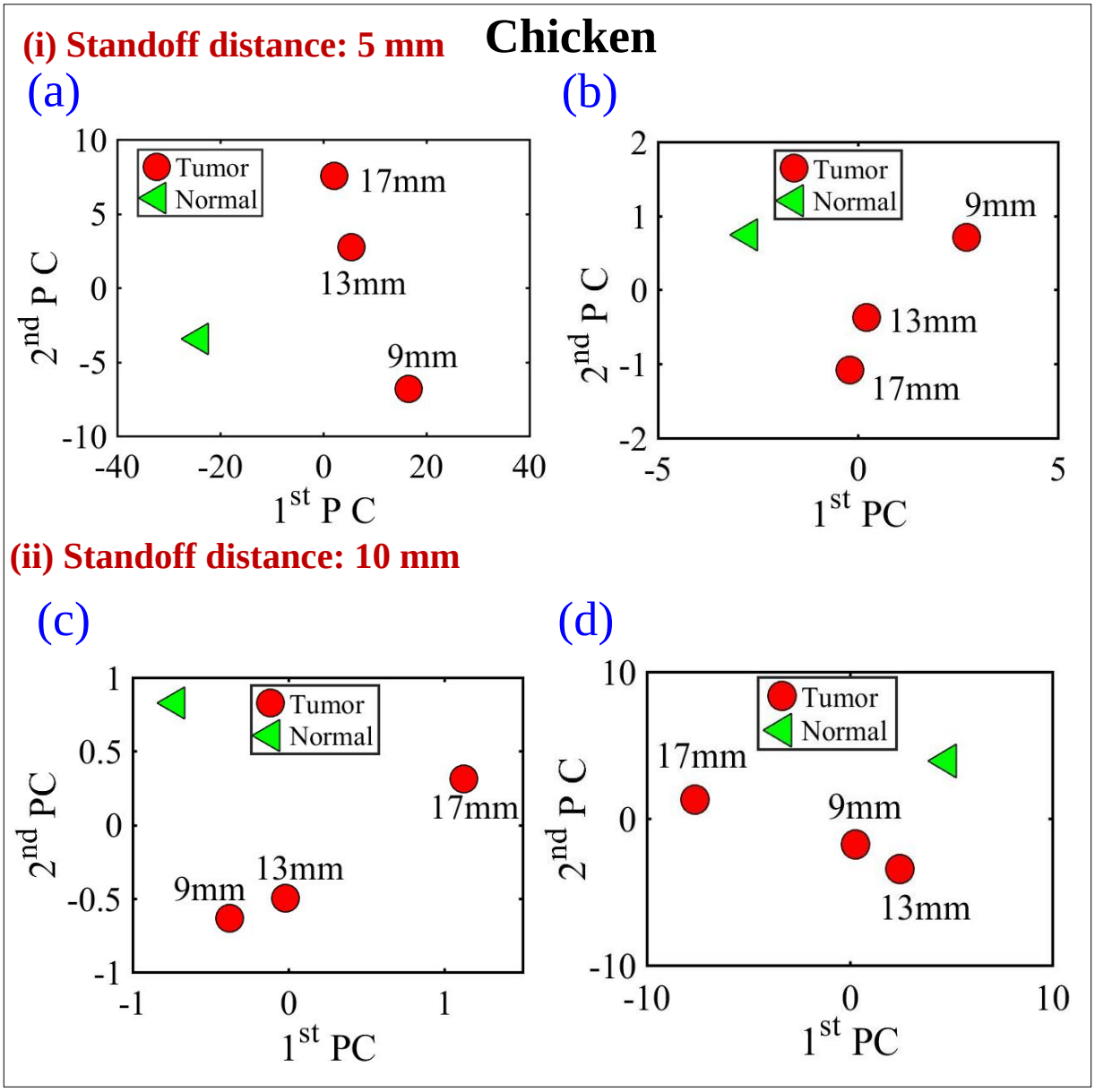


Figure 3.9: Experiment results of using three different sizes of metallic spheres of size 9 mm, 13 mm and 17 mm embedded in a the chicken breast using PCA with a stand-off distance of 5 mm for (a) magnitude of $S_{11}$ and (b) the phase of $S_{11}$ and stand-off distance of 10 mm for the (c) magnitude of $S_{11}$ and (d) the phase of $S_{11}$ using PCA.

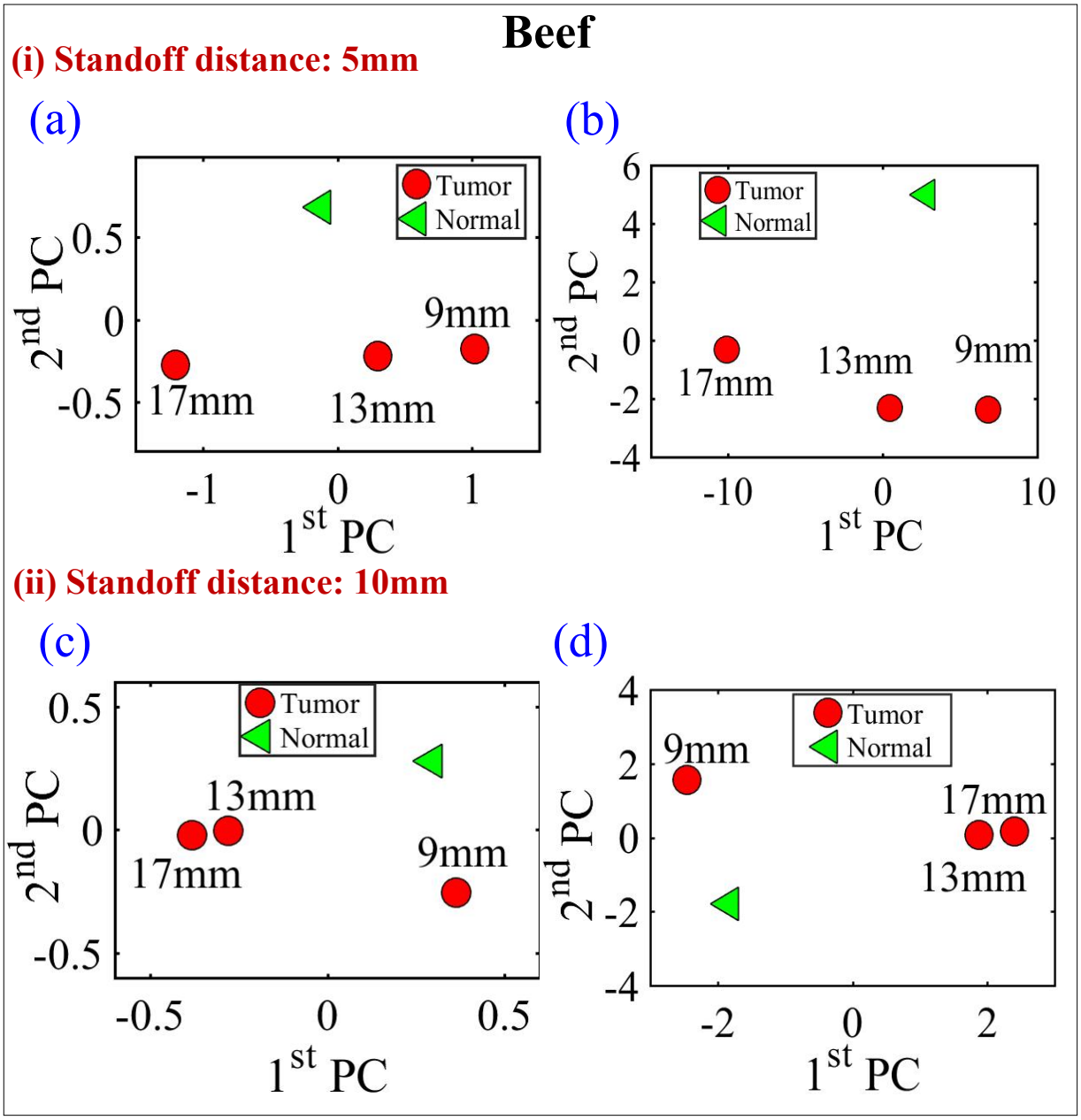


Figure 3.10: Experiment results of using three different sizes of metallic spheres of size 9 mm, 13 mm and 17 mm embedded in a ***slice of beef*** using PCA analyses with vertical distances of 5 mm (for the a)magnitude of $S_{11}$ and b)phase of $S_{11}$ and a vertical distance of 10 mm (for the c)magnitude of $S_{11}$ and d)phase of $S_{11}$).

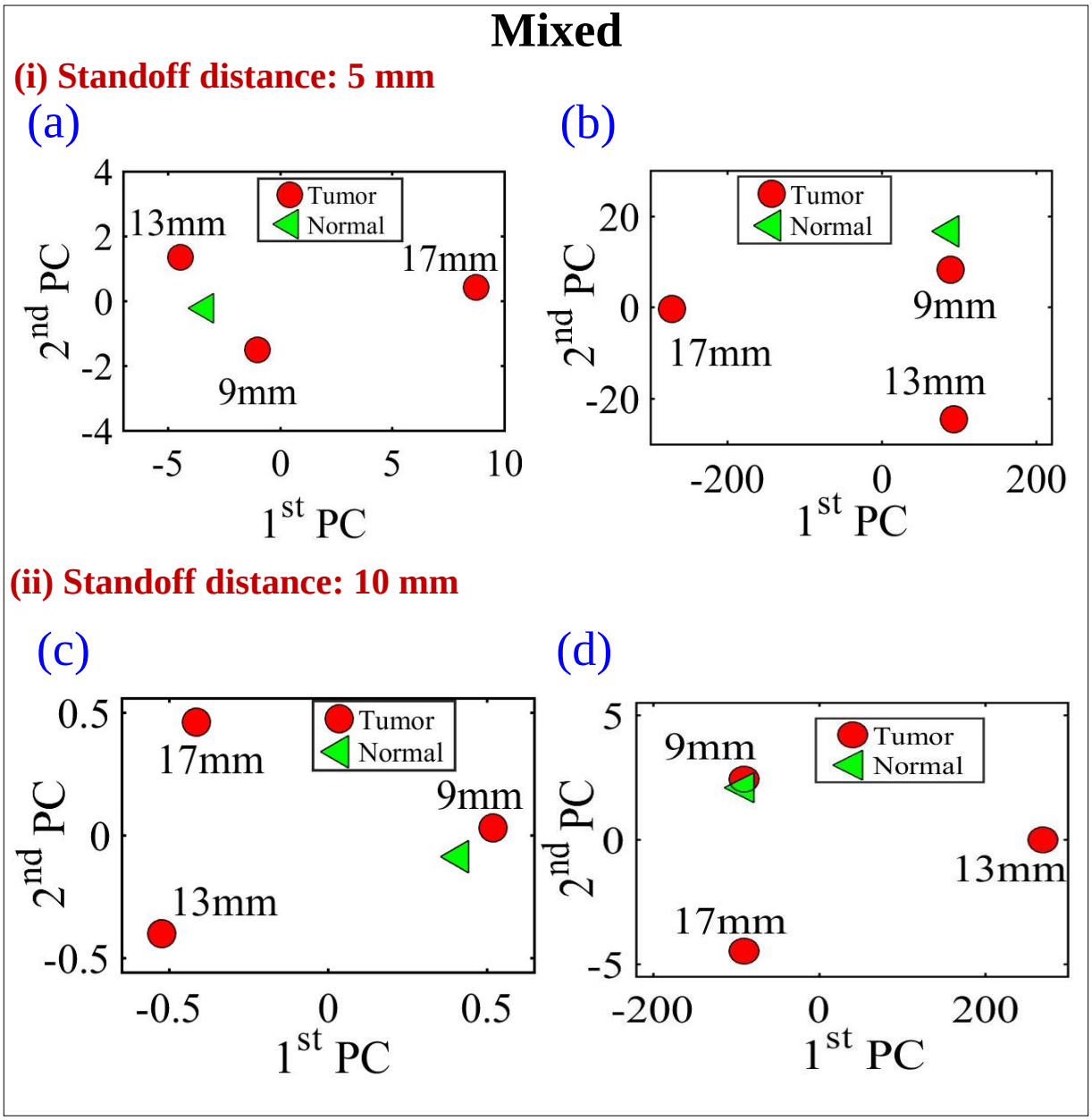


Figure 3.11: Experiment results of using three different sizes of metallic spheres of size 9 mm, 13 mm and 17 mm embedded in a ***mixture of a slice of beef and chicken breast*** using PCA analyses with vertical distances of 5 mm (for the a)magnitude of $S_{11}$ and b)phase of $S_{11}$ and a vertical distance of 10 mm (for the c)magnitude of $S_{11}$ and d)phase of $S_{11}$).

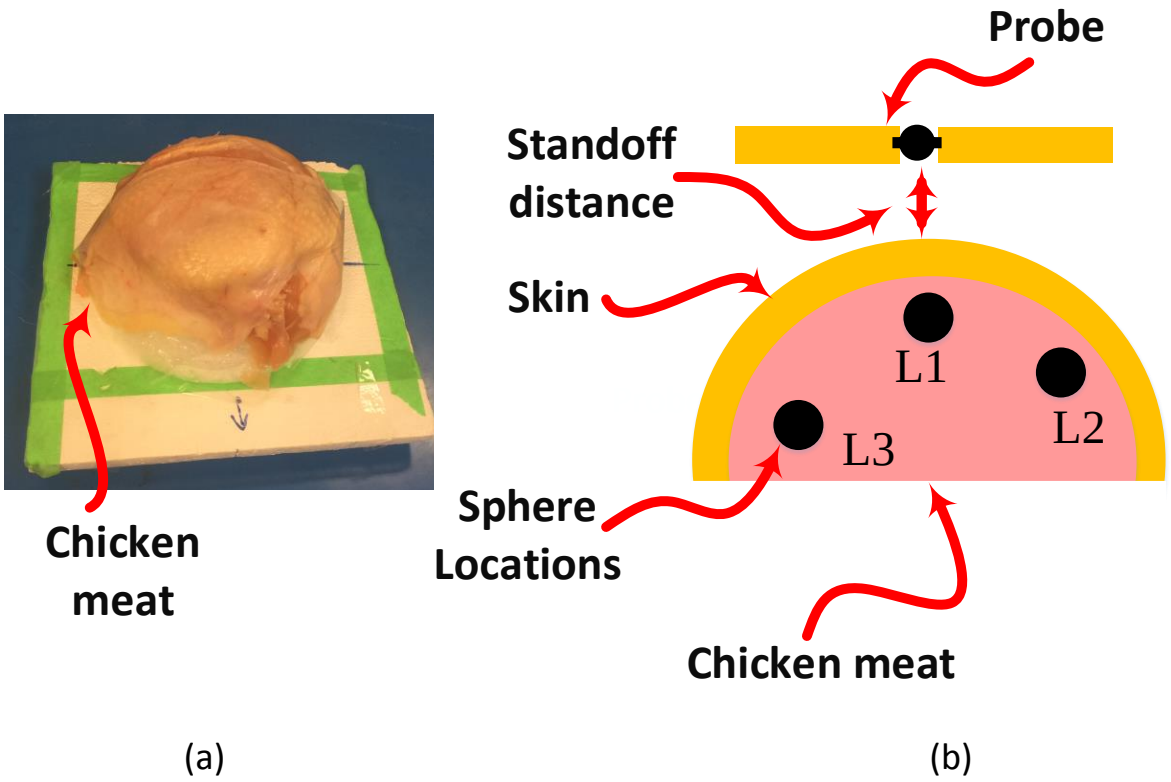


Figure 3.12: Experiment setup: (a) The chicken meat placed on hemispherical shape Styrofoam. (b) A schematic showing the inserted 9 mm sphere at three different location inside the chicken meat.

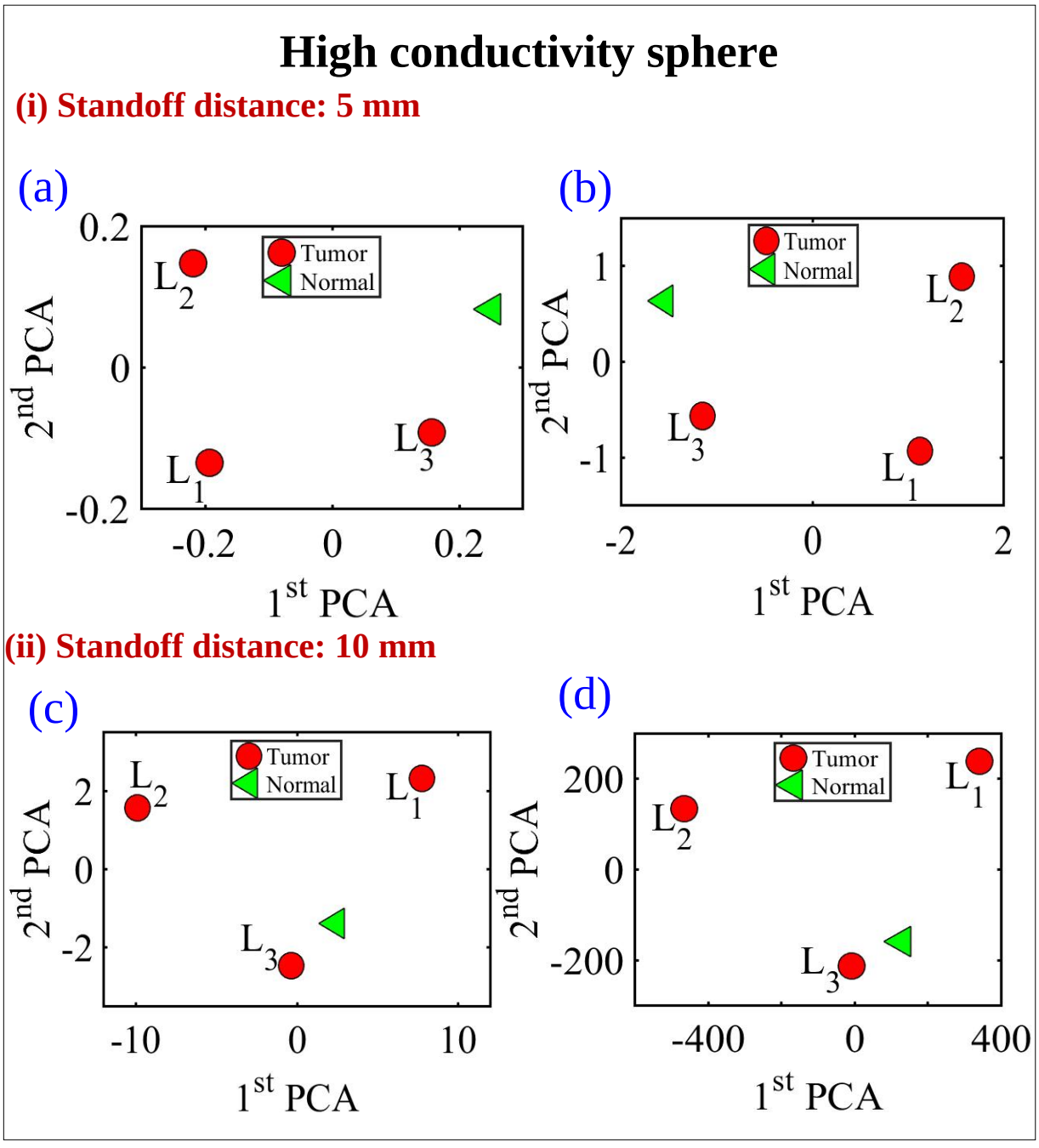


Figure 3.13: Experiment results of using a 9 mm metallic sphere embedded in a ***hemi-sphere chicken meat*** at three different locations using PCA analyses. a) magnitude of $S_{11}$ and b) phase of $S_{11}$ at distance off 5 mm respectively. c) magnitude of $S_{11}$ and d) phase of $S_{11}$ at distance off 10 mm respectively.

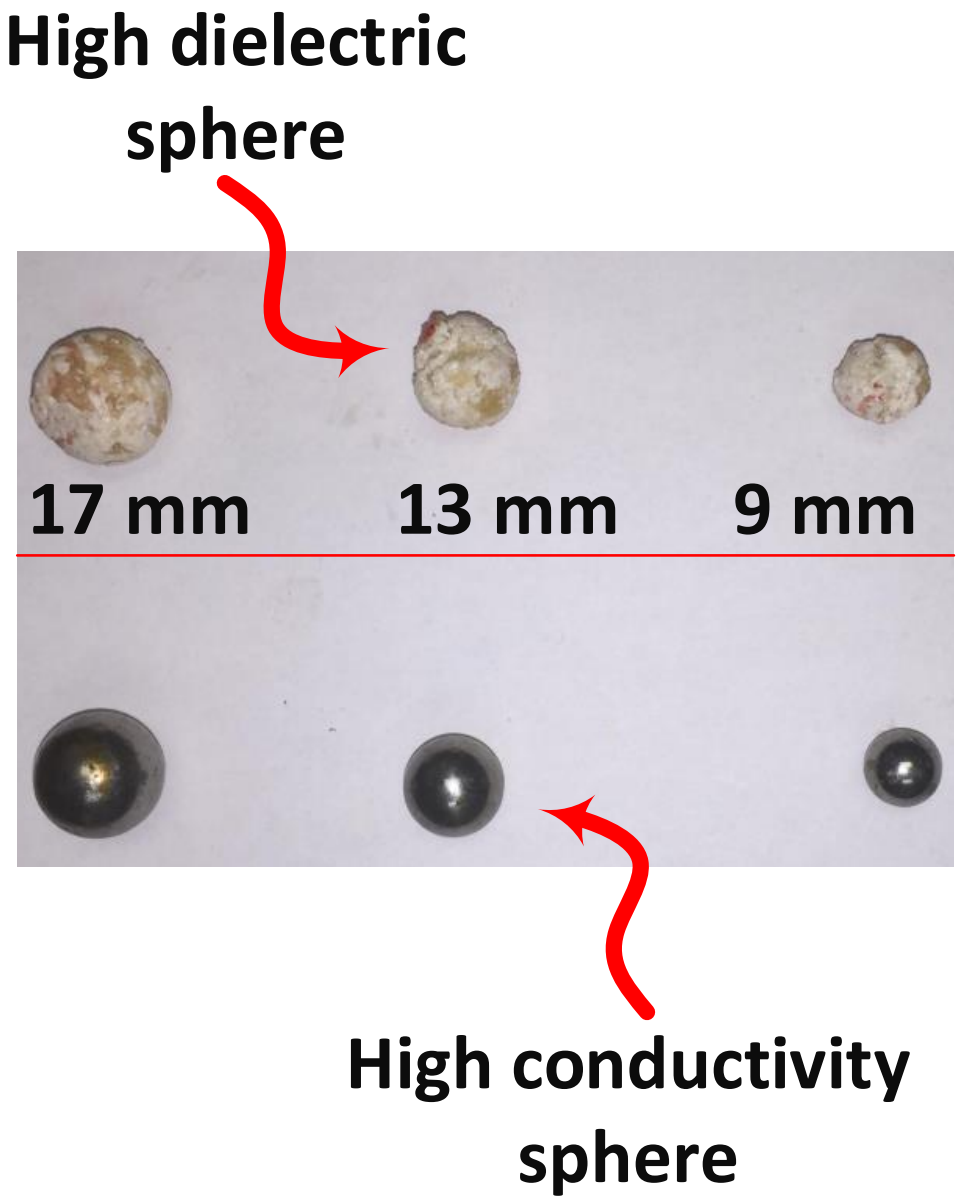


Figure 3.14: View of three different sizes of high conductive (metallic spheres) and high dielectric spheres (oil gelatine mixture spheres).

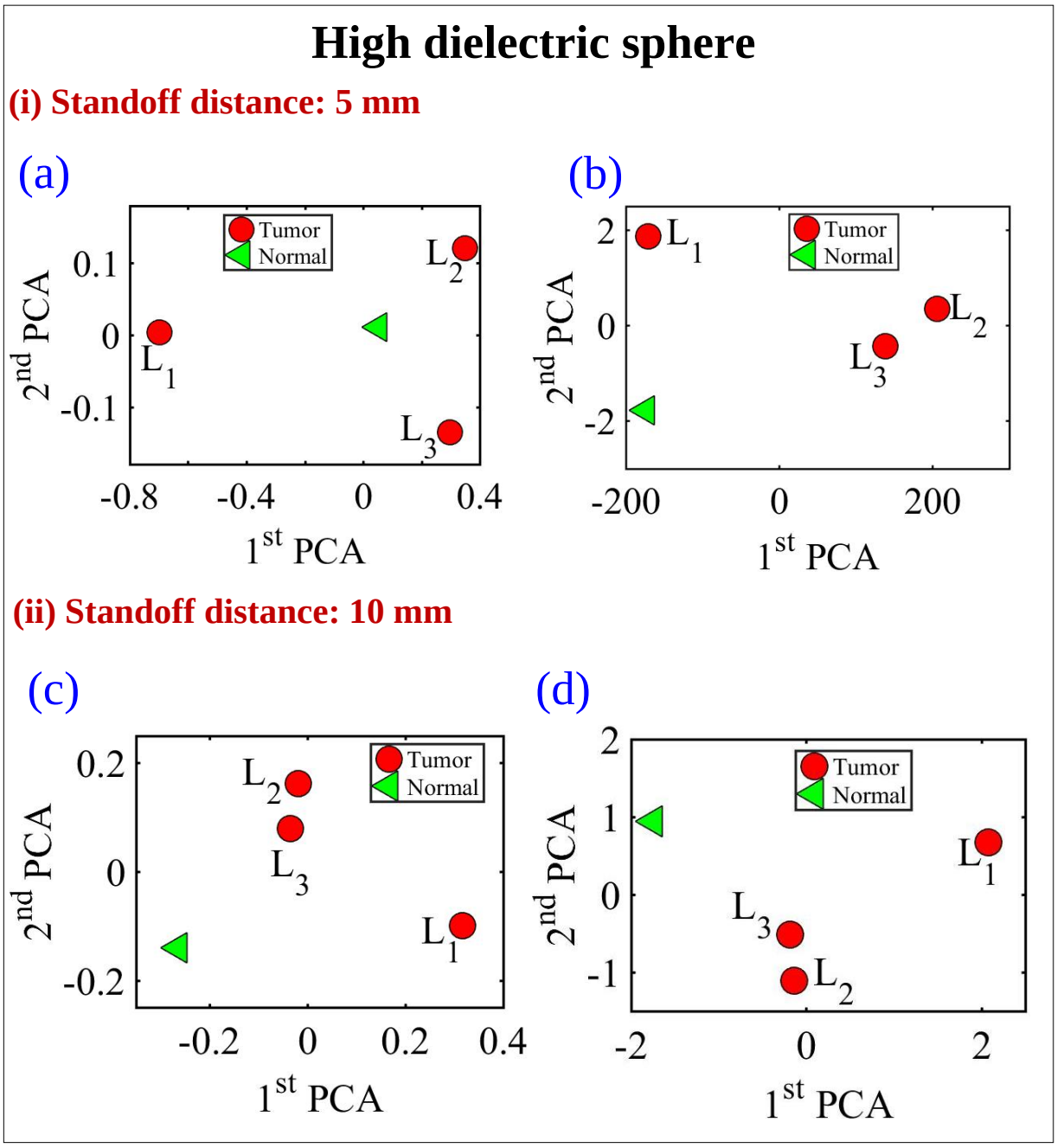


Figure 3.15: Experiment results of using a 9 mm high dielectric sphere embedded in a ***hemisphere chicken meat*** at three different locations using PCA analyses. a) magnitude of $S_{11}$ and b) phase of $S_{11}$ at distance off 5 mm respectively. c) magnitude of $S_{11}$ and d) phase of $S_{11}$ at distance off 10 mm respectively.

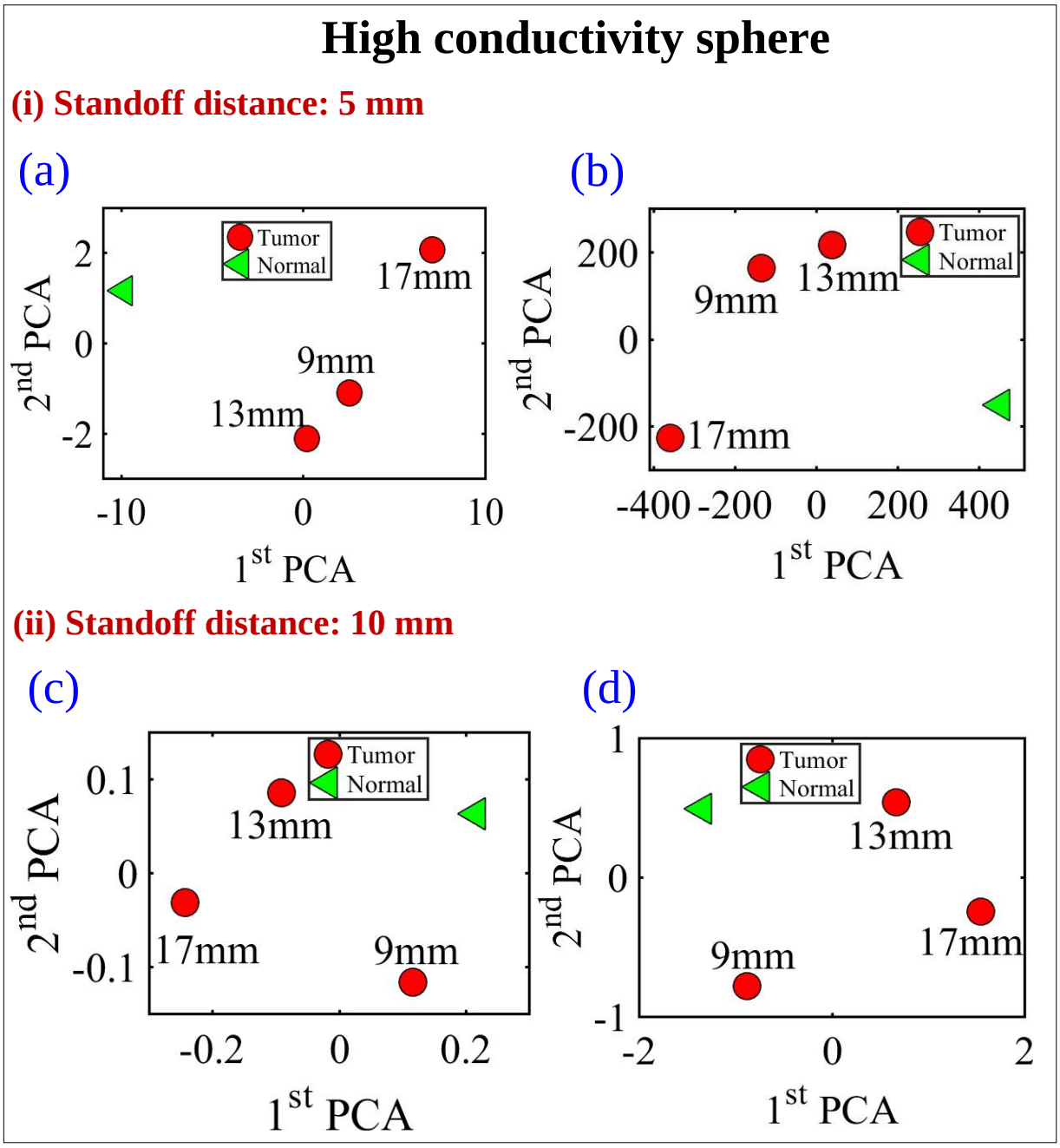


Figure 3.16: Experiment results of using three different sizes of high conductive spheres of size 9 mm, 13 mm and 17 mm embedded in a ***hemisphere chicken breast*** using PCA analyses. a) magnitude of $S_{11}$ and b) phase of $S_{11}$ at distance off 5 mm respectively. c) magnitude of $S_{11}$ and d) phase of $S_{11}$ at distance off 10 mm respectively.

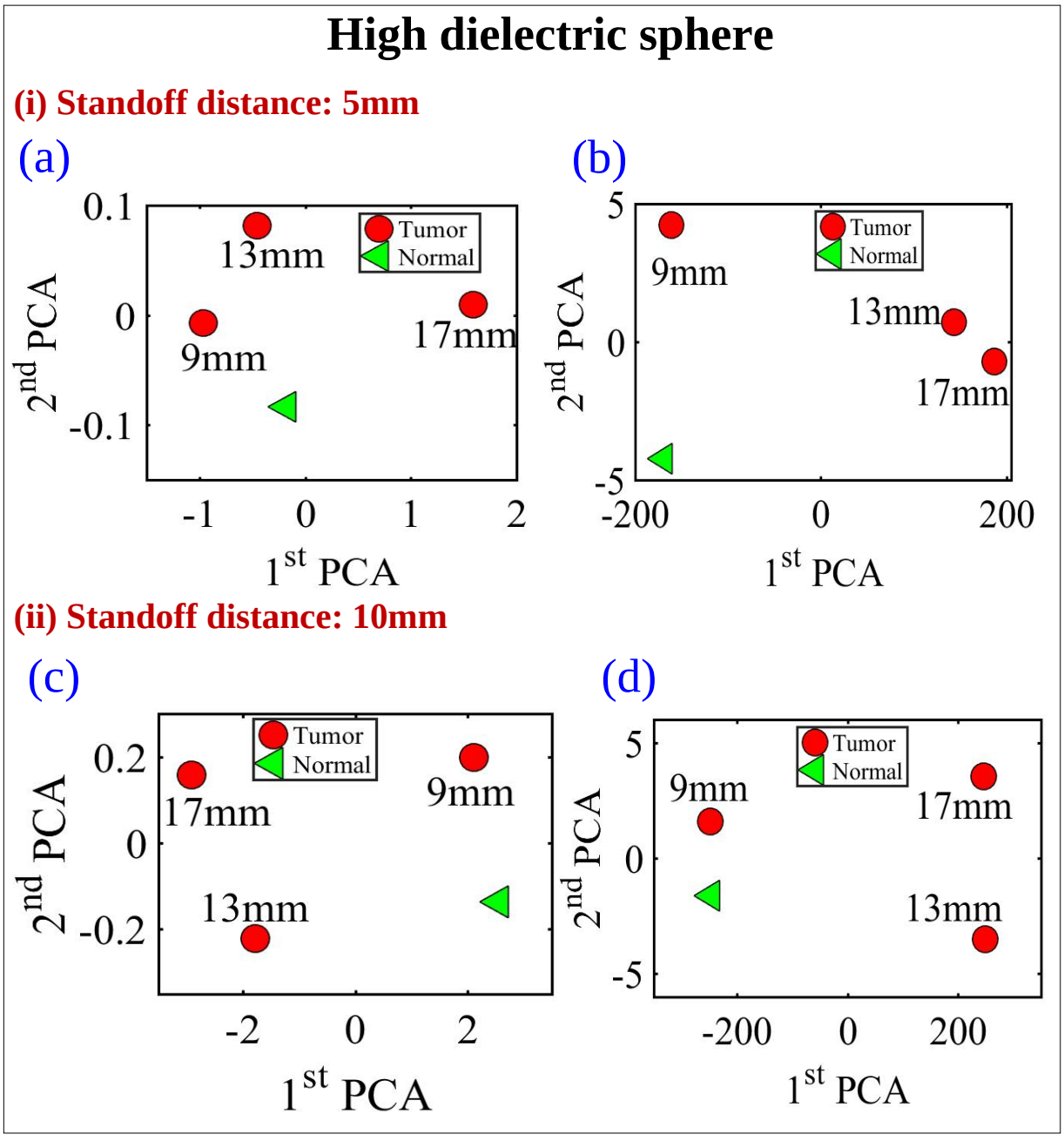


Figure 3.17: Experiment results of using three different sizes of high dielectric spheres (oil gelatine mixture spheres) of size 9 mm, 13 mm and 17 mm embedded in a ***hemisphere chicken breast*** using PCA analyses. a) magnitude of $S_{11}$ and b) phase of $S_{11}$ at distance off 5 mm respectively. c) magnitude of $S_{11}$ and d) phase of $S_{11}$ at distance off 10 mm respectively.

# Chapter 4

# Electrically Small Magnetic Probe with PCA for Near-Field Microwave Breast Tumors Detection

## 4.1 Introduction

In this chapter, an electrically small magnetic probe combined with principal components analysis (PCA) technique for microwave breast cancer detection is presented. The proposed magnetic probe is designed as an electrically small square loop antenna integrated with a matching network operating at 528 MHz. The concept of the proposed microwave detection is based on the shift in the resonance frequency of the near-field magnetic probe due to the presence of a tumor. The proposed magnetic probe is highly sensitive in detecting any changes or abnormality in the dielectric properties of the female breast tissues. Detecting the existence of the breast tumors are expected by estimating the variations in the scattering parameters of the probe's response. The PCA is a feature extraction technique applied to accentuate the variance in the sensor responses for both healthy and tumorous cases. It is shown that when a numerical realistic breast phantom with and without tumor cells is placed close to the magnetic probe in the

near-field region, the probe is capable of distinguishing between healthy and tumorous tissues. In addition, the probe can identify tumors with various sizes placed in a specific location within the breast. As a proof of concept, the magnetic probe was fabricated and used to detect a 9 mm metallic sphere buried at three different locations inside a lump of chicken meat, mimicking both normal and tumorous breast tissues, respectively. The CST numerical simulations and experimental results demonstrate that the presented technique is an emerging modality for detecting breast tumors through an inexpensive and portable way.

In the previous chapter, an electric dipole was employed as a probe to collect the electromagnetic signature with and without a tumor. Since malignant tumors possess a frequency-dependent conductivity that is higher than the surrounding tissues, in this work we propose a *magnetic* probe so that the electromagnetic response is accentuated as compared to an electric dipole. This is attributed to the fact that the magnetic field produced by the magnetic dipole is affected when placed in close proximity to a conductive material. Such effect is translated as a shift in the scattering parameter of the magnetic probe as will be shown in the results section.

## 4.2 Probe design

The magnetic probe employed in this work consists of a square loop with lumped capacitors placed at the middle of each arm as depicted in Fig. 4.1. The main reason for loading the loop with the capacitors is to miniaturize the loop such that it would resonate at lower frequencies. Such a row operating frequency is required to ensure a reasonable penetration level into the breast tissues. The loop was hosted on top of a RO4003C Rogers material with a dielectric constant of $\epsilon_r = 3.38$ and a thickness of 1.54 mm. Each arm of the loop has a length of $L = 30$ mm and width of $w = 30$

mm. The values of the lumped capacitors are $C_1 = C_2 = 8.2$ pF, $C_3 = 5.7$ pF, $C_4 = 2$ pF, and $C_5 = 160$ nF. The capacitors $C_4$ and $C_5$ play a major role in matching the loop with a 50 Ω feeding line at the desired resonance frequency of 528 MHz which lies within the medical band. The loop is then simulated using CST Microwave Studio [60]. The probe simulation response was obtained as shown in Fig. 4.2(a).

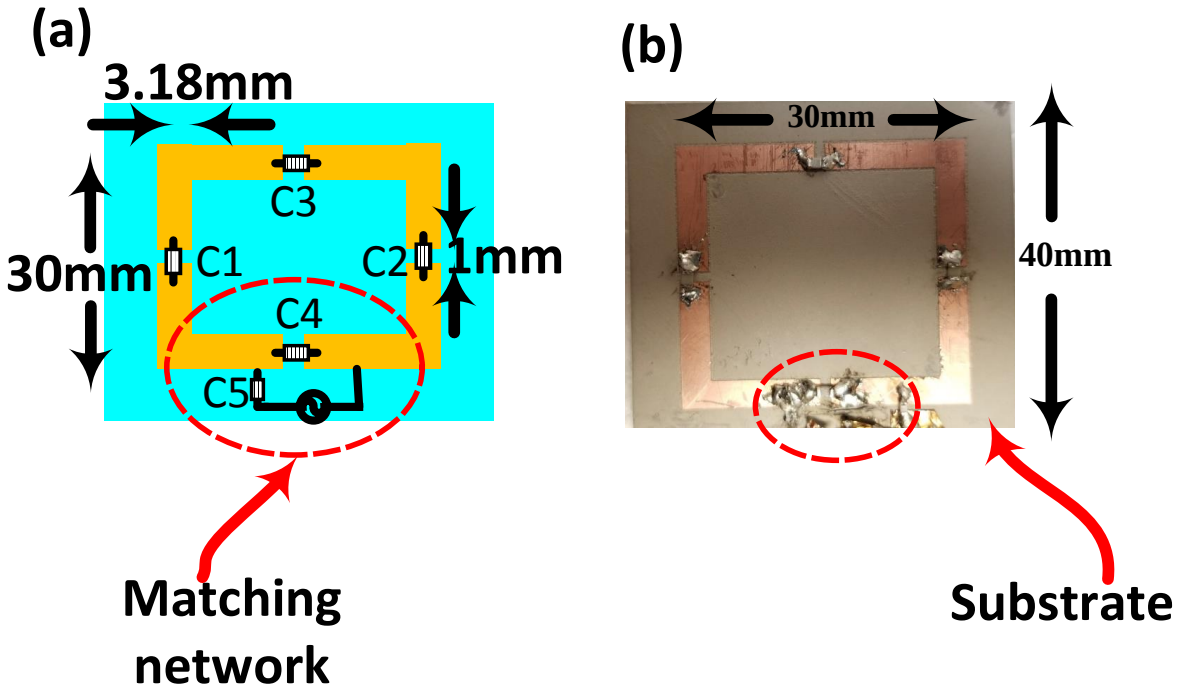


Figure 4.1: The proposed electrically small probe showing in (a) schematics and (b) fabricated. In both sub-figures, the probe consists of a loop antenna with five capacitors used as matching network.

The fabricated prototype of the proposed probe is shown in Fig. 4.1(b). The five capacitors were soldered accordingly, and a coaxial cable was placed across the feed of the loop probe. The simulated and measured reflection coefficients of the probe are depicted in Fig. 4.2(b). It is obvious from the

obtained results that the resonance frequency of both the simulated and measured responses is 528 MHz. However, the measured $S_{11}$ bandwidth is much wider than the simulated one due to the losses of the lumped elements which were not accounted for in the simulation.

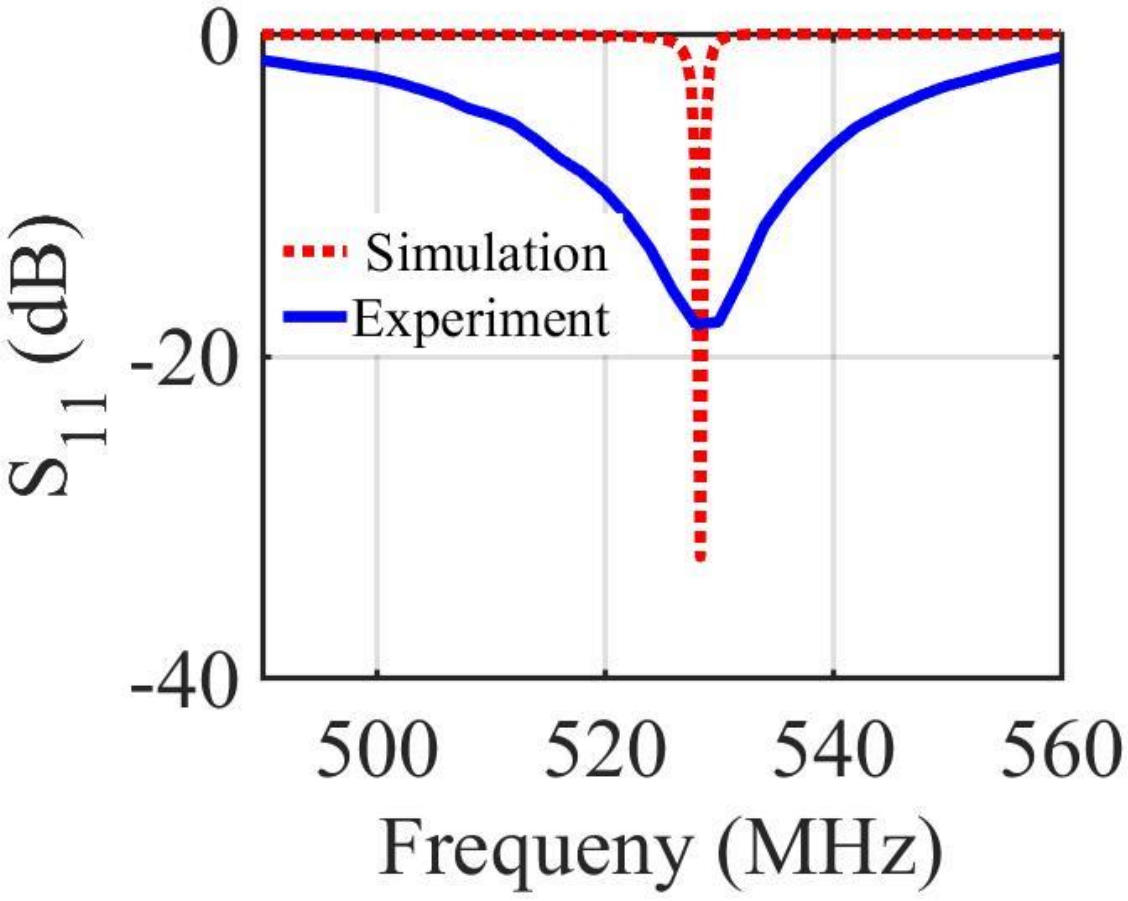


Figure 4.2: The simulated and measured reflection coefficients of the probe.

To investigate the capabilities of the proposed magnetic probe for detecting breast tumor cells, the proposed probe was tested with a realistic female breast through numerical simulations. In this chapter, the heterogeneously

dense breast phantom model of the ID: 062204 ACR classification: Class No. 3 is used.

First, the developed probe is placed at a stand-off distance of 5 mm from the healthy breast phantom as shown in Fig. 4.3(a). The probe's response was then recorded. Next, a 9 mm tumor was placed at three different locations inside the healthy breast as shown in Fig. 4.3(b). The dielectric properties of inserted tumor were obtained from tumor surgery as presented in [70]. The three locations namely L1, L2 and L3 are labeled according to the distance between the tumor and the probe where L1 is the closest from the probe, L2 deeper than the first location L1 and L3 is the farthest to the probe. The probe response was then recorded for the other breast with the embedded tumor. The probe response data that contain the magnitude and phase are then analyzed with and without the tumor to determine whether or not the breast is infected with a tumor.

Next, PCA as a feature extraction method [96, 97, 100] is employed to emphasize the variation of the probe responses of both normal and tumors cases by extracting important data from the magnitude and phase of the probe's response datasets. These datasets are then represented as orthogonal vectors called principal components [96, 97, 100]. In large datasets, the Principal Component Analysis (PCA) is used to reduce the dimensionality by implementing a vector space transform [97, 100]. The PCA task is to abstract the important information from the data set and to express this information as a set of new- orthogonal variables called principal components [100]. In Mathematical terms, eigen-decomposition of positive semi-definite matrices and the singular value decomposition of rectangular matrices are used for finding the principal components [97]. Thus, via mathematical projection, high dimensional original datasets can be reduced to small number of variables without losing much of the original information to analyze trends, patterns and outliers [100].

In the proposed microwave detection technique, the reflection coefficient

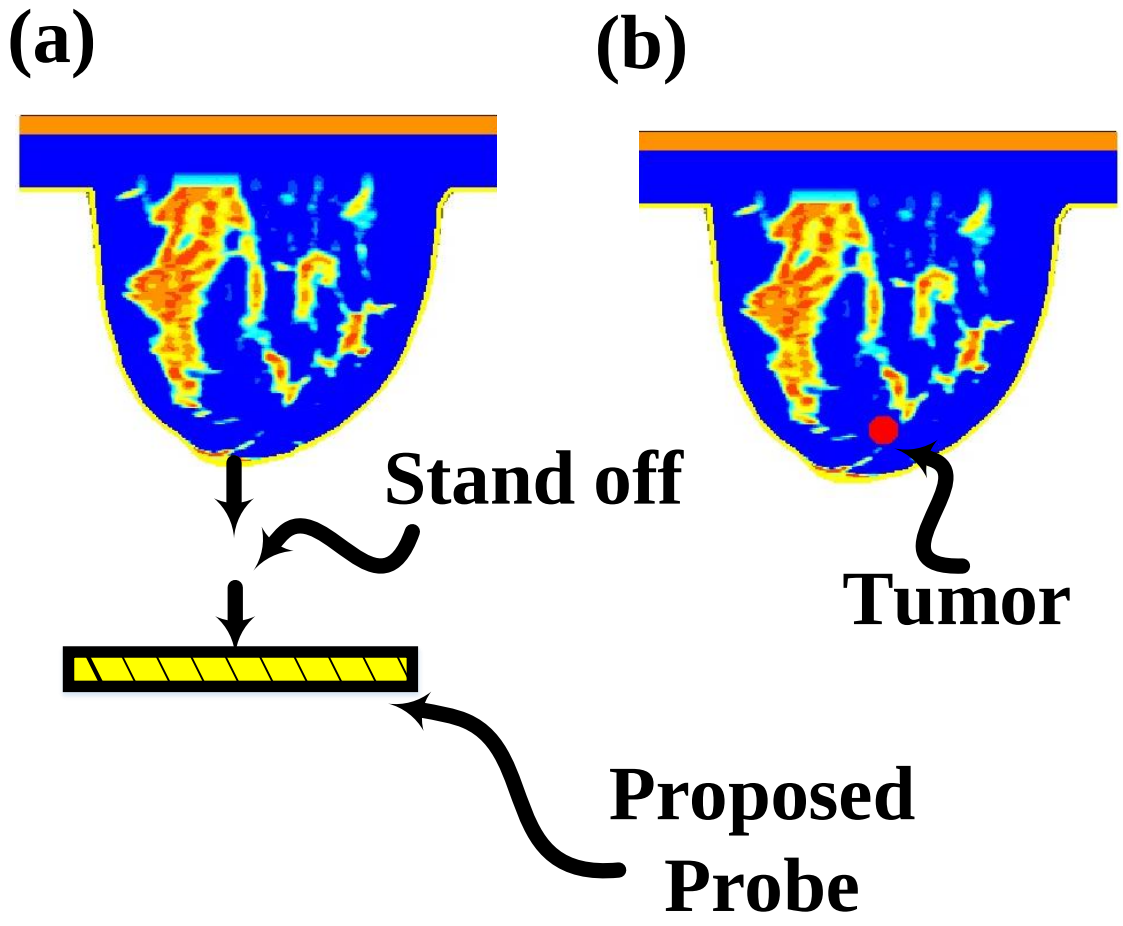


Figure 4.3: Numerical simulation set-up: (a) Magnetic probe at a stand-off distance of 5 mm away from the 3-D normal breast phantom model. (b) The inserted tumor in the breast model.

of the proposed magnetic probe which contains the magnitude and phase features are extracted. Here, the feature vectors prior to applying the PCA analysis method are the magnitude and phase of scattering parameters (S11) of the probe. Each discrete value of the reflection coefficient changes with the frequency response. The magnitude and phase of the scattering param-

eters of the probe were recorded at 201 different frequencies spanning the range 490 to 560 MHz. The first feature datasets, magnitude, is defined by the first and second column which contains the frequency and magnitude points, respectively. The second feature datasets, phase, is defined by the first and third column which includes the frequency and phase points, respectively. The data was then entered into the PCA analysis method code to indicate the existence of a tumor inside a breast phantom. Moreover, PCA is used to emphasize or explore the difference between the measured probe responses datasets of both cases (i.e., with and without tumor). Once the probe scattering parameters of the two examinations of the breast phantom are registered , the probe response was extracted and analyzed with and without PCA as shown in Fig. 4.4. The results of Fig. 4.4(a) show the magnitude of $S_{11}$ and Fig. 4.4(b) show the magnitude of $S_{11}$ using PCA . Fig. 4.4(c) shows the phase of $S_{11}$ and Fig. 4.4(d) shows the phase of $S_{11}$ using PCA. It is evident from the results that the difference in magnitude and phase of the reflection coefficient of the probe between the normal and tumourous case is greater for tumor locations that are closer to the probe.

Then the numerical simulations were extended for detecting three different sizes of tumors placed at a single location. Three different sizes of breast tumors with diameters of 9 mm, 13 mm, and 17 mm are embedded inside the breast phantom to see the capability of the proposed probe for detecting different sizes of the breast tumors as shown in Fig. 4.3(b). The results are shown in Fig. 4.5 for the three different tumor sizes. For all tumor sizes, the probe was capable of detecting the presence of tumor tissues. Obviously from the results, larger tumor sizes are easier to detect, where the shift in the frequency response of both magnitude and phase is noticeable compared with normal case.

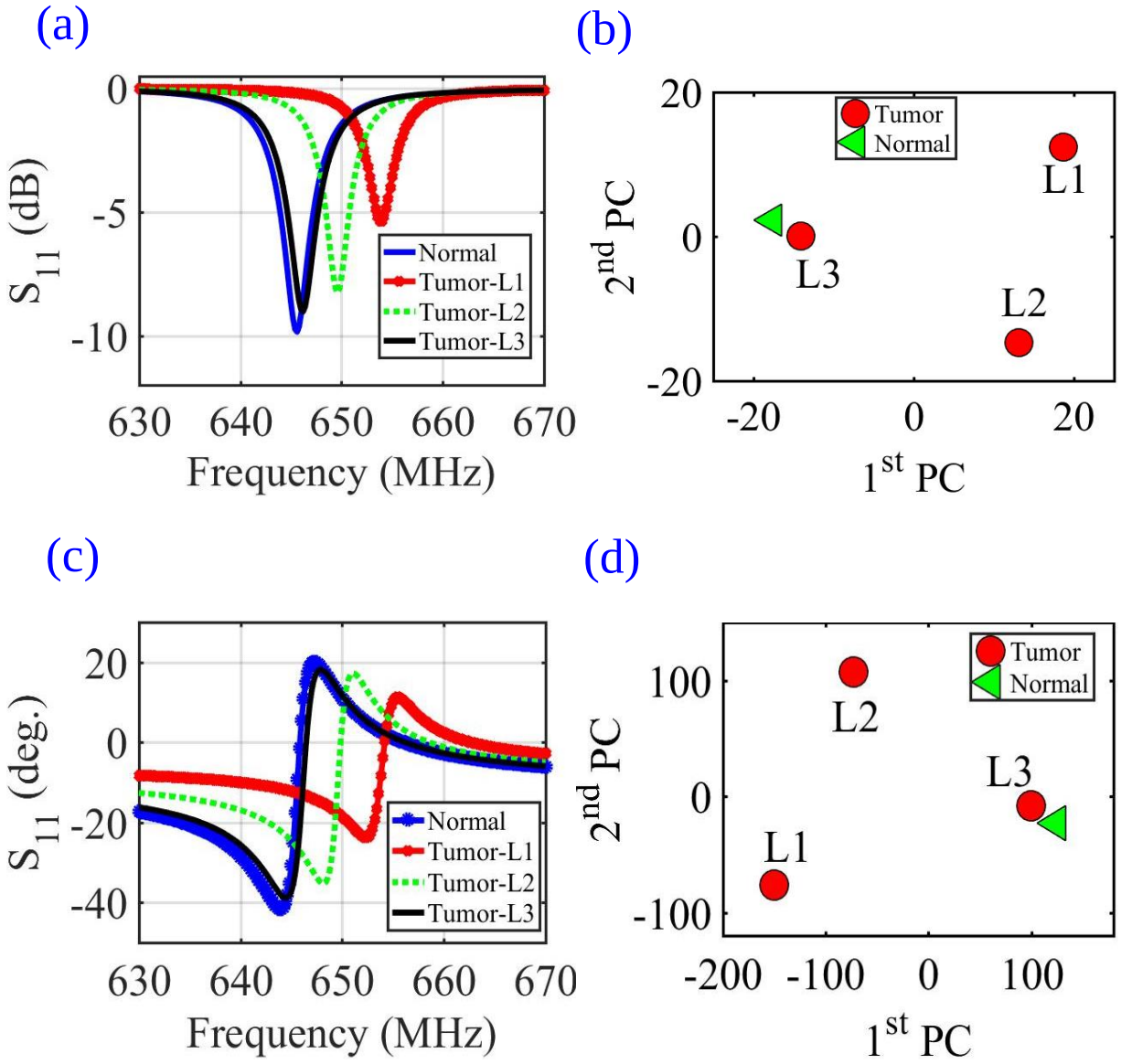


Figure 4.4: Simulation results of the probe magnitude and phase responses for breast phantom model with and without a 9 mm tumor at three different positions. (a) The $S_{11}$ magnitude, (b) the $S_{11}$ magnitude using PCA, (c) the $S_{11}$ phase and (d) the $S_{11}$ phase using PCA.

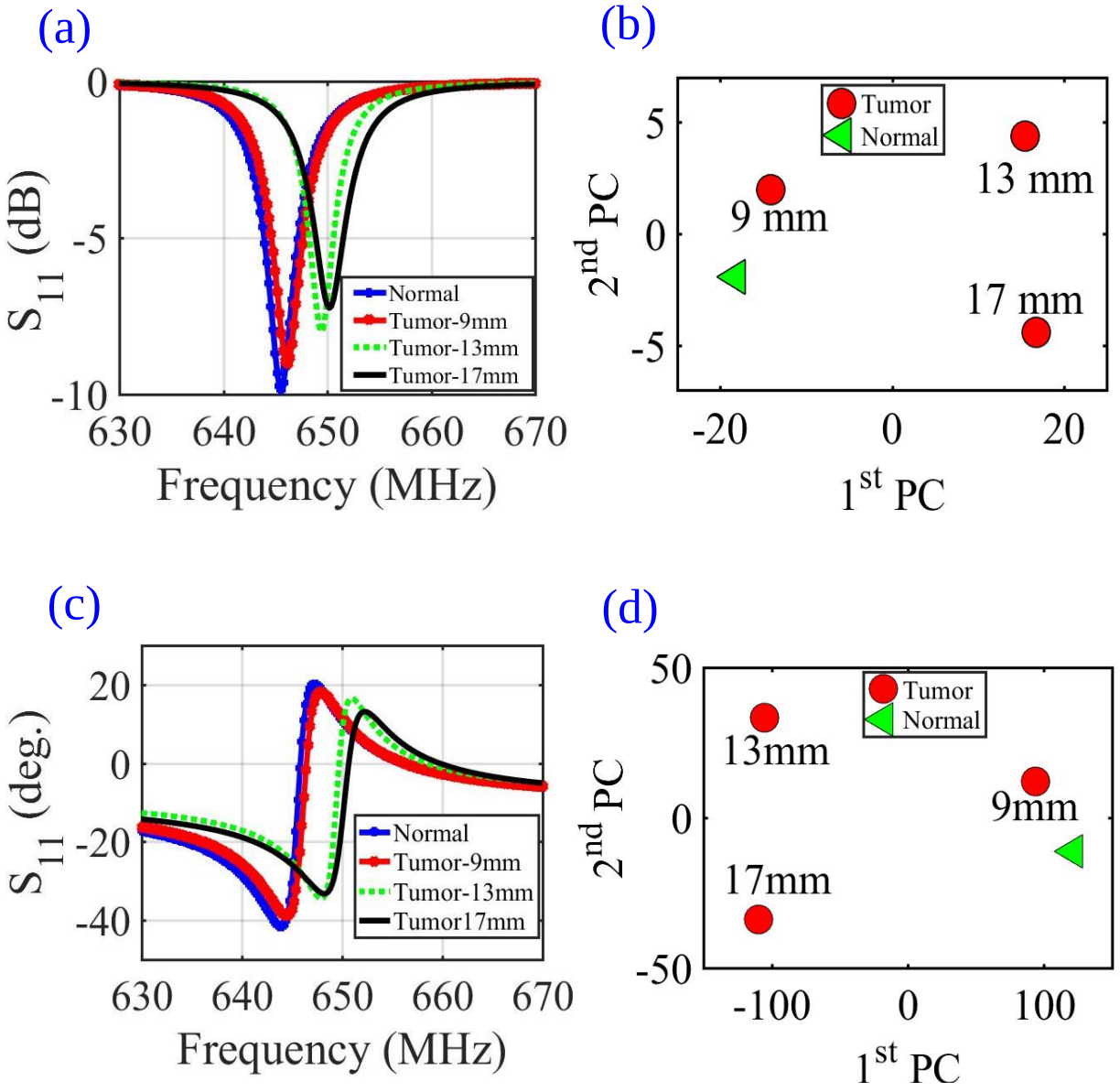


Figure 4.5: Simulation results of the probe response for detecting three different sizes of breast tumors including: 17 mm, 13 mm and 9 mm inserted at the same location inside the healthy breast phantom. (a) $S_{11}$ magnitude, (b) $S_{11}$ magnitude using PCA, (c) $S_{11}$ phase and (d) $S_{11}$ phase using PCA.

## 4.3 Experimental Validation

Several experiments were conducted to validated the obtained simulated results. In the experiments, a lump of chicken meat and metallic spheres were used to mimic a breast phantom and a breast tumor respectively. The chicken meat was placed at a stand-off distance of 5 mm from the fabricated magnetic probe. All the measurement setup was enclosed in a styrofoam as shown in Fig. 4.6.

In the experiment, the same test procedure that was done in the simulation for various tumor locations and sizes is repeated. The obtained results are summarized in Fig. 4.7 and Fig. 4.8. Consistent conclusions were obtained from the experiments as compared to the simulations in terms of the sensitivity of the probe to different tumor locations and sizes.

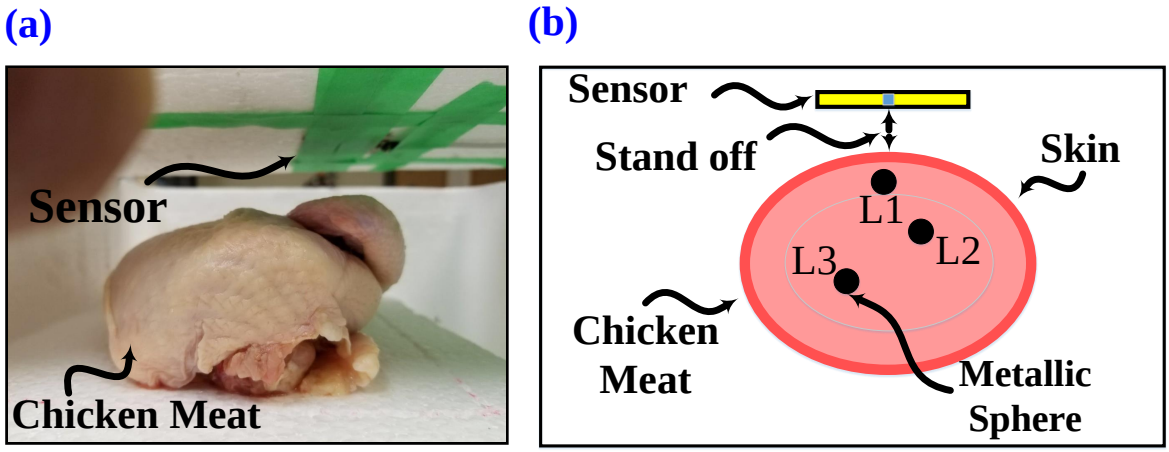


Figure 4.6: Experiment Procedures: (a) The proposed magnetic probe at a stand-off distance of 5 mm from the chicken meat. (b) A schematic illustrating the experimental setup when inserting a 9 mm metallic sphere at three different positions inside the chicken meat.

For all sizes of the tumor, the probe was capable of detecting the presence of tumor tissues as depicted in Fig. 4.8 . Obviously, and from the experimental results, larger tumor sizes are easier to detect. It is evidenced

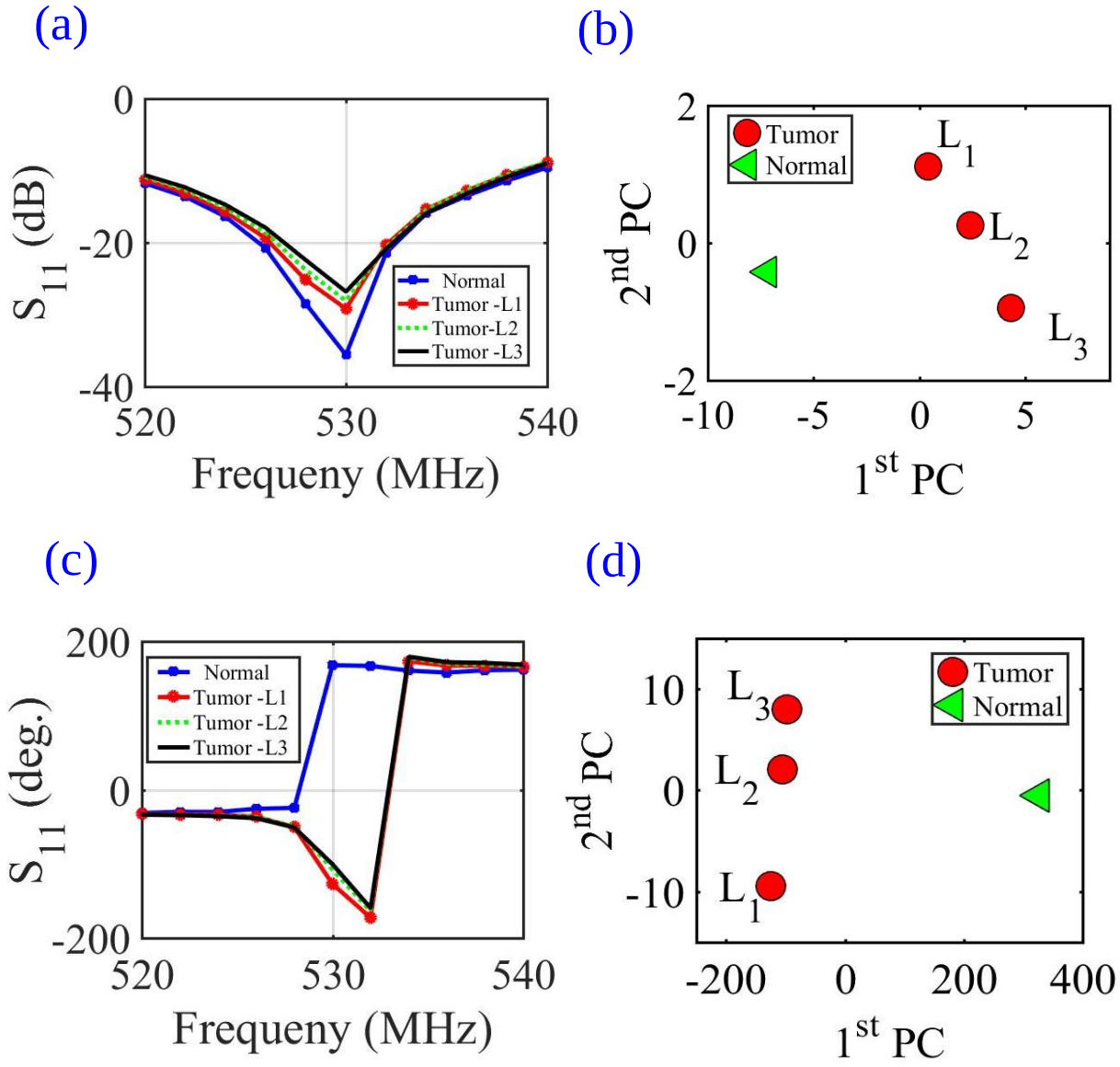


Figure 4.7: Experiment results showing the probe responses for detecting a 9 mm metallic sphere inserted at three different locations inside the chicken meat. (a) The magnitude of $S_{11}$, (b) the magnitude of $S_{11}$ using PCA, (c) the phase of $S_{11}$ and (d) the phase of $S_{11}$ using PCA.

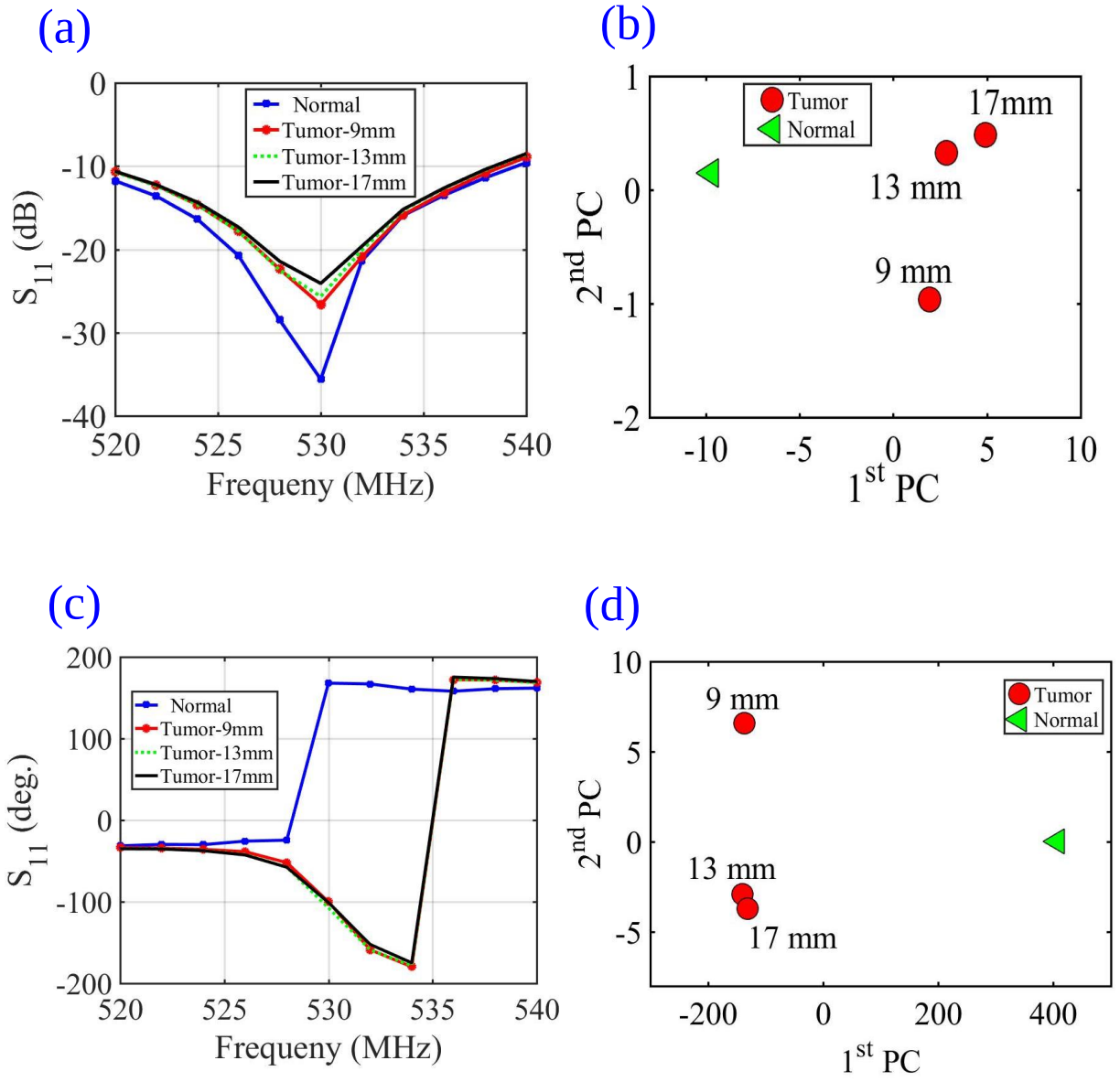


Figure 4.8: Experimental results showing the probe response for detecting three different sizes of metallic spheres of size 9 mm, 13 mm and 17 mm inserted at the same location inside the chicken meat. (a) $S_{11}$ magnitude, (b) $S_{11}$ magnitude using PCA, (c) $S_{11}$ phase and (d) $S_{11}$ phase using PCA.

that as the tumor size increases, the classification using the PCA between the healthy and infected (with different tumor sizes) chicken meat is distinguishable.

## 4.4 Conclusion

In this chapter, a new microwave detection technique for human female breast tumor using an electrically small single loop magnetic probe is introduced. The sensing scheme has the advantages of providing non-ionizing, inexpensive and easy to use method of detection. The detection modality introduced here is used to classify between the healthy and tumorous breast based on the interaction between the microwave signal of a magnetic-small loop probe and the dielectric properties of the breast tissues of the human female breast. The sensing concept was validated through numerical and experimental tests by detecting tumors placed at different locations and various sizes. The simulation results show the capability of detecting a 9 mm breast tumor embedded in three different locations inside a female realistic breast phantom. The experimental results demonstrated that the proposed probe has higher sensitivity for detecting the presence of a tumor in thee different locations inside a slice of chicken meat having inhomogeneous dielectric variations. The feature extraction method, PCA, was employed to emphasize and enhance the variation in the probe's response which identity between a normal and tumorous female breast.

# Chapter 5

# Near-field Microwave Dipole Array Sensor for Breast Tumor Detection

## 5.1 Introduction

In this chapter, electrically small four dipole antenna arrays excited by a single port proposed as a microwave sensor for near-field microwave breast tumor detection is presented. Using of antenna array enlarges the sensitivity area as compared to a single element resulting in better detection of tumors located deeply inside breast tissues. The dipole array sensor comprises 4-element identical dipole antenna array fed with a single port. The simulation and experimental results show that the array sensors has a high sensitivity for detecting a breast tumor inserted at different locations and with various sizes.

The advantage of the proposed sensors as compared to previously introduced sensors is that the proposed array sensor is fed by a single-feed point. When compared to multiple-feed points sensors, using a single feeding port sensor array allows for great reduction in the computational cost and complexity that are caused by processing the data from multiple feeding points. In addition, using an array of elements as compared to a single element en-

larges the sensitivity area of the sensor which results in covering the whole breast and therefore eliminating the use of mechanical motors to move the sensor all over the breast. Therefore, the sensitivity of the proposed array sensor is based on the aggregate effect of all elements to form one single but highly sensitive sensor.A summary of the advantages of the proposed sensor for detecting breast tumors compared to the current sensors that are used for MI techniques is presented in Table 5.1.

## 5.2 Sensor design and simulation

The near-field sensor array is comprised of 1×4 electrically small printed dipoles antenna array with identical dimensions and substrate material of overall length L is 123 mm and trace width of W is 30 mm where as the length of each electrically small dipole ld is 30 mm and width wd is 3 mm which hosted on a substrate Rogers material (RO4003C) with a thickness of 1.52 mm and dielectric constant of $\epsilon_r$=3.38 as shown Fig. 5.1. Each dipole is fed through a gap of length g = 1 mm using two vias connected to each arm of the dipole. The two vias penetrate the substrate to connect the loop to a feeding network printed on the bottom face of the substrate. The sensor array is excited by a single port placed on the substrate's bottom face which shares the common ground placed on the top face with dimensions of lg = 40 mm and Wg = 17 mm, as shown in Fig. 5.1(a). A corporate feed network using uniform impedance microstrip lines is designed to distribute the signal to all resonating loop elements as shown in Fig. 5.1(b). The CST [60] optimization tool was used to optimize the width and length of the feed lines so that the sensor array operates at the desired resonance frequency of 1130 MHz. The proposed sensor was fabricated as shown in Fig. 5.1. The measured and simulated reflection coefficients of the proposed sensor array are shown in Fig. 5.2. Strong agreement is observed between the simulation and measurements.

Table 5.1: A qualitative summary of the advantages of the proposed sensor for detecting breast tumors compared to the current sensors that are used in MI techniques.

| Feature | Proposed Sensors | Current sensors that used for MI technology [2, 10, 44, 101] |
|---|---|---|
| Operation Frequency | Low frequency high penetration | High frequency low penetration |
| Bandwidth | Narrow band | Wide band |
| Number of elements | Multiple sensor with one fed | Multiple sensor with multiple fed |
| Simplicity | Simple setup simple processing for detecting tumors | Complex setup complicated processing for reconstructing an image of tumors |
| Immersion medium | No need | need immersion mediums(oil) |
| Cost | Affordable | Costly |
| Comfort | Comfortable and easy to use | Might produce discomfort to patients |
| Potability | Portable Portable | Most of MI systems are fixed |

To see the capability of the proposed array sensor for detecting breast tumor cells, the proposed sensor was simulated with the heterogeneously dense breast phantom model of the ID: 062204 ACR classification: Class No 3 which introduced in chapter2 using CST.

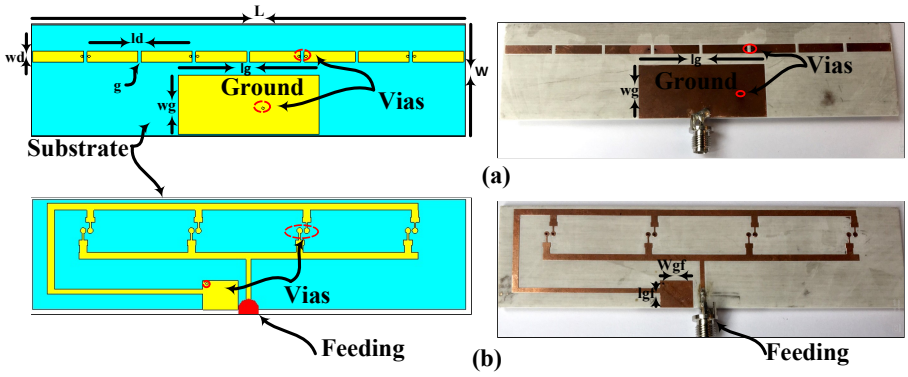


Figure 5.1: The proposed dipole array sensor. (a) Top view shows the loop antenna array elements. (b) Bottom view shows the corporate feed network of the proposed sensor arrays.

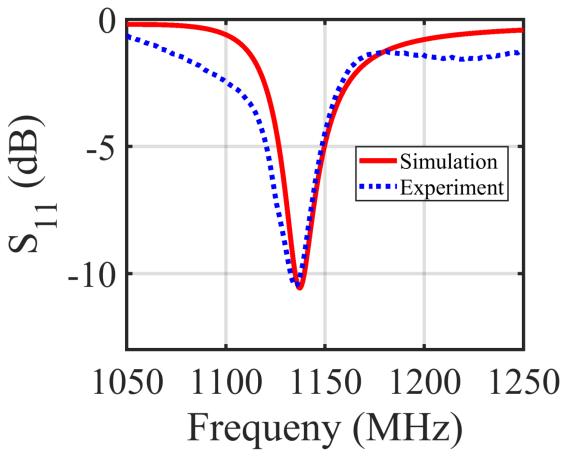


Figure 5.2: The reflection coefficient of the array sensor obtained through (a) simulation and (b) measurement.

First, the proposed sensor array is placed at stand-off distance of 5 mm away from the healthy breast phantom as shown in Fig. 5.3(a). The probe's response was then recorded which included the magnitude and phase of the scattering parameters at the feed point of the array. Next, a tumor of a spherical shape with a diameter of 10 mm was placed at four different locations inside the healthy breast as shown in Fig. 5.4. The dielectric properties

of the inserted tumor was obtained from tumor surgery as presented in [70]. The four locations namely L1, L2, L3, and L4 are labeled according to the distance between the tumor and the sensor where L1 is the nearest location to the center of the sensor, L2 is located at the side of the sensor further away than the first location L1, and L4 is the farthest to the sensor. The sensor response was then recorded for the other breast with the embedded tumor. The data of the sensor response which contains both magnitude and phase is then analysed with and without the tumor to decide whether or not a tumor is present.

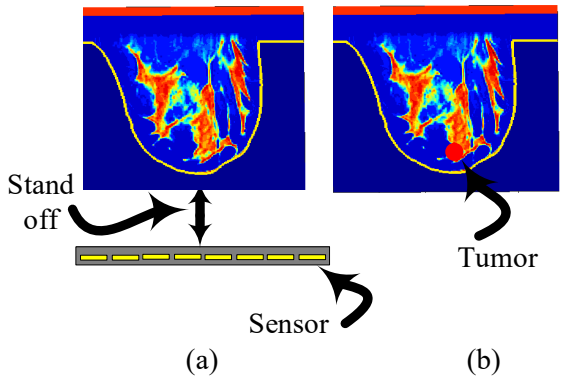


Figure 5.3: Simulation setup: (a) The proposed array dipole sensor at a stand-off distance of 5 mm from 3D normal realistic numerical breast phantom model, and (b) The inserted tumor in the normal numerical breast phantom model.

Once the sensor response of the two examinations, with and without the inserted tumor, at different locations is recorded, the sensor response was extracted and analyzed as shown in Fig. 5.5 and Fig. 5.6. The results of Fig. 5.5 shows the magnitude of $S_{11}$, and Fig. 5.6 shows the phase of $S_{11}$. It is evident from the results that the difference in magnitude and phase of the reflection coefficient of the array sensor between the normal and tumourous case is greater for tumor locations that are close to the sensor.

For more validation of the proposed sensor array, the simulation was

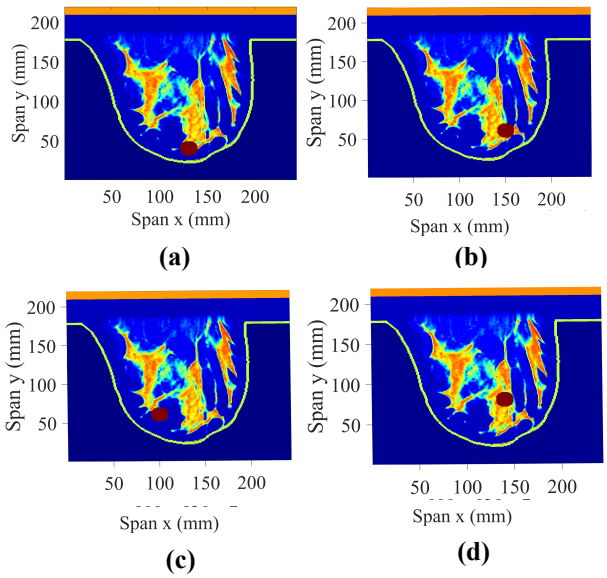


Figure 5.4: Simulation setup of three different tumor locations inside the breast phantom model.The tumor is located at random positions in the breast tissue with size of 10 mm. (a) Tumor located at L1 (x = 130 mm, y = 40 mm, z = 140 mm). (b) Tumor located at L2 (x = 150 mm, y = 60 mm, z = 140 mm). (c) Tumor located at L3 (x = 140 mm, y = 90 mm, z = 140 mm). (d) Tumor located at L4 (x = 150 mm, y = 90 mm, z = 140 mm) .

extended for detecting three different sizes of tumors at a single location. Four different sizes of breast tumors with diameter sizes, namely: 7 mm, 10 mm, 13 mm and 16 mm, are embedded inside the breast phantom to study the capability of the proposed sensor for detecting different sizes of the breast tumors as shown in Fig. 5.3(b). The results are shown in Fig. 5.7 and Fig. 5.8 for the four different tumor sizes. In all the tumor sizes, the probe was capable of detecting the presence of tumor tissues. Obviously from the results, larger tumor sizes are easier to detect, where the shift in the frequency response of both magnitude and phase is noticeable compared with normal case.

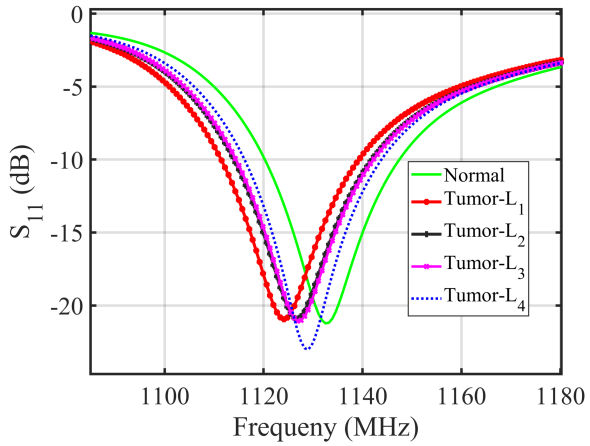


Figure 5.5: Simulation results of the sensor array, magnitude response for the breast phantom model with and without a 10 mm tumor at four different locations.

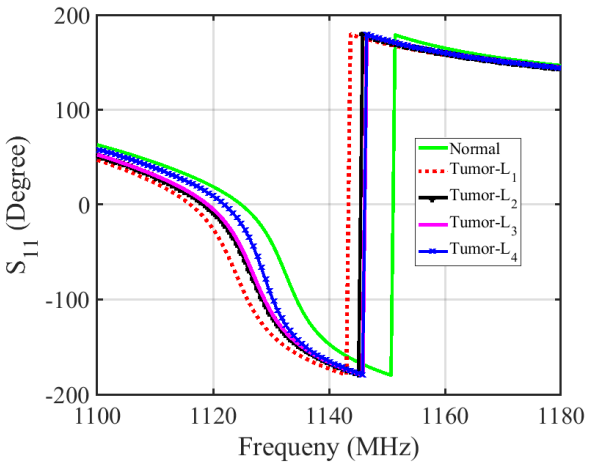


Figure 5.6: Simulation results of the sensor array, phase response for the breast phantom model with and without a 10 mm tumor at four different locations.

## 5.3 Experimental Study

An experiment was performed to test the proposed sensor in an environment that resembles female breast tissues. The fabricated sensor was used

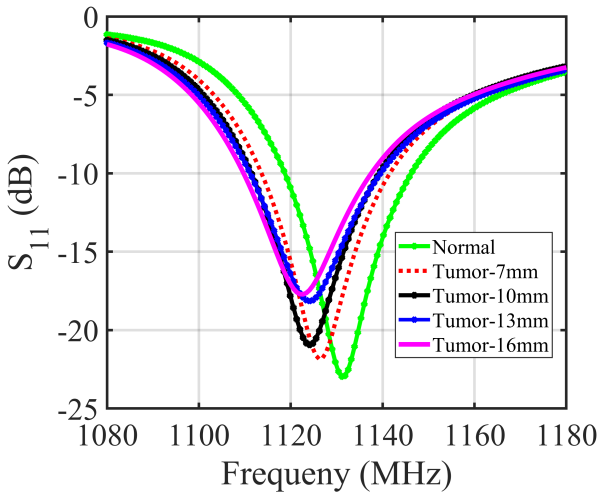


Figure 5.7: Simulation results of the magnitude of reflection coefficient response $S_{11}$ in dB for detecting four different sizes of breast tumors including: 7 mm,10 mm, 13 mm and 16 mm inserted at a fixed location inside the healthy breast phantom.

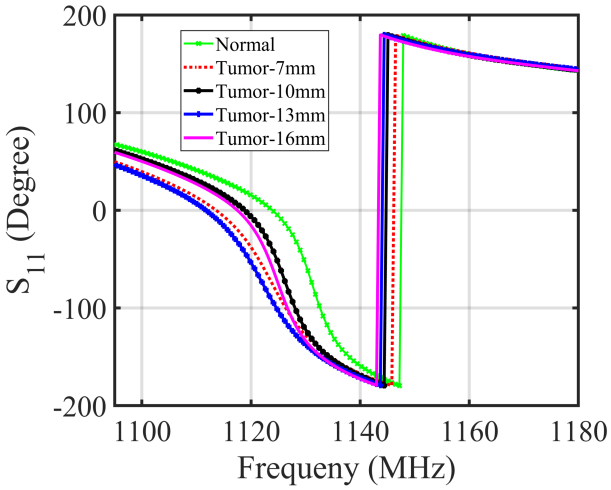


Figure 5.8: Simulation results of the phase of reflection coefficient response $S_{11}$ in degree for detecting four different sizes of breast tumors including: 7 mm,10 mm, 13 mm and 16 mm inserted at a fixed location inside the healthy breast phantom.

to validate the concept experimentally. The measurement setup used in the experiment consists of the sensor, a Victor Network Analyzer (VNA), metal-

lic spheres and tumors made of an oil and gelatine mixture with different diameter sizes (mimicking tumors) and chicken meat as shown in Fig. 5.9 and Fig. 5.10 respectively.

In the experiment, the same test procedure that was employed in the simulation for various tumor locations and sizes is repeated. First, the sensor was tested with the chicken meat which is considered as the normal case of the breast phantom. Second, we placed a 13 mm tumor inside the chicken meat at four different locations which represent the breast phantom with inserted tumors as shown in Fig. 5.11 . The main objective of inserting the 13 mm tumor at four different locations inside the chicken meat is to analyse the capability or the sensitivity of the array sensor for detecting breast tumor at different locations even though the tumor is not facing the area of the sensor. In addition, we can avoid the scan of multiple location for detection the tumor.

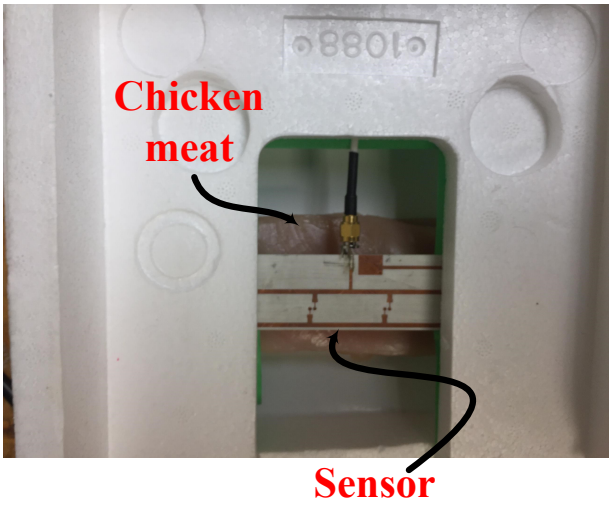


Figure 5.9: Measurement setup showing the proposed sensor with a chicken meat.

The experimental results of the sensor magnitude and phase response when using a tumor sphere (high dielectric spheres ) of size 13 mm inserted in a chicken meat at four different locations are summarized in Fig. 5.12

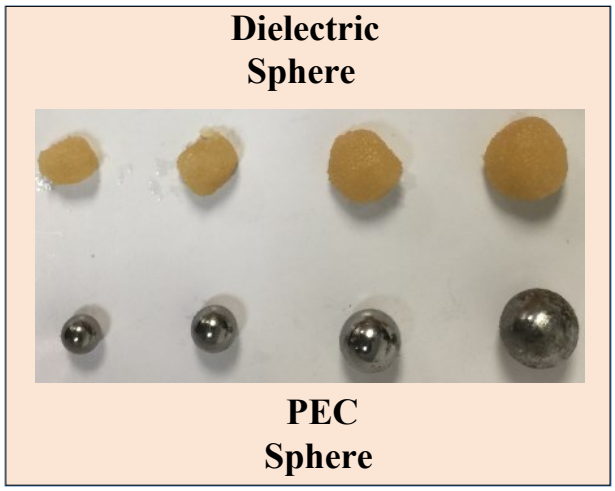


Figure 5.10: View of four different sizes of high conductive (metallic spheres) and high dielectric spheres (oil gelatine mixture spheres).

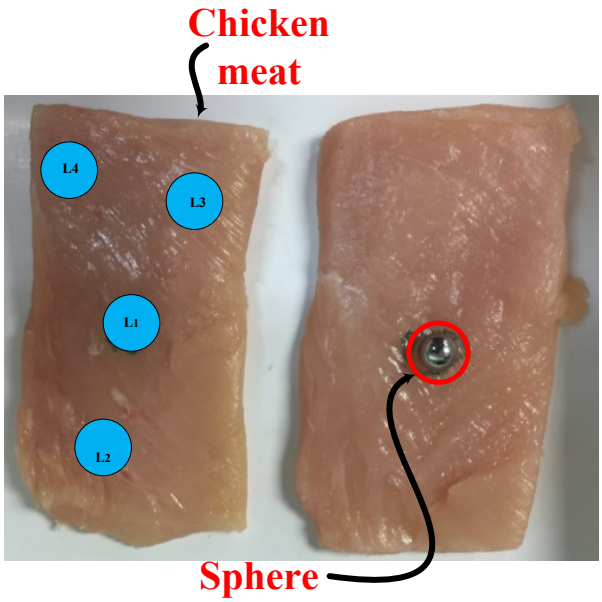


Figure 5.11: Measurement setup showing the process of allocating the tumor of radius 6.5 mm at various locations within the chicken meat.

and Fig. 5.13 respectively. Fig. 5.14 and Fig. 5.15 show the results of the sensor magnitude and phase response when using a metallic sphere (high conductive sphere) of size 13 mm at four different locations.

It is depicted that the sensitivity of the sensor for detecting the sphere at location (L1) where the sphere is located at the center of the sensor is higher than the other locations where the tumor is located off center or the area from the sensors. In addition, the sensor has higher sensitivity for detecting the high dielectric spheres (tumors) than the high conductive metallic spheres.

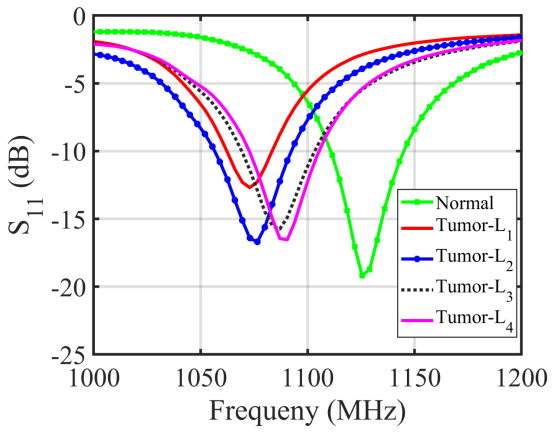


Figure 5.12: Experimental results of the sensor magnitude response when using a tumor of size 13 mm inserted in a chicken meat at four different locations.

Another experiment was performed to test the ability of the proposed sensor to detect various tumor sizes as shown in Fig. 5.10. In the experiment, the metallic spheres and tumors with various radii as indicated in the simulation were inserted inside the chicken meat. Here, the tumors and spheres where located in the same place one at a time. The response of the sensor was recorded for each case and compared to the original case having only chicken meat with no tumor. The magnitude and phase responses of different sizes tumors were analyzed and plotted as shown in Fig. 5.16

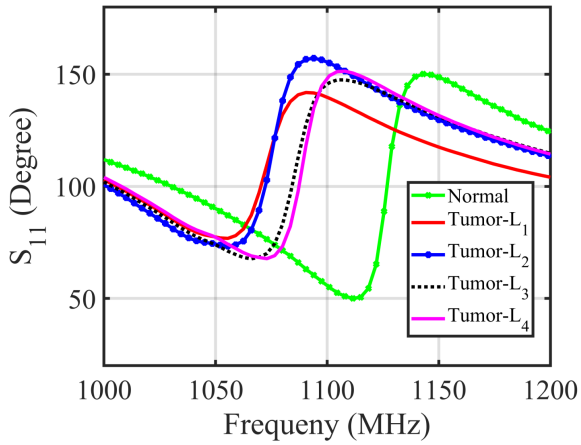


Figure 5.13: Experimental results of the sensor phase response when using a tumor of size 13 mm inserted in a chicken meat at four different locations.

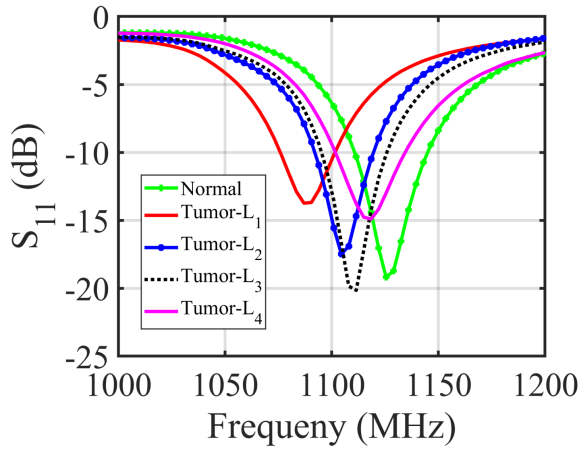


Figure 5.14: Experimental results of the sensor magnitude response when using a metallic sphere of size 13 mm inserted in a chicken meat at four different locations.

and Fig. 5.17. Fig. 5.18 and Fig. 5.19 shows the results of magnitude and phase responses of of different sizes metallic spheres. From the results, we can clearly see that as the tumor size increases, a higher frequency shift is experienced in both the magnitude and phase of the reflection coefficient.

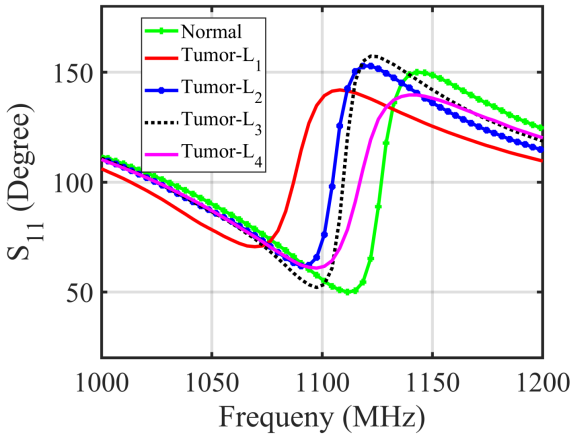


Figure 5.15: Experimental results of the sensor phase response when using a metallic sphere of size 13 mm inserted in a chicken meat at four different locations.

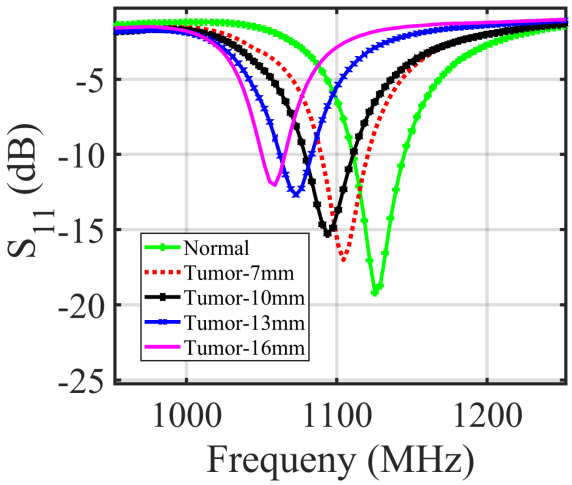


Figure 5.16: Experiment results of the magnitude of reflection coefficient response $S_{11}$ in dB for detecting four different sizes of breast tumors including: 7 mm,10 mm, 13 mm and 16 mm inserted at a fixed location inside the chicken meat phantom.

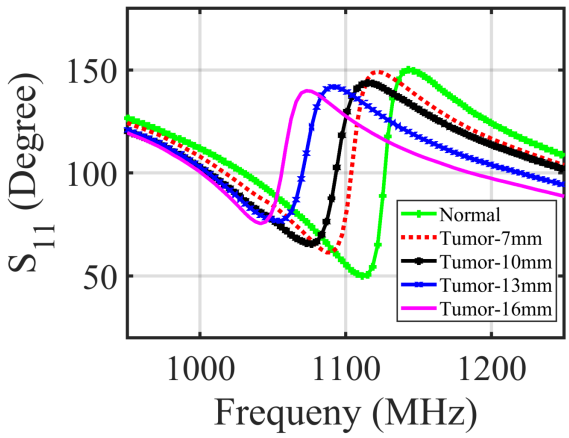


Figure 5.17: Experiment results of the phase of reflection coefficient response $S_{11}$ in dB for detecting four different sizes of breast tumors including: 7 mm,10 mm, 13 mm and 16 mm inserted at a fixed location inside the chicken meat phantom.

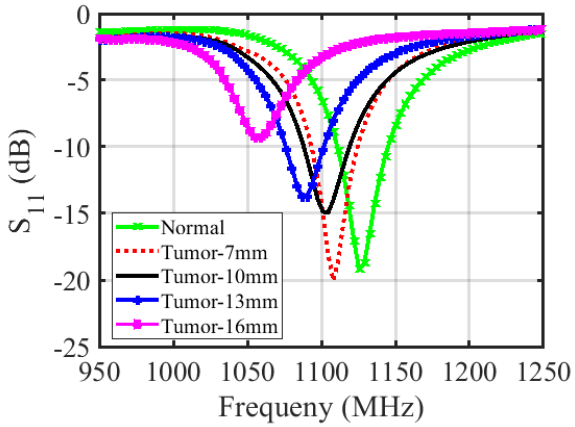


Figure 5.18: Experiment results of the magnitude of reflection coefficient response $S_{11}$ in dB for detecting four different sizes of metallic spheres including: 7 mm,10 mm, 13 mm and 16 mm inserted at a fixed location inside the chicken meat phantom.

## 5.4 Conclusion

A near-field dipole array sensor was introduced for detecting breast tumors. Numerical and experimental tests were used to validate the proposed detec-

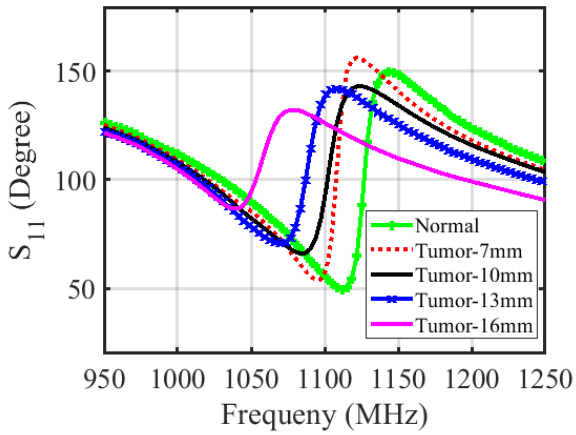


Figure 5.19: Experiment results of the phase of reflection coefficient response $S_{11}$ in dB for detecting four different sizes of metallic spheres including: 7 mm,10 mm, 13 mm and 16 mm inserted at a fixed location inside the chicken meat phantom.

tion methodology. This was achieved by testing the proposed sensor with a breast phantom having tumors placed at four different locations and of various sizes. Measurements were carried out on chicken meat. The results showed a high sensitivity of the proposed sensor which can indicate the existence of an anomaly, that resembles a tumor, inside chicken meat having inhomogeneous material composition.

# Chapter 6

# Near-field Microwave Loop Array Sensor for Breast Tumor Detection

## 6.1 Introduction

This chapter presents a novel sensor based on loop antenna arrays excited by a single port, that is to be used for near-field microwave breast tumor detection. The proposed sensor comprises 4-element identical loop antenna array fed with a single port, that is to be utilized for improving the sensitivity area as compared to a single loop sensor resulting in better detection of tumors located deeply inside breast tissues. Numerical simulations have been conducted using a numerical breast model with and without tumor cells placed in the near-field of the sensor. The sensor is capable of detecting a breast tumor inserted at five different locations and with various sizes. An experimental validation was conducted using a glass box filled with vegetable oil and metallic spheres that resembles healthy and tumourous breast tissues, respectively. The simulation and experimental results show that the array sensor has a high sensitivity for detecting a metallic sphere placed at five different locations inside a dielectric medium as well as detecting variable sizes of the metallic spheres.

## 6.2 Sensor design and simulation

The near-field sensor array comprises of 1×4 loop antenna array with identical dimensions and substrate material having an overall length of L = 125 mm and width of W = 51 mm. Each element has a side length of ld = 30 mm and the array was hosted on a substrate of Rogers material (RO4003C) with a thickness of 1.52 mm and a relative permittivity of $\epsilon_r$=3.38 as shown Fig. 6.1. Each small loop is fed through a gap of length g = 1 mm using two vias connected to each arm of the loop. The two vias penetrate the substrate to connect the loop to a feeding network printed on the bottom face of the substrate. The sensor array is excited by a single port placed on the substrate's bottom face which shares the common ground placed on the top face with dimensions of Lg = 40 mm and wg = 17 mm, as shown in Fig. 6.1(a). A corporate feed network using uniform impedance microstrip lines was designed to distribute the signal to all resonating loop elements as shown in Fig. 6.1 (b). The CST [60] optimization tool was used to optimize the width and length of the feed lines so that the sensor array operates at the desired resonance frequency of 1.108 GHz.

The proposed sensor was fabricated as shown in Fig. 6.1(b). The measured and simulated reflection coefficients of the proposed sensor array are shown in Fig. 6.2. Strong agreement is observed between the simulation and measurements.

To see the ability of the proposed sensor for detecting breast tumor cells, the proposed sensor was simulated with the Heterogeneously Dense Breast phantom model of the ID: 012204" ACR classification: Class 2 in CST.

First, the proposed sensor array is placed at stand-off distance of 5 mm away from the healthy breast phantom as shown in Fig. 6.3(a). The probe's response was then recorded which included the magnitude and phase of the scattering parameters at the feed point of the array. Next, a tumor of a spherical shape with a diameter of 7 mm was placed at five different

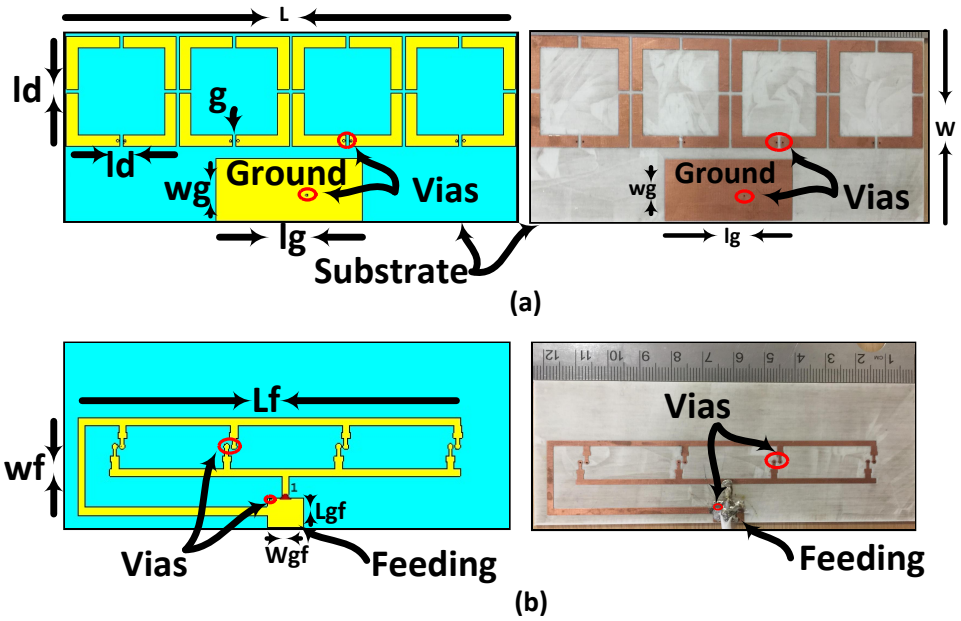


Figure 6.1: The proposed loop array sensor. (a) Top view shows the loop antenna array elements. (b) Bottom view shows the corporate feed network of the proposed sensor arrays.

locations inside the healthy breast as shown in Fig. 6.3(b). The five locations namely L1, L2, L3, L4 and L5 are labeled according to the distance between the tumor and the sensor where L1 is the nearest location to the center of the sensor, L2 is located at the side of the sensor further away than the first location L1, and L5 is the farthest to the sensor. The sensor response was then recorded for the other breast with the embedded tumor. The data of the sensor response which contains both magnitude and phase is then analysed with and without the tumor to decide whether or not a tumor is present.

Once the sensor response of the two examinations, with and without the inserted tumor, at different locations is recorded, the sensor response was extracted and analyzed as shown in Fig. 6.4 and Fig. 6.5. The results of Fig. 6.5 shows the magnitude of $S_{11}$, and Fig. 6.5 shows the phase of $S_{11}$. It is evident from the results that the difference in magnitude and phase of

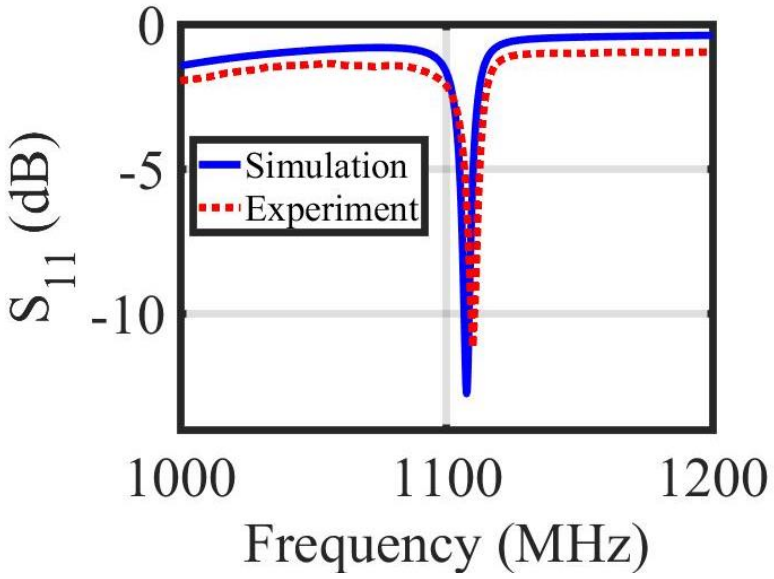


Figure 6.2: The reflection coefficient of the array sensor obtained through simulation and measurement.

the reflection coefficient of the probe between the normal and tumourous case is greater for tumor locations that are close to the sensor.

$$\Delta Decision = S_{11}Right - S_{11}left \tag{6.1}$$

The sensitivity of the sensor is based on the value of the $\Delta$ Decision given in equation 6.1. If the value of $\Delta$ Decision is high, this indicates a high differences in the sensor response of both normal breast and breast with inserted tumor. The results show that the $\Delta$ Decision is higher when using the phase of $S_{11}$ as compared with $\Delta$ Decision of the magnitude of $S_{11}$.

For more validation of the proposed sensor array, the simulation was extended for detecting three different sizes of tumors at a single location. Three different sizes of breast tumors with diameter sizes, namely: 7 mm,

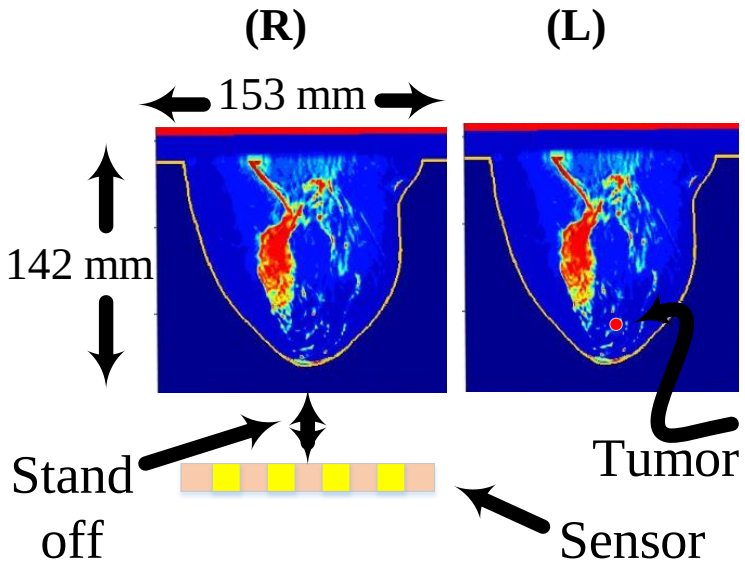


Figure 6.3: Simulation setup: (a) The proposed array loop sensor at a stand-off distance of 5 mm from 3D normal realistic numerical breast phantom model in CST, and (b) The inserted tumor in the normal numerical breast phantom model.

15 mm, and 20 mm, are embedded inside the breast phantom to study the capability of the proposed probe for detecting different sizes of the breast tumors as shown in Fig. 6.3(b). The results of the magnitude and phase of reflection coefficient response are shown in Fig. 6.6 and Fig. 6.7 for the three different tumor sizes respectively. In all the tumor sizes, the probe was capable of detecting the presence of tumor tissues. Obviously from the results, larger tumor sizes are easier to detect, where the shift in the frequency response of both magnitude and phase is noticeable compared with normal case.

Since a breast tumor has a higher conductivity and permittivity as compared with its surrounding healthy tissues, a higher electric field intensity is observed in the proximity of the breast tumor in comparison with the surrounding normal tissues. Fig. 6.8 (a) and Fig. 6.8 (b) show the distribution

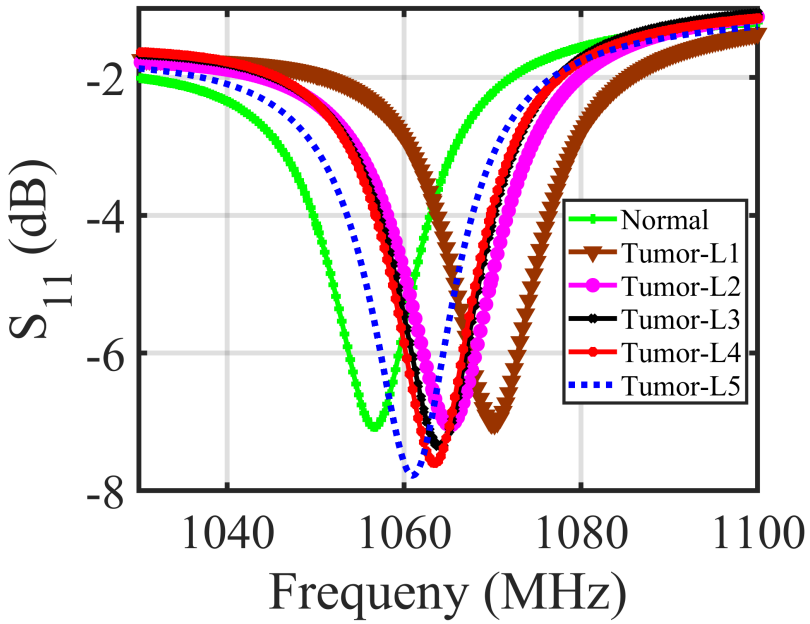


Figure 6.4: Simulation results of the magnitude of the sensor's reflection coefficient response for the breast phantom model with and without a 7 mm tumor at five different locations.

of the electric field inside a normal breast phantom and a breast phantom with a 15 mm tumor, respectively.

## 6.3 Experimental Validation

An experiment was conducted to further validate the obtained simulated results based on the numerical breast phantoms. In the experiment, a glass box filled with vegetable oil [102]- [103] and a metallic sphere were used to mimic a normal and tumourous breast phantom, respectively. The fabricated sensor was placed at a distance of 5 mm away from the class box as shown in Fig. 6.9 (a).

In the experiment, the same test procedure that was employed in the

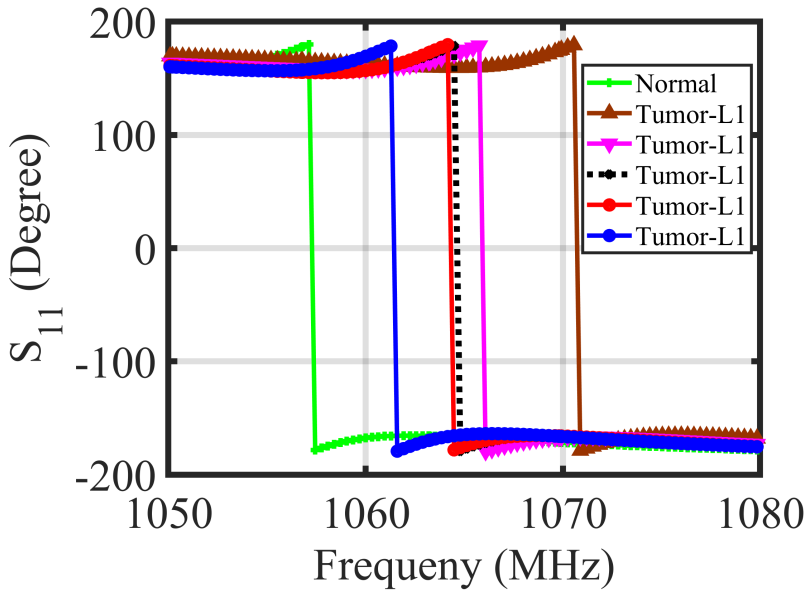


Figure 6.5: Simulation results of the phase of the sensor's reflection coefficient response for the breast phantom model with and without a 7 mm tumor at five different locations.

simulation for various tumor locations and sizes is repeated. First, the sensor was tested with the glass box filled with vegetable oil which is considered as the normal case [102] of the breast phantom. Second, we placed a 7 mm metallic sphere inside the glass box at five different locations which represent the breast phantom with inserted tumors as shown in Fig. 6.9 (b).

The objective of inserting the 7 mm metallic sphere at five different locations inside the glass box is to analyse the capability or the sensitivity of the array sensor for detecting breast tumor at different locations even though the tumor is not facing the area of the sensor. The obtained results of the magnitude and phase of reflection coefficient response for different sphere locations are summarized in Fig. 6.10 and Fig. 6.11 respectively.

It is depicted that the sensitivity of the sensor for detecting the sphere at location (L1) where the sphere is located at the center of the sensor

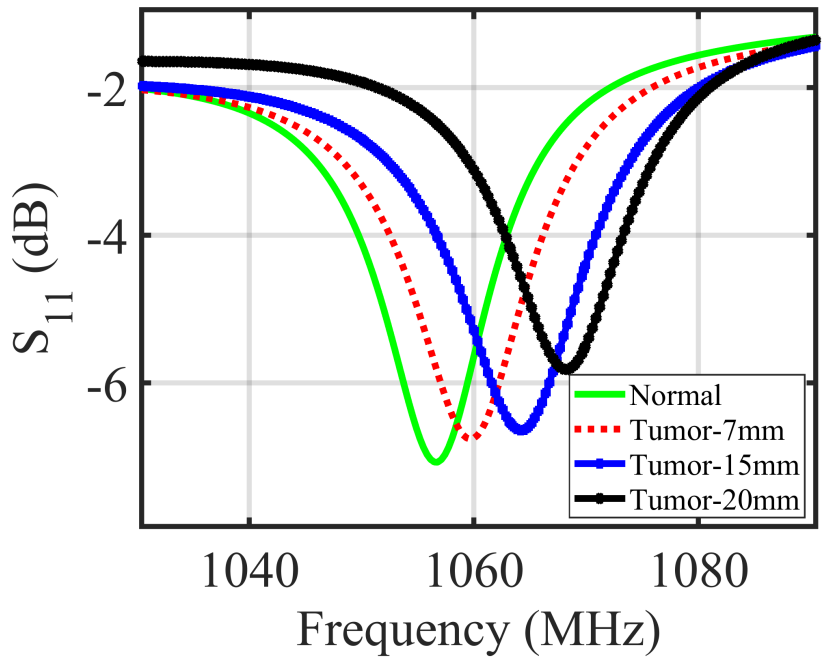


Figure 6.6: Simulation results of the magnitude of reflection coefficient response $S_{11}$ in dB for detecting three different sizes of breast tumors including: 7 mm, 15 mm and 20 mm inserted at a fixed location inside the healthy breast phantom.

is higher than the other locations where the tumor is located off center from the sensors prospective. It is also noticeable that at location L1, the separation in the sensor's response between the normal and the tumorous case increases, indicating a more pronounced detection as translated by a larger frequency shift. Moreover, the separation in the sensor's response between the cases with and without the sphere is more pronounced for both the magnitude and phase of the $S_{11}$ of the array sensor.

The experiment was extended to detecting three different sizes of metallic spheres including 7 mm, 15 mm and 20 mm, placed at the center location (L1), one at a time to investigate the sensitivity of the sensor when detecting different sizes of tumors with a standoff distance of 5 mm and 10 mm.

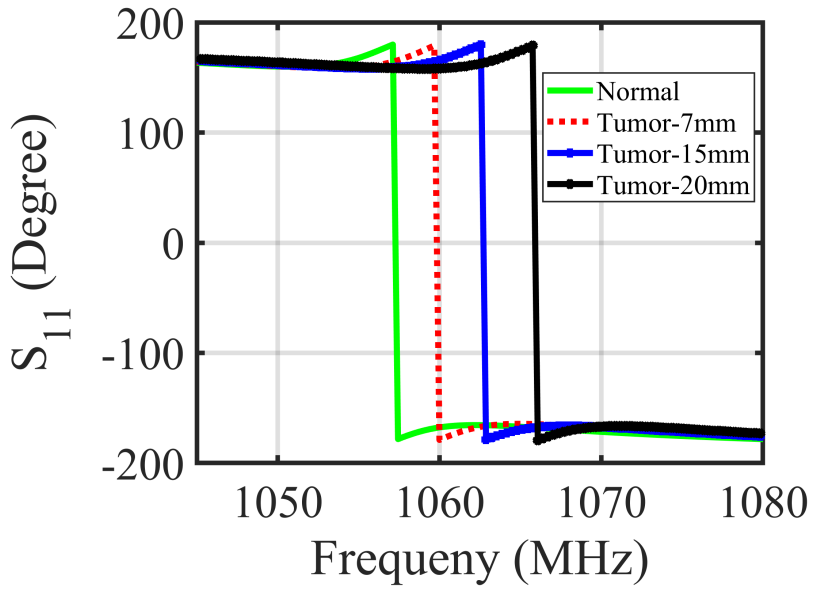


Figure 6.7: Simulation results of the phase of reflection coefficient response $S_{11}$ in degrees for detecting three different sizes of breast tumors including: 7 mm, 15 mm and 20 mm inserted at a fixed location inside the healthy breast phantom.

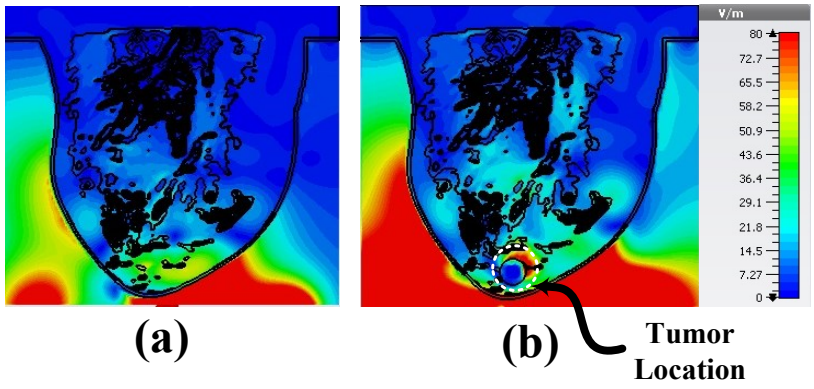


Figure 6.8: Simulation results of the electric field distribution: (a) Normal breast phantom model, and (b) Breast phantom model with an inserted 15 mm tumor.

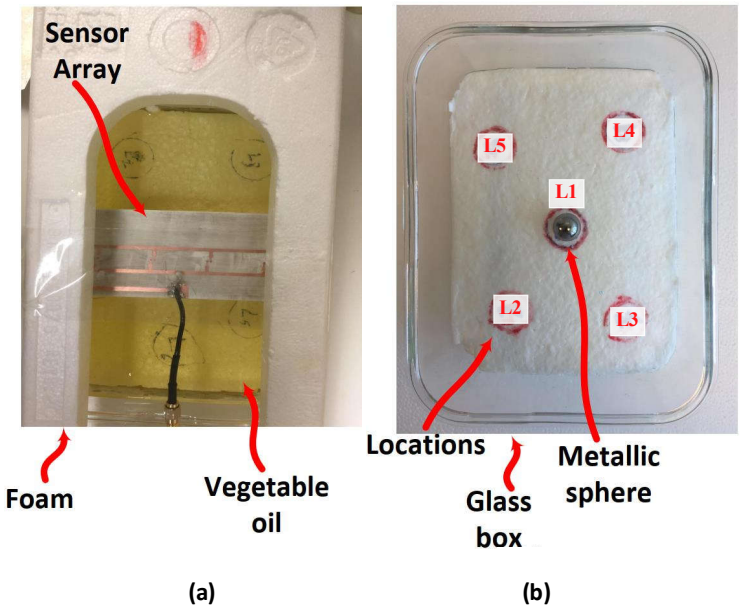


Figure 6.9: Experiment setup: (a) The fabricated loop array sensor at stand-off distance of 5 mm from the glass box filled with vegetable oil, and (b) A photo showing the experimental procedures of a 7 mm metallic sphere placed at five different locations inside the class box.

Fig. 6.12 and Fig. 6.13 show the experimental results of the sensor magnitude and phase response for standoff distance of 5 mm respectively. Fig. 6.14 and Fig. 6.15 show the experimental results of the sensor magnitude and phase response for standoff distance of 10 mm respectively.

The results show that the sensitivity of the sensor for detecting large sphere (20 mm) is higher than the smaller sizes. Consistent conclusion was obtained in the experiment as compared to the simulations in terms of the sensitivity of the sensor to different tumor sizes. For all the tumor sizes, the sensor was capable of detecting the presence of tumorous tissues. Obviously from the results, larger tumor sizes are easier to detect. In addition, as the tumor size increases, the difference in the sensor's response between the normal and tumorous cases increases. It is evident from the results that there is a clear distinction in the magnitude and phase of the sensor between

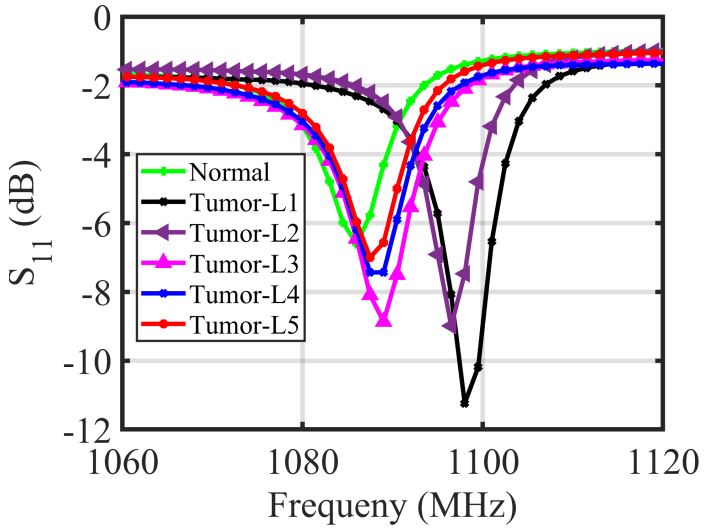


Figure 6.10: Experimental results of the sensor magnitude response ($S_{11}$ in dB) when using a metallic sphere of size 7 mm inserted in a glass box filled with vegetable oil at five different locations.

the normal case of the glass box filled with vegetable oil without the metallic spheres and the cases of inserted three different sizes of metallic spheres, one at a time, for both standoff distance of 5 mm and 10 mm. However, the sensitivity of the sensor for detecting different sizes spheres at standoff distance of 5 mm is higher than the sensitivity of the sensor at standoff distance of 10 mm.

## 6.4 Conclusion

In this work, we introduced a new array sensor for detecting human female breast tumors using a microwave near-field technique. The array sensor has the advantages of detecting breast tumors at different locations with different sizes inside the breast phantom. The sensitivity of the sensor for

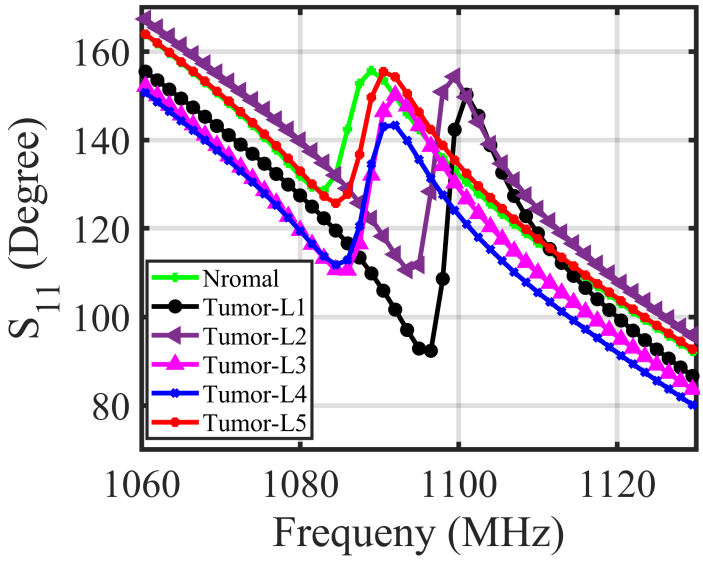


Figure 6.11: Experimental results of the sensor phase response ($S_{11}$ in degree) when using a metallic sphere of size 7 mm inserted in a glass box filled with vegetable oil at five different locations.

detecting the breast tumors is enhanced when using multiple sensor elements which results in increasing the coverage area of the sensor.

The array sensor concept is validated through numerical and experimental tests by detecting tumors placed at different locations with various sizes. From the obtained results, it can be concluded that the sensor is capable of detecting tumors of diameter size as small as 7 mm placed inside female realistic breast tissues. In addition, experimental results demonstrate the high sensitivity of the sensor through detecting the presence of a tumor inside a glass box filled with vegetable oil. The shift in the sensor response of both magnitude and phase of the reflection coefficients was successfully employed to distinguish between a healthy and tumorous female breast.

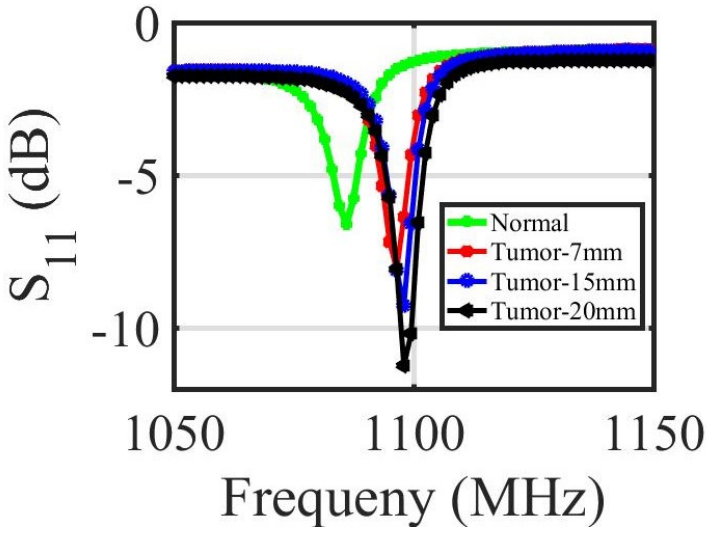


Figure 6.12: Experimental results of the sensor magnitude response ($S_{11}$ in dB)when using three different sizes of metallic spheres (7 mm, 15 mm and 20 mm) embedded at a single location inside a glass box filled with vegetable oil at stand off distance of 5 mm.

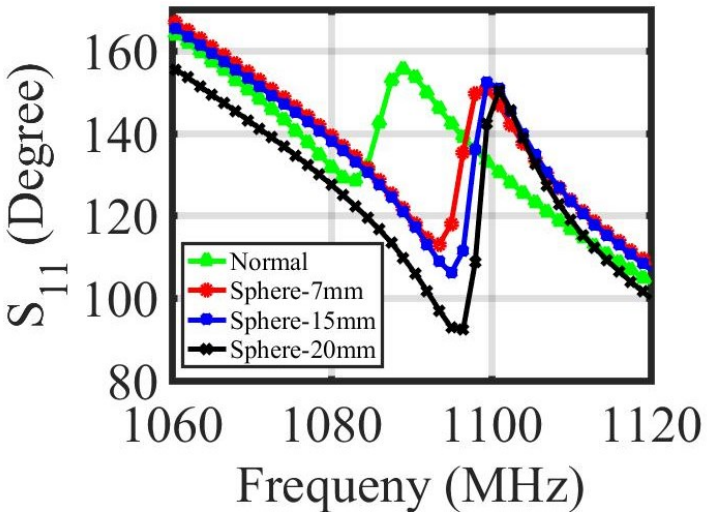


Figure 6.13: Experimental results of the sensor phase response ($S_{11}$ in degree) when using three different sizes of metallic spheres (7 mm, 15 mm and 20 mm) embedded at a single location inside a glass box filled with vegetable oil at stand off distance of 5 mm.

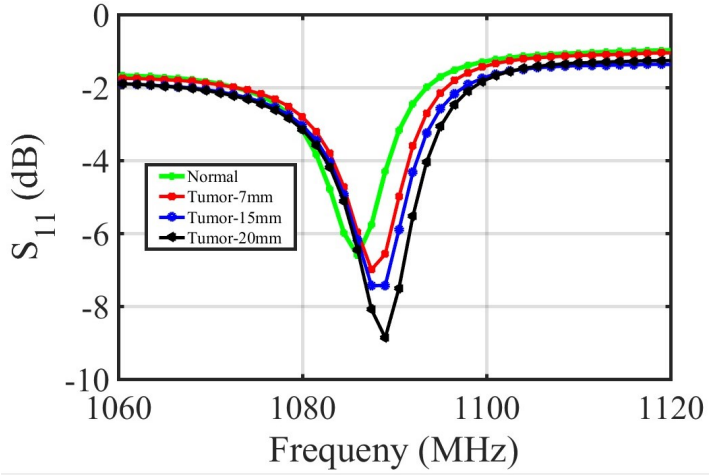


Figure 6.14: Experimental results of the sensor magnitude response ($S_{11}$ in dB)when using three different sizes of metallic spheres (7 mm, 15 mm and 20 mm) embedded at a single location inside a glass box filled with vegetable oil at stand off distance of 10 mm.

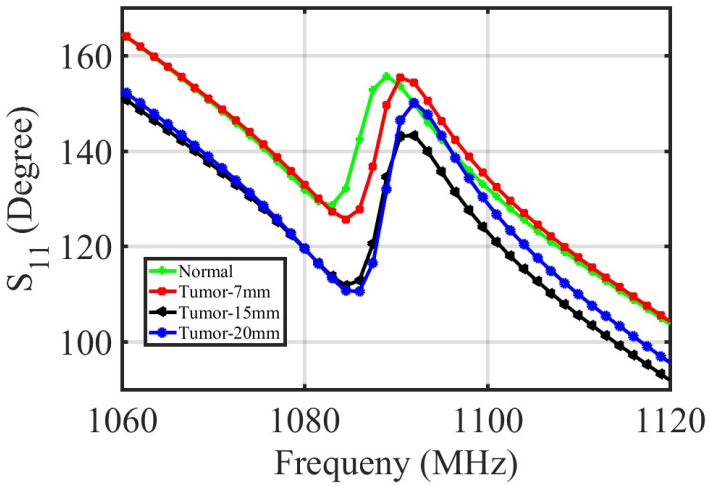


Figure 6.15: Experimental results of the sensor phase response ($S_{11}$ in degree) when using three different sizes of metallic spheres (7 mm, 15 mm and 20 mm) embedded at a single location inside a glass box filled with vegetable oil at stand off distance of 10 mm.

# Chapter 7

# Near-field Metasurface Sensor for Breast Tumor Detection

## 7.1 Introduction

A breast cancer detection modality is introduced whereby a near-field array sensor operating in the microwave regime is used statically to identify the presence of a breast tumor. In a departure from conventional near-field sensors, the sensor is a metasurface comprising an array of 8×8 electrically-small resonating elements. The elements of the metasurface are designed to respond to both electric and magnetic fields. This enables the metasurface to emphasize seemingly small changes in the composition of the electric and magnetic fields in its environment, thus leading to a higher overall sensor sensitivity. Furthermore, unlike previous near-field probes, the overall metasurface sensor is not electrically small, which means that it provides a larger sensing surface while maintaining the effectiveness of near-field probes in the sense of detecting material changes in the near proximity of the sensor. Numerical simulations and experiments show that the proposed metasurface has higher sensitivity than previously proposed probes for breast cancer detection

## 7.2 Metasurfaces and its Potential for Sensing

Metamaterials are artificial materials which have the electromagnetic properties that show a highly sensitive response to the dielectric media [104,105]. Metasurfaces (MSs) are two-dimensional (2D) metamaterial planar surfaces that consisting of few layers with sub-wavelength thickness and provide excellent abilities for achieving a control over the amplitude, phase, and polarization of electromagnetic wave [106]. Scientists use the metamaterials to develop microwave sensors that have a great interest in many biomedical application, such as cancer detection field [104].

In [107–109] and practically all sensors used in previous works for either material detection or characterization in general, different types of antennas used as microwave sensors were employed for transmitting and receiving such as dipoles or loops, or possibly resonating antennas [2, 110–114]. The main objective of those sensors for microwave breast tumor detection was to sending and receiving microwave signals through and from the female human breast. Since breast tumors can develop at different locations inside the breast, microwave sensors need to couple appreciable energy to the entire breast volume. Some studies used multiple sensors array with multiple feeds to enhance the sensitivity of the microwave detection systems [110]– [114]. Most of the microwave systems that were used for microwave breast cancer detection have some limitations such as complexity, high cost, the use of matching liquid and complex coding for image processing [47]– [116].

In chapter 4 , a single magnetic dipole consisting of a loop with four symmetrical gaps was proposed for breast tumor detection [108]. The idea behind the use of a magnetic dipole, which emits a magnetic field with much higher amplitude than that of an electric field, is that a tumor not only has higher dielectric properties than the surrounding healthy tissues but also has higher conductivity. Such high conductivity contrast is expected to be more sensitive to a magnetic dipole when placed in its close proximity. However,

the loop needs to be scanned across the breast volume since the size of the sensitive part of the loop (i.e., the gaps of the loop) is much smaller than the breast volume. To increase the sensitivity area of the probe, a four-loop linear array fed by a single port was introduced in chapter 6. This array sensor improved the sensitivity of detecting a breast tumor in different locations within the breast; however the sensitivity of the sensor for detecting a tumor located off center or out of the covered area of the sensor is less than that of the sensitivity of the sensor when detecting a tumor placed at the center or under the covered area of the sensor [109].

In this chapter, we propose a metasurface sensor for detecting sub-surface anomalies but specifically to detect benign and cancerous tumors in human female breast tissues. The metasurface consists of an array of 8×8 electrically-small (subwavelength scale) elements. Each element consists of a dipole and a loop producing electric and magnetic fields, thus enhancing the sensitivity of the probe to changes in both the dielectric and magnetic properties of the sensed medium. The array nature of the sensor provides the ability to sense a larger area than previously introduced probes.

## 7.3 Array Sensor Design Methodology

The single unit cell of the proposed metasurface sensor consists of a loop with an embedded dipole in the middle, a dielectric substrate backed by a reflector and a port connecting the top and bottom layers through a via as shown in Fig. 7.1. The cell dimensions were chosen such that it operates at 2.5 GHz with L=22 mm, d=7.8 mm, g=0.4 mm, s=0.5 mm and copper thickness of t=35 $\mu m$. The unit cell was hosted on top of a Rogers RO4003C dielectric substrate having a $tan\delta$=0.0027 and a dielectric constant of $\epsilon_r$=3.38 with a thickness of a 1.524 mm. Each unit cell was fed by a port placed in shunt through a via with an impedance of 175 Ω

as shown in Fig. 7.1. The unit cell was simulated using CST Microwave Studio [60].

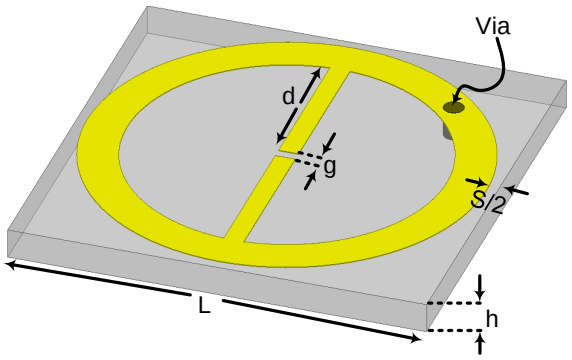


Figure 7.1: A schematic showing a single element of the proposed metasurface.

The cell was first excited by a waveguide with Perfect Electric Conducting (PEC) walls along the X-axes and Perfect Magnetic Conducting (PMC) walls along the Y-axes to ensure a plane wave excitation. The top and bottom sides of the waveguide were assigned wave ports with a power level of 0.5 W as shown in Fig. 7.2. Simulation results for the reflection and absorption coefficients are shown in Fig. 7.3.

The near-field metasurface sensor consists of a periodic array of identical 8×8 cells and a dielectric substrate as described above. A single port located on the third layer was used to excite the metasurface array as shown in Fig. 7.4. The third layer contains a cooperative feed that distribute the energy equally to all of the 64 unit cells. A ground plane is placed at the second layer which is shared between the resonators' layer and the feeding network layer. A single stub matching circuit was used to ensure strong impedance matching between the 50 Ω coaxial feed line and the corporate feed network.

The sensor array was fabricated according to the above design with a schematic shown in Fig. 7.5 (a), (b) and (c). The simulated and measured

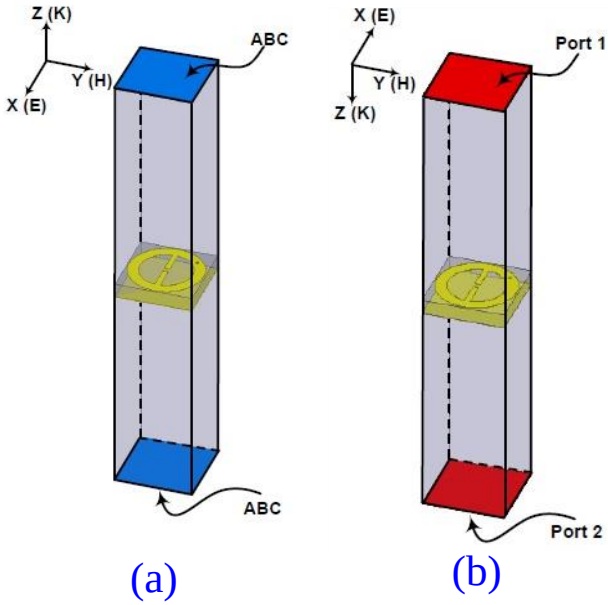


Figure 7.2: The simulation setup showing the proposed unit cell of the metasurface sensor placed inside a waveguide with periodic boundary condition. (a) transmitting mode, and (b) receiving mode.

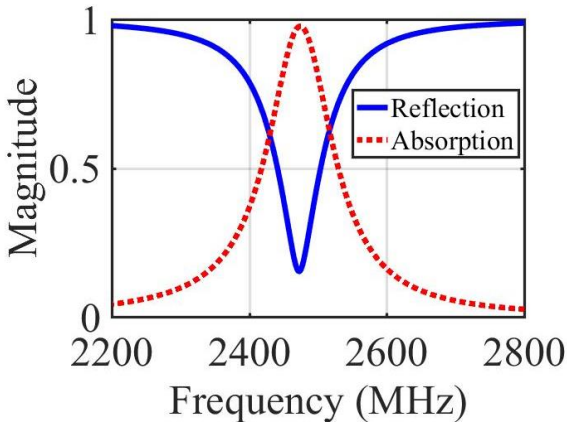


Figure 7.3: Simulation results for the reflection and absorption coefficients of the unit cell.

reflection coefficients of the sensor are shown in Fig. 7.5 (d)

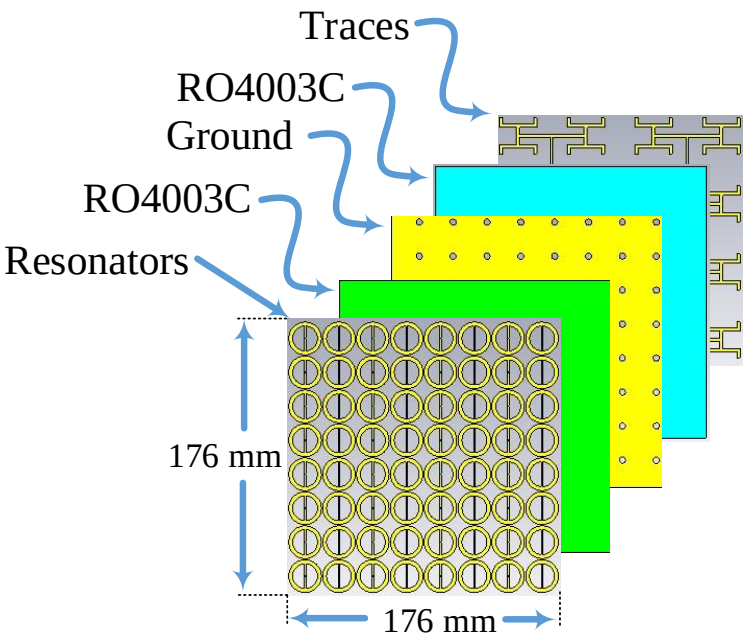


Figure 7.4: Architecture of the metasurface sensor array. The multi-layers comprising the sensor including the resonating cells, the Rogers RO4003C first substrate, the copper ground plane, the Rogers RO4003C second substrate, and the transmission line traces of the optimized feed network.

## 7.4 Simulation Verification for Breast Tumor Detection

The designed sensor array was simulated in the presence of a realistic human female breast phantom to test its ability to detect the existence of breast tumor. The class of breast phantoms used in this chapter is the Heterogeneously Dense Breast which introduced in chapter 2.

The detection modality proposed in this work is based on the following medical fact: (1) Women breasts have material composition that are symmetric in shape and content [94, 95], and (2) it is highly unlikely for a

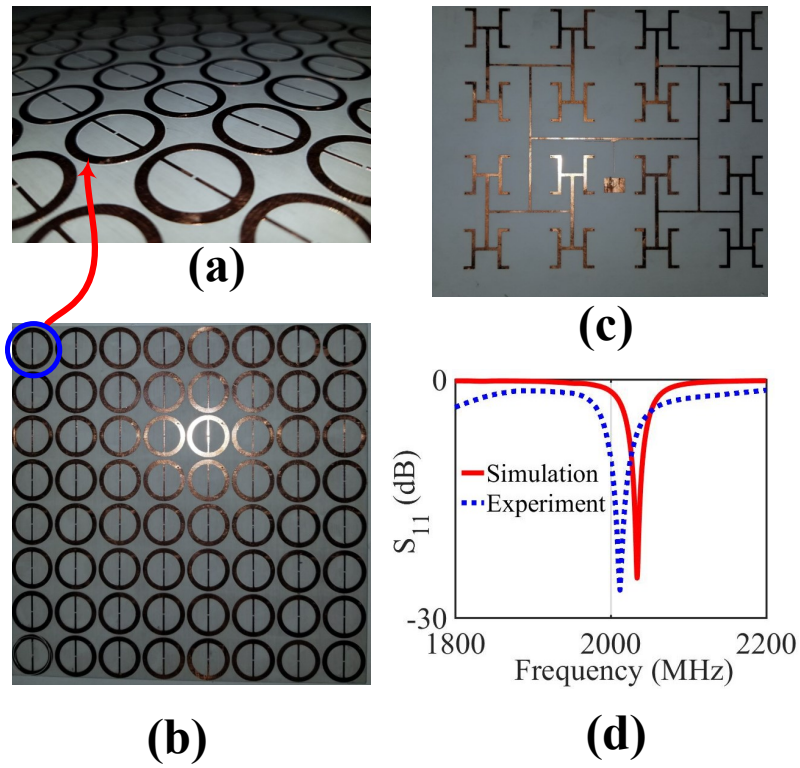


Figure 7.5: Photograph of the fabricated array sensor. (a) Perspective view, (b) bottom view, (c) top view, and (d) magnitude of $S_{11}$.

woman to develop tumors in both breast simultaneously having the same size, shape and location [94]. The responses of the sensor is recorded (phase and magnitude of the reflection coefficients) for both breast. This is done by placing two identical probes in close proximity to the breast so that the near field of the probe can interact with the entire volume of the breast. Because of the symmetry between the left and right breasts, identical probes' response would indicate that the breasts are free of tumors. Any differences in the reading can indicate the likelihood of tumor being developed in either breasts that can be benign or cancerous.

A numerical realistic breast phantom was analyzed and tested with the

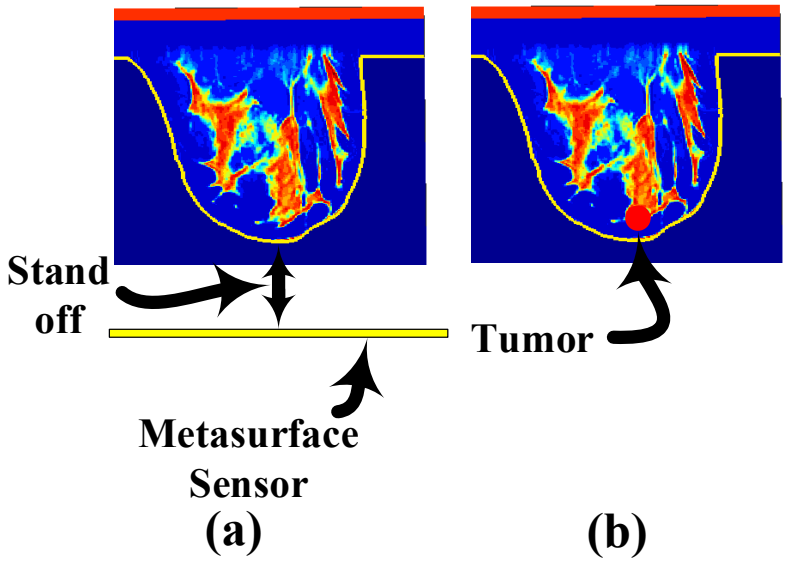


Figure 7.6: A schematic showing the 3D model of the breast phantom (a) normal breast phantom (b) abnormal breast phantom having a tumor of 10 mm diameter and positioned above the metasurface sensor.

metasurface array sensor.In the simulation, the distance between the metasurface and the breast phantom was varied at three distance off 5 mm, 10 mm and 15 mm to ensure that the near field of the probe interacts with the entire volume of the breast as shown in Fig. 7.6. The magnitude and phase of the probe were then recorded over a frequency range from 1940 to 2050 MHz. A tumor with a radius of 5 mm was then placed at fixed locations inside the same breast phantom. The three distance off d1, d2 and d3 are labeled depending on the distance between the metasurface and the breast phantom where d1 is the closest location from the sensor, d2 further away than that of the first location and d3 is the farthest among the three positions with reference to the metasurface. The sensor's response was then recorded with a range of frequencies for both magnitude and phase. The obtained data is then analyzed with and without the existence of a tumor

to record the changes in the probe response and decide whether a tumor is present or not.

The probe's response of the two experiments with and without a tumor (positioned at different distance off) were recorded as shown in Fig. 7.7,Fig. 7.8 and Fig. 7.9. From these figures, it is clear that the proposed metasurface was sensitive to the presence of breast tumors at varies standoff the breast phantom. As would be expected, the shift in the frequency response of the probe is more pronounced when the breast phantom is closer to the surface of the sensor.

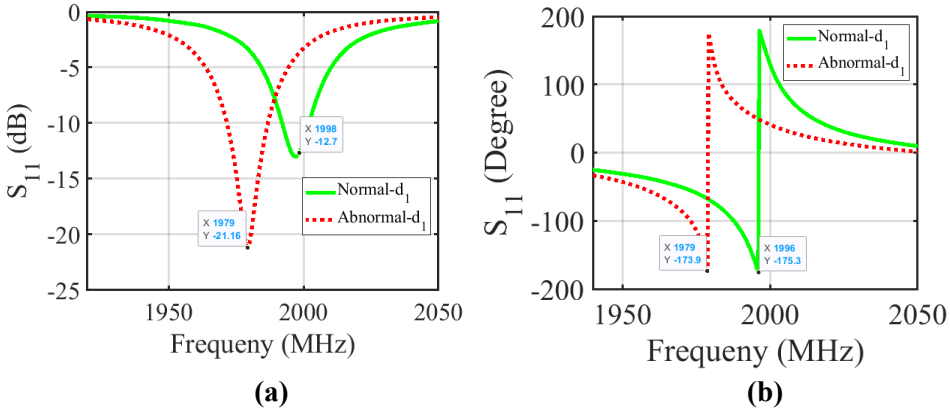


Figure 7.7: Numerical results of the 3D breast phantom with and without the presence of a tumor having a radius of 5 mm and a stand off distance of d1 = 5 mm. (a) The magnitude of $S_{11}$ (dB), and (b) the phase of $S_{11}$ (Degree).

Fig. 7.10 shows the distribution of the power flow inside a normal breast phantom in addition to a breast phantom with a 10 mm diameter tumor at three different stand off distances d1, d2 and d3, respectively. Results show that at stand off distance of d1, higher power flow is concentrated within the the breast content as compared to the other stand off distances (d2 and d3). This is due to the strong nearfield coupling between the sensor array and the breast which is higher for smaller stand off distances.

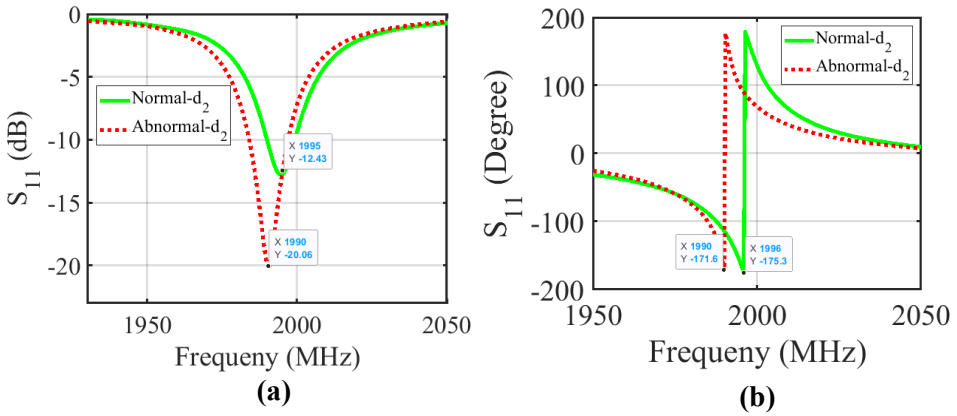


Figure 7.8: Numerical results of the 3D breast phantom with and without the presence of a tumor having a radius of 5 mm and a stand off distance of d1 = 10 mm. (a) The magnitude of $S_{11}$ (dB), and (b) the phase of $S_{11}$ (Degree).

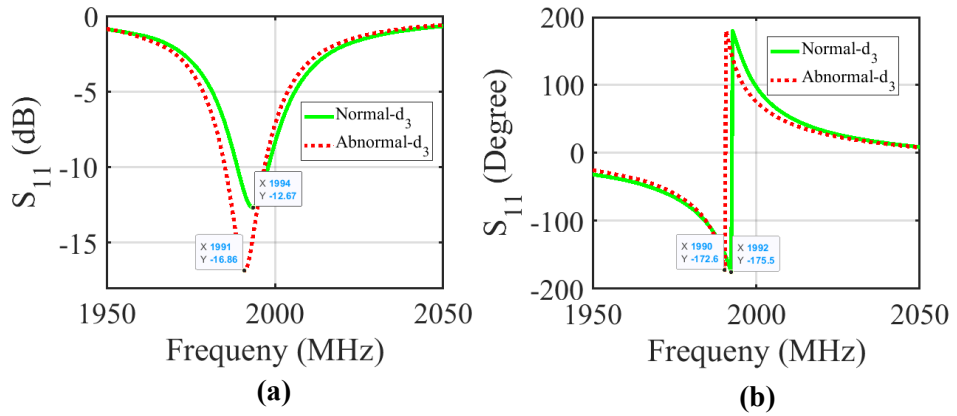


Figure 7.9: Numerical results of the 3D breast phantom with and without the presence of a tumor having a radius of 5 mm and a stand off distance of d1 = 15 mm. (a) The magnitude of $S_{11}$ (dB), and (b) the phase of $S_{11}$ (Degree).

For more validation of the proposed sensor array for improving the sensitivity area of object under test , the simulation was extended for detecting a breast tumor at three different locations inside the breast phantom. The breast tumor with diameter size 10 mm, is inserted at the three different

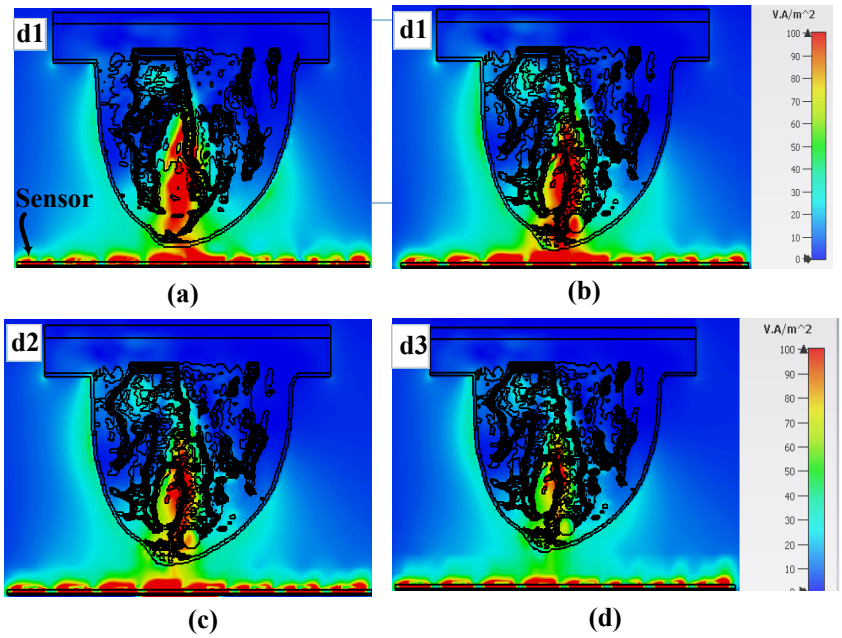


Figure 7.10: Simulation results of the power flow distribution: (a) Normal breast phantom model at a stand-off distance of 5 mm ,(b) Abnormal breast phantom model at a stand-off distance of 5 mm ,(c) Abnormal breast phantom model at a stand-off distance of 10 mm (d) Abnormal breast phantom model at a stand-off distance of 15 mm.

locations inside the breast phantom, namely L1, L2, and L3 as shown in Fig. 7.11. Fig. 7.12 show the magnitude and phase response of the sensor at three different tumor locations. In all the tumor locations, the sensor was capable of detecting the presence of tumor. Obviously from the results, inserting the tumor at locations closer to the sensor is easier to detect, where the shift in the frequency response of both magnitude and phase is noticeable compared with normal case.

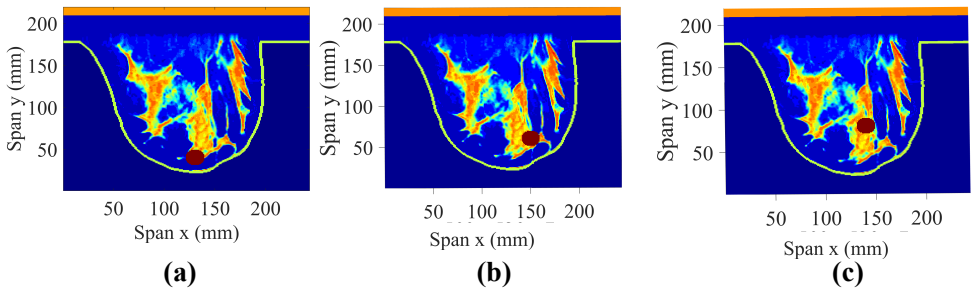


Figure 7.11: Simulation setup of three different tumor locations inside the breast phantom model.The tumor is located at random positions in the breast tissue with size of 10 mm. (a) Tumor located at L1 (x = 130 mm, y = 40 mm, z = 140 mm). (b) Tumor located at L2 (x = 150 mm, y = 60 mm, z = 140 mm). (c) Tumor located at L3 (x = 140 mm, y = 90 mm, z = 140 mm).

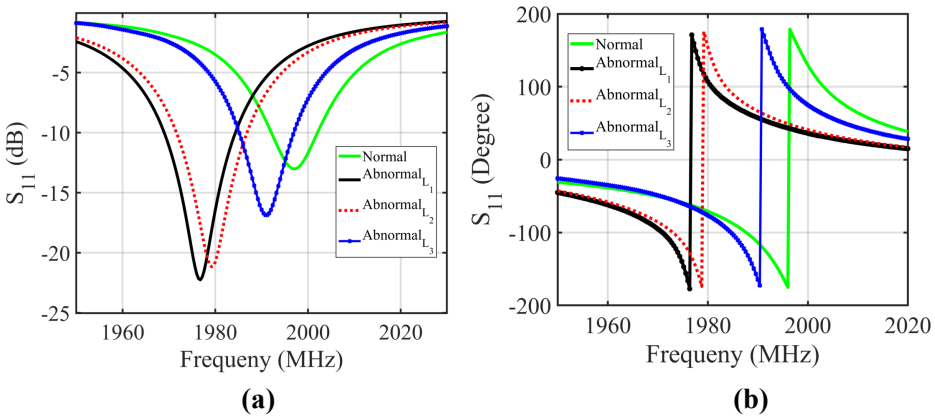


Figure 7.12: Simulation results of the sensor array, magnitude and phase response, for the breast phantom model with and without a 10 mm tumor at three different locations. (a) Magnitude of the sensor's reflection coefficient response ( $S_{11}$ in dB). (b) The phase of the sensor's reflection coefficient response ($S_{11}$ in degrees).

## 7.5 Experimental Verification for Breast Tumor Detection

An experiment was conducted to test the metasurface sensor in an environment that resembles female breast tissues. The fabricated sensor was used to validate the concept experimentally. The measurement setup used in the experiment consists of the metasurface, a vector Network Analyzer (VNA), and realistic normal and abnormal breast phantoms. The abnormal breast phantom contains a 10 mm diameter breast tumor. The experiment apparatus was contained in a wooden box with an opening in one of the box sides to allow for easily placing and changing the position of the breast phantom inside the box as shown in Fig. 7.13

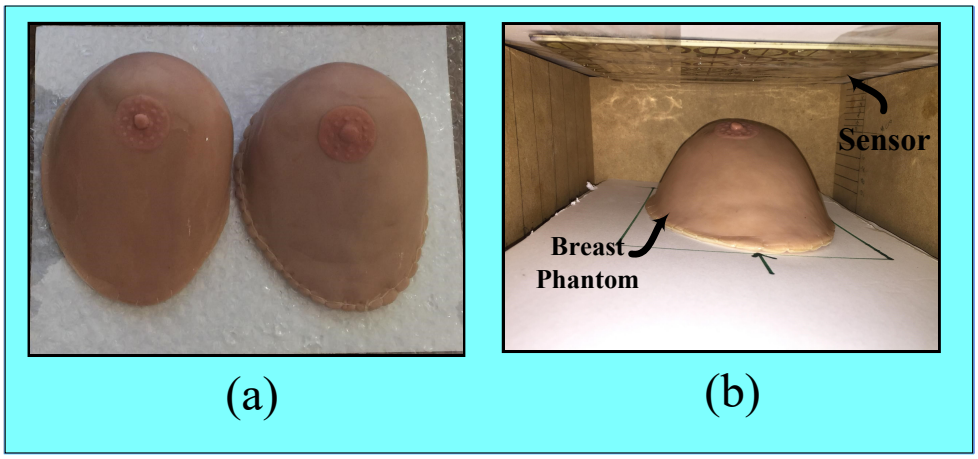


Figure 7.13: Measurement setup showing: (a) A photo showing the used both realistic normal and abnormal phantoms. (b) A photo showing the process of allocating the breast phantom at various locations within the wooden box with the fabricated metasurface sensor.

The breast phantoms which contains a layer of skin, fat tissues and meat were used as the base material resembling a female breast. The breast phantom was positioned at three standoff distance similar to the proposed once in the simulation namely d1, d2 and d3 as shown in Fig. 7.14(b). Then,

the response of the metasurface probe was recorded. Next, the same process was applied on the abnormal phantom at the same stand off distances d1, d2 and d3. For each stand off distance, the scattering parameters of the sensor with normal and abnormal phantom were recorded and analyzed as shown in Fig. 7.14, Fig. 7.15 and Fig. 7.16 respectively.

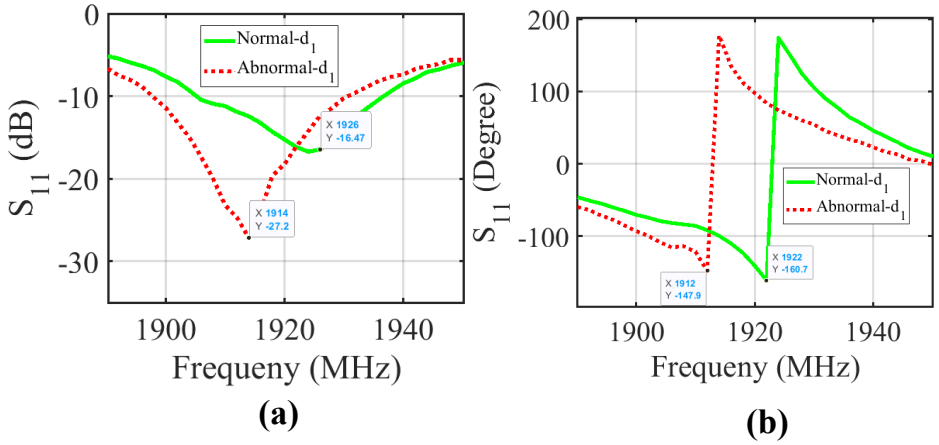


Figure 7.14: Experimental results of the sensor magnitude and phase response when breast phantoms at stand off distance is d1: 5 mm : a) the magnitude of the sensor response ( $S_{11}$ in dB), and (b) the phase of sensor response ($S_{11}$) in degrees.

## 7.6 Discussion

Near-field probes have traditionally been considered as electrically-small antennas whose radiation decays rapidly with distance from the probe. Such probes came into being, largely, by miniaturizing conventional antennas such as monopoles, dipoles, loops, patch antennas, and most recently, by employing a variety of different quasi-static resonators such as split-ring resonators, complementary split-ring resonators, or similar structures. What was missing from those near-field probes is a systematic design procedure that lends the designer to exert some type of control over the behavior of

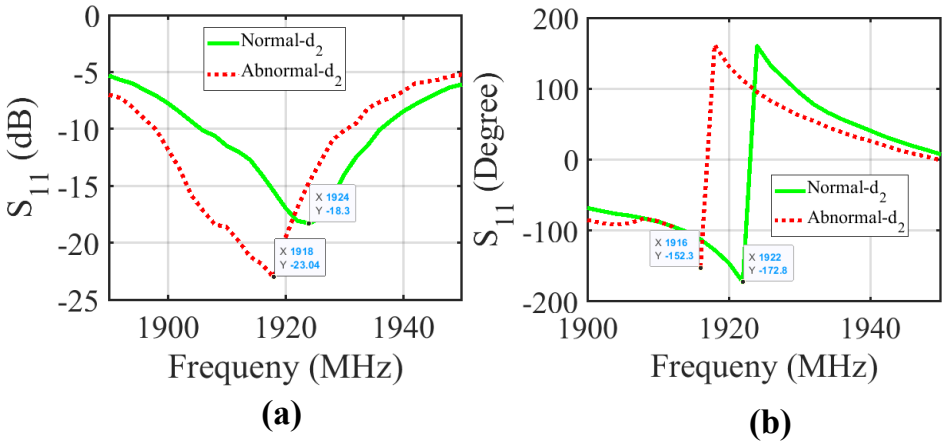


Figure 7.15: Experimental results of the sensor magnitude and phase response when breast phantoms at stand off distance is d2:10 mm : a) the magnitude of the sensor response ( $S_{11}$ in dB), and (b) the phase of sensor response ($S_{11}$) in degrees.

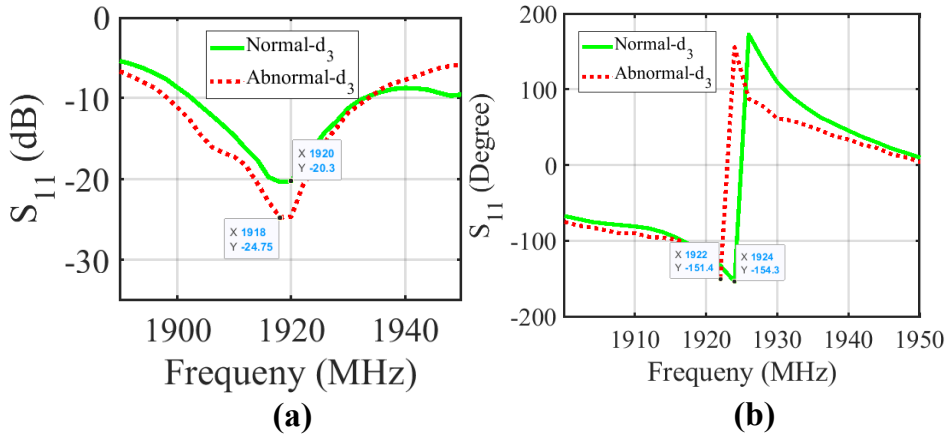


Figure 7.16: Experimental results of the sensor magnitude and phase response when breast phantoms at stand off distance is d3:15 mm : a) the magnitude of the sensor response ( $S_{11}$ in dB), and (b) the phase of sensor response ($S_{11}$) in degrees.

the sensor rather than ad-hoc structure minimization while adhering to specific or desired topological features such as sharp edges or pointed tips. The metasurface near-field probe/sensor/antenna introduced in this work aims

to produce a design procedure that provides sensing parameters not found in the earlier ad-hoc designs.

In earlier near-field probes, the entire probe or sensor was electrically small. In the metasurface sensor, the entire surface area of the sensor is not electrically small; however, each of the elements comprising the sensor is electrically small. The resulting array comprising these electrically-small sensors will then have two important characteristics: (a) all elements have equal radiation of EM energy, and (b) the overall response of the resonator is narrowband by virtue of the narrowband elements that comprise it (although not as narrowband as the single elements), and (c) the surface is composed of identical elements thus making each part of the surface practically equally sensitive to every other part (notice that the elements are fed using a corporate feed thus equal energy is provided to each element). Thus we expect the metasurface sensor to be not only sensitive to changes in material properties (of the surrounding medium) but also to the location where the material changes take place. Notice for instance the shift in the frequency when a tumor is present in the breast as compared to the case without a tumor can be attributed to the fact that when the breast is placed in the near field of the array sensor, the surface current distribution on the surface of the probe changes depending on the breast composition, as shown in Fig. 7.17. The change in the array's surface current results in a change in the input impedance, and consequently the reflection coefficient of the metasurface probe. Since the array is composed of 64 elements, the probe can experience a wide range of variation in its reflection coefficient that is related to surface current change in all the 64 elements. It is interesting to contrast the metasruface sensor behavior with, say, a microstrip patch antenna or a resonating dipole antenna which has appreciably non-uniform distribution thus makes it less sensitive to both changes in medium property and the location of the change.

To highlight the sensitivity of densely populated electrically small unit

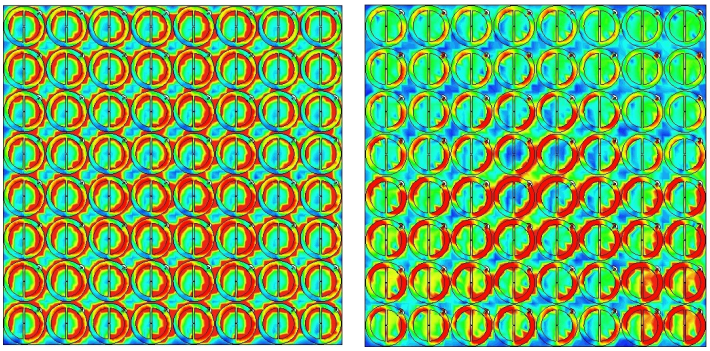


Figure 7.17: Surface current distribution on the surface of the array sensor. (a) Without a tumor, and (b) with a tumor. The blue color corresponding to 0 A/m and the red color corresponds to 1 A/m.

cells (metasurfaces) to that of patch antennas, the following numerical comparative simulation study was conducted. The study consisted of the metasurface proposed in this paper and a 4×4 array of square patch antennas where each patch has a side length of half a wavelength and the distance between adjacent antennas is also approximately half a wavelength as shown in Fig. 7.18 (a). Both the metasurface array and the patch antenna array were designed to operate at approximately 2 GHz to eliminate any dispersive effect when the sensors interact with the breast phantom as shown in Fig. 7.5 (d) and Fig. 7.18 (b), respectively.

Each sensor was scanned laterally at three positions to investigate the sensitivity area of each sensor. Please note here that we refer to the sensitivity area as the area over which the probe can detect any changes to its near field which is reflected on the reflection coefficient of the sensor by changes to its magnitude and phase as a function of frequency. Each sensor was placed at the same fixed vertical standoff distance of 5 mm to ensure that the breast is in the near field of the probe. Then the breast was centered at the left edge of each sensor array and the distribution of the

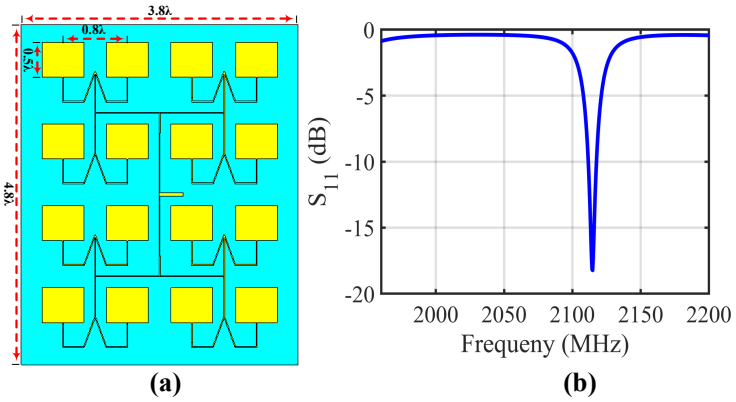


Figure 7.18: A schematic showing the proposed 4×4 microstrip patch antenna array where, (a) the layout of the 4×4 microstrip patch antenna array and, (b) a plot of the magnitude of the $S_{11}$ of the proposed microstrip patch antenna array in (dB).

power flow on a 2D cut plane was recorded using the color code as shown in Fig. 7.19. Identical simulations for both arrays were performed for different lateral positions where the breast is placed at the center of the arrays and finally when centered at the right edge of the arrays as shown in Fig. 7.19. From the power plots, we can see that the metasurface created a high power layer across the surface of the array due to the strong coupling along the unit cells which is clearly visible by the red color in Fig. 7.19 (d), (e),and (f). However, in the case of patch antenna array shown in Fig. 7.19 (a), (b),and (c), the power is concentrated at the center of the array due to weak coupling between the antennas and the nature of the radiation pattern of the patch antenna. Therefore, the sensitivity of the patch antenna array is much lower at the edges as compared to the center part of the array. In contrast, the metasurface has almost a uniform sensitivity across the array due to the strong coupling between the subwavelength unit cells which increases the sensitivity area as compared to that of the patch antenna array. This shows the ability of the metasurface to detect breast abnormalities without any mechanical movement given that the metasurface covers the whole breast content.

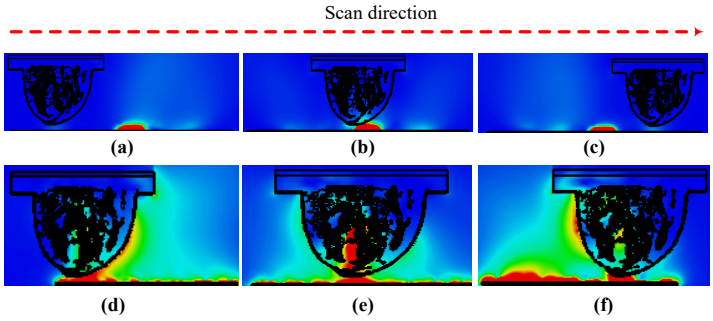


Figure 7.19: Comparative study of the power flow between 4×4 patch antenna array and the proposed metasurface sensor array at the three different lateral locations(left, center and right). The blue color corresponding to 0 watts/$m^2$ and the red color corresponds to 100 watts/$m^2$.

## 7.7 Conclusions

A near-field metasurface array sensor was introduced for detecting breast tumors. Numerical and experimental tests were used to validate the proposed detection methodology. This was achieved by testing the metasurface with a breast phantom having tumor placed at single location at three different stand off distances and with a breast phantom having tumors placed at different locations. Measurements were carried out on a realistic phantom that mimic a real female breast in terms of electric properties. The results showed high sensitivity of the metasurface which can indicate the existence of an anomaly that resembles a tumor inside a breast phantom having inhomogeneous material composition. When compared with an array of patch antennas, the metasurface array proposed in this work was able to create a larger sensitivity array which is a very critical feature for detecting tumors at different locations with various sizes. Such metasurface sensor can be viable for a number of applications where scanning is required to detect a certain object under test.

# Chapter 8

# Microwave Near-field system for Breast Tumor Detection

## 8.1 Introduction

This chapter, presents a detection technique that combines a machine learning technique with microwave near-field sensors for breast tumor detection. The detection technique consists of two main parts including metasurface microwave near-field sensors and machine learning classification logarithms. The metasurface is extend to the metasurface sensor which introduced in chapter 7. The sensor is a metasurface comprising an array of 8×8 electrically-small resonating elements, operates at 1.3 GHz.

Microwave breast tumor detection utilizing state of the art machine learning techniques provide a highly performance detection system that can differentiate between normal and abnormal breasts by employing the contrast in their dielectric properties. The proposed technique uses a highly sensitive microwave sensor to identify the differences between normal and abnormal breasts. Distinguishing between healthy and non-healthy breasts was based on estimating the differences in the reflection coefficient of the probe response for both normal and abnormal breasts. The machine learning meth-

ods proposed discriminate between normal and abnormal breast phantoms in different sizes and classes of breasts, and also significantly improve the accuracy, sensitivity and specificity of the proposed detection system.

## 8.2 Array Sensor Design Methodology

The single unit cell of the proposed metasurface sensor consists of two cascaded half loop with an embedded dipole which has two gaps in the middle, a dielectric substrate backed by a reflector and a port connecting the top and bottom layers through a via as shown in Fig. 8.1. The cell dimensions were chosen such that it operates at 1.48 GHz with L=20.5 mm, d1=3.5 mm, d2=2.5 mm g=0.8 mm, s=0.5 mm and copper thickness of t=35 $\mu m$. The unit cell was hosted on top of a Rogers RO3010 dielectric substrate having a $tan\delta$=0.0022 and a dielectric constant of $\epsilon_r$=10.2 with a thickness of a 1.27 mm. Each unit cell was fed by a port placed in shunt through a via with an impedance of 160 $\Omega$ as shown in Fig. 8.1. The unit cell was simulated using CST Microwave Studio [60].

The cell was first excited by a waveguide with Perfect Electric Conducting (PEC) walls along the X-axes and Perfect Magnetic Conducting (PMC) walls along the Y-axes to ensure a plane wave excitation. The top and bottom sides of the waveguide were assigned wave ports with a power level of 0.5 W as shown in Fig. 8.2. Simulation results for the reflection and absorption coefficients are shown in Fig. 8.3.

The near-field metasurface sensor consists of a periodic array of identical 8×8 cells and a dielectric substrate as described above. A single port located on the third layer was used to excite the metasurface array as shown in Fig. 8.4 (a) and (c). The third layer contains a cooperative feed that distribute the energy equally to all of the 64 unit cells. A ground plane is placed at the second layer which is shared between the resonators' layer

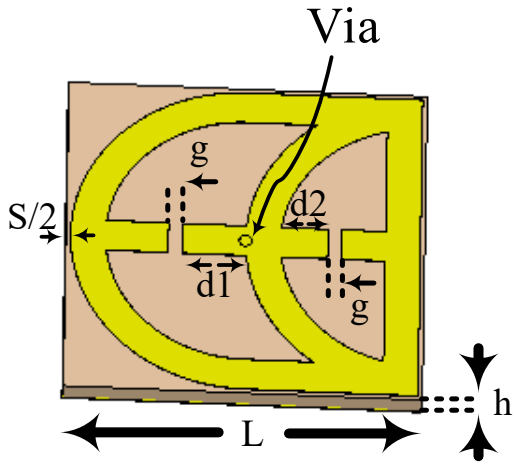


Figure 8.1: A schematic showing a single element of the proposed halfloop metasurface.

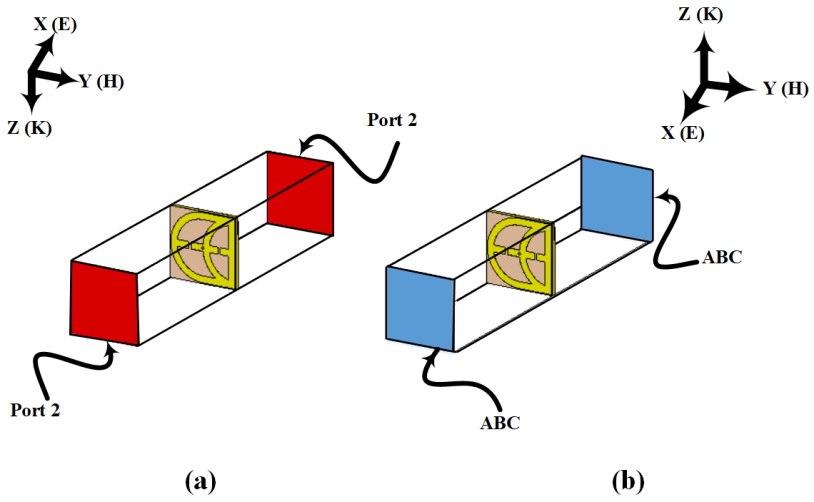


Figure 8.2: The simulation setup showing the proposed unit cell of the metasurface sensor placed inside a waveguide with periodic boundary condition. (a) transmitting mode, and (b) receiving mode.

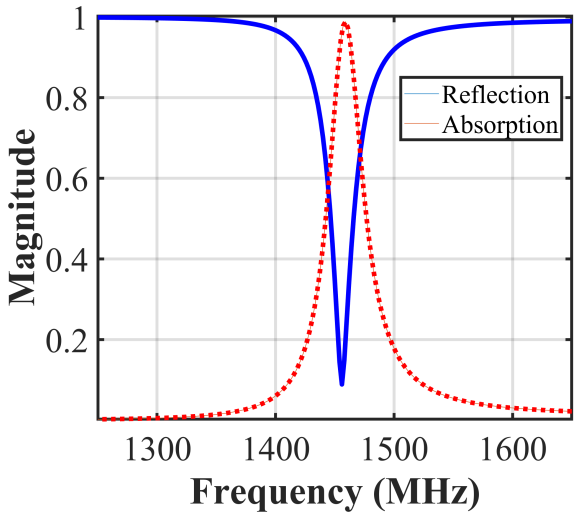


Figure 8.3: Simulation results for the reflection and absorption coefficients of the unit cell.

and the feeding network layer. A single stub matching circuit was used to ensure strong impedance matching between the 50 Ω coaxial feed line and the corporate feed network. The sensor array was fabricated according to the above design with a schematic as shown in Fig. 8.4 (b) and (d). The simulated and measured reflection coefficients of the sensor as shown in Fig. 8.5.

## 8.3 System Detection performance

The performance of any detection systems and screening tests relates to the system's ability to correctly discriminate between a normal and an abnormal patient. This system performance is based on statistical measures, such as accuracy, sensitivity, specificity, positive predictive value (PPV) and negative predictive value (NPV) [117, 118].

According to the reference standard, humans under test are assigned to one category cell of the four cells in a 2×2 table labeled TP through

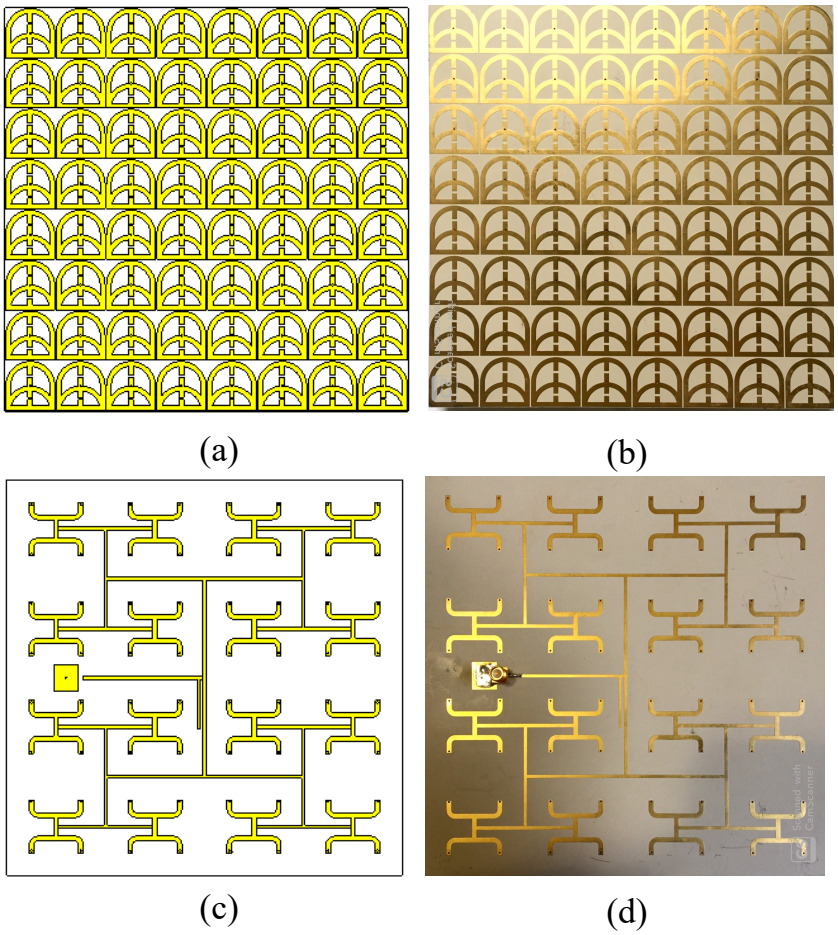


Figure 8.4: The photograph of the proposed halfloop metasurface array sensor: (a) Top view shows the metasurface array elements. (c) Bottom view shows the corporate feed network of the proposed sensor arrays. (b) Top view shows the array elements of the of the fabricated array sensor, and (d)Bottom view shows the corporate feed network of the of the fabricated array sensor.

TN as shown in Fig. 8.6. These four category cells are used to estimate the performances of the detection system and is defined as the follows [117,118]:

1. **True Positive (TP)**: the person has been correctly diagnosed to have the condition.

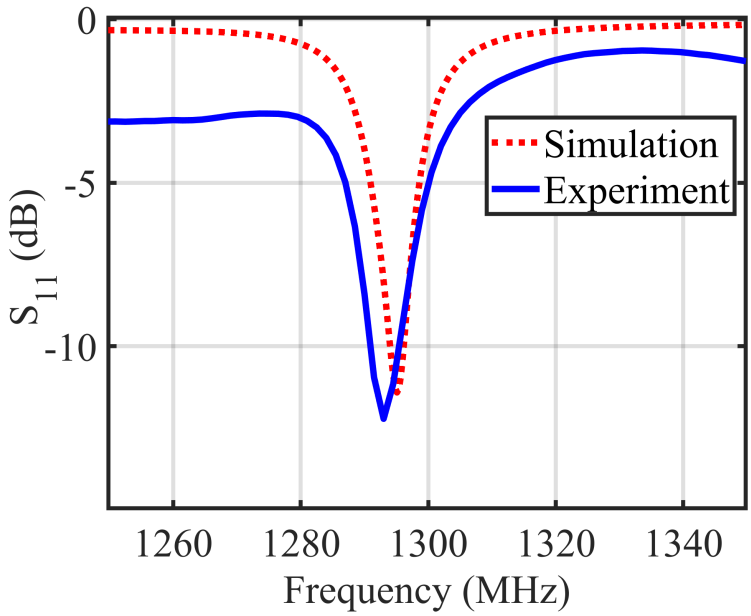


Figure 8.5: The reflection coefficient of the array sensor obtained through simulation and measurement.

2. **True Negative (TN)**: the person has been correctly diagnosed to not have the condition.

3. **False Positive (FP)**: the person has not been correctly diagnosed to have the condition.

4. **False Negative (FN)**: the person has not been correctly diagnosed to not have the condition.

From these four category cells,the five statistical measures performances of the detection system can be determined as the follows [117, 118]. Sensitivity or recall is defined as the proportion of sick people who are correctly identified as having breast tumor(s) (abnormal) and it can then be com-

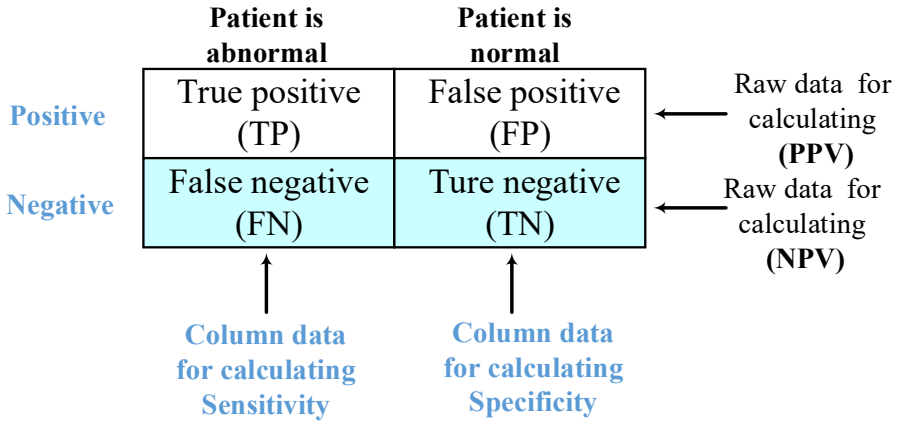


Figure 8.6: Diagram table showing the calculated statistical measures of the detection system which include the: sensitivity, specificity, and positive and negative predictive values.

puted using the following formula:

$$Sensitivity = [TP/(TP + FN)] * 100 \tag{8.1}$$

Specificity or selectivity is defined as the proportion of people who are correctly identified as not having breast tumor(s) (normal) and it can then be computed using the following formula:

$$Specificity = [TN/(TN + FP)] * 100 \tag{8.2}$$

Positive predictive value (PPV) or precision is defined as the proportion of people or samples under test with positive test result in total of samples with positive results and it can then be calculated using the following formula:

$$PPV = [TP/(TP + FP)] * 100 \tag{8.3}$$

Negative predictive value (NPV) is defined as the proportion of people or sample under test without the tumor with a negative test result in total of samples with negative test results and it can then be calculated using the following formula:

$$NPV = [TN/(TN + FN)] * 100 \tag{8.4}$$

PPV and NPV values are directly related to prevalence of the disease in the people and directly indicate the presence or absence of the disease according to the detection test.

F-measure or F1 Score is related with both the precision and recall by using the following equation: F-measure = 2×((Precision×Recall)/(Precision+Recall)) F-measure is used for a balance results between Precision and Recall. Accuracy is defined as the proportion of correctly diagnosed people among all the people who take the test and it can then be calculated using the following formula [117, 118]:

$$Accuracy = [(TP + TN)/(TP + TN + FP + FN)] * 100 \tag{8.5}$$

## 8.4 Machine Learning Approaches for Microwave Breast Tumor Detection

In recent years, machine learning has been applied to breast cancer detection. Many studies developed various modalities of machine learning for breast tumor detection by using different classifiers algorithms [119]– [129]. These classifiers' algorithms were used to transform qualitative scattering microwaves signals into more objective quantitative feature classification problems to characterize and detect breast tumor [130]– [133]. Machine

learning is employed to emphasize the difference in the probe responses of the two testings for both healthy and tumorous cases. Machine learning classification techniques are used for making a decision and a distinction between normal and abnormal breasts. The Machine learning classification techniques involve three steps for analyzing and making a decision of the recording data as shown in Fig. 8.7:

1. **Data preprocessing** is an important step in the machine learning technique. It is used to convert the collected data from the microwave sensor into a clear data set before feeding it into the classification model.

2. **Feature extraction methods** are used to extract the most important or most relevant features from each recorded backscattered microwave signal that will use in the classification model. Several feature extraction algorithms have been examined in the literature for MI breast cancer detection, such as Principal Component Analysis (PCA), Local Discriminant Basis (LDB), and Independent Component Analysis (ICA). [134]– [144].

3. **Classification algorithms** used the relevant features from the extraction data for distinguishing between the normal and abnormal breasts. These algorithms used to decide whether or not a tumor is present by using the signatures features of the tumors. Several classification approaches have been applied to detect the presence of breast tumors including Support Vector Machine (SVM), Cost-sensitive Support vector machines (CSSVM), Quadratic Discriminant Analysis (QDA), PCA, linear discriminant analysis (LDA), and, Decision Tree (DT). [145]– [155].

In this study, the PCA feature extraction method is used to reduce the dimensionality of the problem by implementing a vector space transform [96]

as explained in chapter one. The main challenge of all these previous techniques is to find a suitable combination of features and classifiers for discriminating between healthy and nonhealthy breasts by using the signature of the contrast in their dielectric properties. In this study, SVM and DT classification logarithms are used for discriminating between normal and nonnormal breasts because both of them, SVM and TD, are powerful methods for binary classification problems that used for a distinction between two classes database, such as normal and abnormal breasts

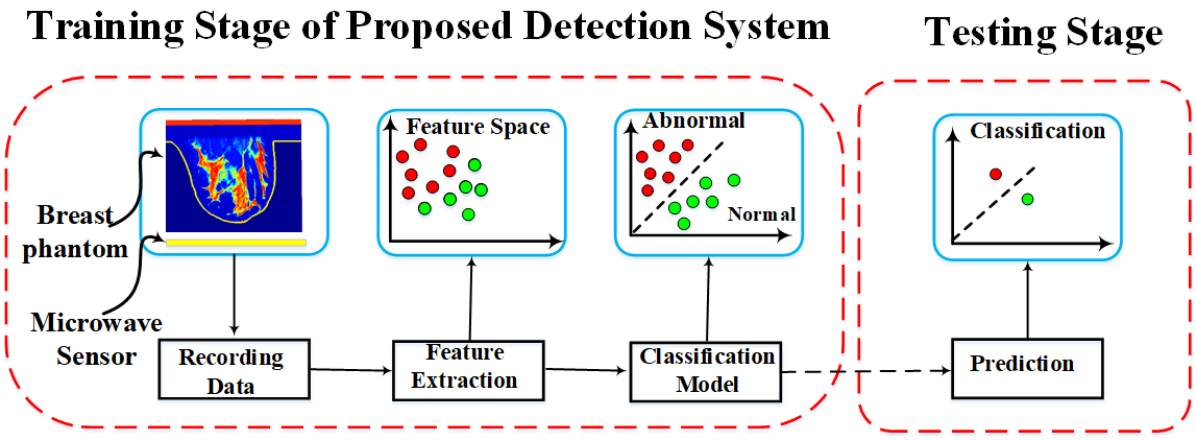


Figure 8.7: Flow chart diagram shows the methodology process for breast tumors detection using machine learning techniques.

The SVM is a supervised and discriminative machine learning algorithm that is used as a classifier algorithm for data classification. The SVM is typically used for separating data which has exactly two classes such as normal and abnormal breasts. [156–158]. The optimum function of SVM as a classifier algorithm is to classify or separate between two classes recorded data by discovering the best hyperplane. The hyperplane separates all recorded data points of first-class from those points data of the second class. The optimum hyperplane of the SVM classifier is the largest margin between the two classes (normal and abnormal breasts). The SVM classifier finds

the best margin based on support vectors that are closest points to the separating hyperplane. Two types of SVM classifier are used include: linear and nonlinear classification [158, 159]. Nonlinear Kernel SVM classification algorithm maps the data to a higher-dimension feature space. Radial Basis Function (RBF) is one type of the Kernel, which is used for this classification study. [156–160].

The equation of generated the decision hyperplane in the features space is defined as the following below [156–160]:

$$wx + b = 0 \tag{8.6}$$

Where : $\boldsymbol{x}$ represents the collected data, $\boldsymbol{w}$ is the normal vector to the hyperplane or weights, and b is the bias. The RBF function is obtained by using the following equation:

$$K(X_i, X_j) = \exp(-\gamma||X_i - X_j||^2) \tag{8.7}$$

Where -$\gamma$ is the scaling factor of the RBF Kernel.

DT is one of the most powerful machine learning algorithms used for binary classification problems. The DT is a structure like a tree, where each node denotes an attribute ( feature), each branch represents an outcome decision of the examination, and each leaf represents a class label [55,161–163]. The machine learning algorithm model performance for predicting unseen data is evaluated by using the cross-validation. In the cross-validation procedures, the collected dataset is randomly divided and sorted into k folds.

In this study, SVM and TD methods proposed as discriminated algorithms for discriminating between normal and abnormal breast phantoms in different sizes and classes of breasts. Also, they are used to calculate the sensitivity, specificity, accuracy, and precision for separating between the two the classes normal and abnormal breast phantoms.

## 8.5 Classification Test Between Normal and Abnormal Breast Phantoms

In this section, a database of ninety different sizes and classes realistic breasts phantoms (45 normal breasts and 45 abnormal breasts) were created using CST. Forty-five different sizes of normal breasts comprising the four different classes (every ten normal breasts were created using dielectric properties of each class) named: mostly fat, scattered fibroglandular, heterogeneously dense, very dense as shown in chapter two. Forty-five abnormal breasts were created using CST. a database of different sizes of tumors embedded in the abnormal breasts. The different sizes tumors have radius vary between the following values: 11, 9, 8, 7, 6, 5, 4, 3.5,3 and 2.5 mm.

The proposed technique presented here for breast tumor detection employs two testings for both normal and abnormal breasts using two identical near field sensors placed at the same distance off away from both of them normal and abnormal breasts. Recording and analyzing the responses of the two sensors using machine learning is used for distinguishing between the normal and abnormal breast. Machine learning is employed to emphasize the difference in the sensor responses of the two testing for both healthy and tumorous cases. We investigate the detection of breast tumors if a woman has different breast sizes while having an abnormality in one of them. We show that when two different-size phantom breasts, one with a tumor and one without, the sensor is able to detect the presence of the tumor with high probability. Simulation results of ninety different sizes realistic breasts phantoms (45 normal or healthy breasts and 45 abnormal or unhealthy breasts) show that the proposed probe combined with machine learning is capable of differentiating between normal and abnormal breasts.

Two scenarios are tested; firstly, the proposed sensor was simulated with each size of the developed forty-five different-size normal breast phantoms at

a standoff distance of 5 mm. The reflection coefficient response is recorded of each size of these normal breast phantoms. Next, the sensor was simulated with the other developed forty-five different-size abnormal breast phantoms with the same standoff distance of 5 mm. In each abnormal realistic breast phantom size test, the reflection coefficient response is recorded. In the second test scenario, the forty-five different sizes of abnormal breasts were simulated with the proposed sensor using the same standoff distance of 5 mm.

Then, for the recorded probe responses of ninety normal and abnormal breast phantoms, PCA feature extraction methods, knowledge-based approach and two classifiers (SVM and TD) were investigated. These two classifiers (SVM and TD) are used to emphasize the differences in the probe responses between normal and abnormal breast models.

The sensitivity of the sensor is based on the value of the main $\Delta$ decision given in equation 8.8. If the value of $\Delta$ Decision is high, this indicates a high difference in the sensor response of both normal breast and abnormal breast with the inserted tumor

$$\Delta Decision = S_{11}Right - S_{11}left \tag{8.8}$$

$\Delta$ decision is based on results of other four sub $\Delta$ decision namely: $\Delta$ min frequency of both magnitude of $S_{11}$ and phase of $S_{11}$, $\Delta$ magnitude of $S_{11}$, and $\Delta$ decision phase of $S_{11}$.

The prediction or classification setup makes a decision based on the value of the main $\Delta$ decision which makes a decision based on the other sub $\Delta$s decision. In the next step, features are extracted using a knowledge-based $\Delta$s decision approach by using minimum frequency (resonance frequency) and the minimum response of $S_{11}$. Fig. 8.9 shows the results of both normal and abnormal breasts by using $\Delta$s decision of the $\Delta$ magnitude of $S_{11}$. Next, SVM and DT classification models are using by training and testing using

10-fold cross-validation of the knowledge-based features ($\Delta$s decision) to estimate the performance metrics. The performance metrics result of the both SVM and DT classifiers using both $\Delta$ magnitude of $S_{11}$ and $\Delta$ phase of $S_{11}$ is presented in Table 8.1 and Table 8.2. The results show that the $\Delta$ decision is higher when using the magnitude of $S_{11}$ as compared with $\Delta$ decision of the phase of $S_{11}$.

Table 8.1: Results of comparison of SVM and TD classification algorithms of using $\Delta$ magnitude of $S_{11}$ show the the performance metrics values of Accuracy, Precision, Sensitivity, Specificity, and F_Measure.

| **Metric/Classifier** | **SVM** | **Decision Tree** |
|---|---|---|
| **Accuracy** | 95.6 | 94.4 |
| **Precision** | 93.8 | 95.8 |
| **Sensitivity** | 97.8 | 97.8 |
| **Specificity** | 93.2 | 95.5 |
| **F_Measure** | 95.8 | 96.8 |

Table 8.2: Results of comparison of SVM and TD classification algorithms of using $\Delta$ phase of $S_{11}$ show the the performance metrics values of Accuracy, Precision, Sensitivity, Specificity, and F_Measure.

| **Metric/Classifier** | **SVM** | **Decision Tree** |
|---|---|---|
| **Accuracy** | 79.7 | 93.3 |
| **Precision** | 66.7 | 93.5 |
| **Sensitivity** | 99 | 97.8 |
| **Specificity** | 79.7 | 93.5 |
| **F_Measure** | 47.7 | 93.2 |

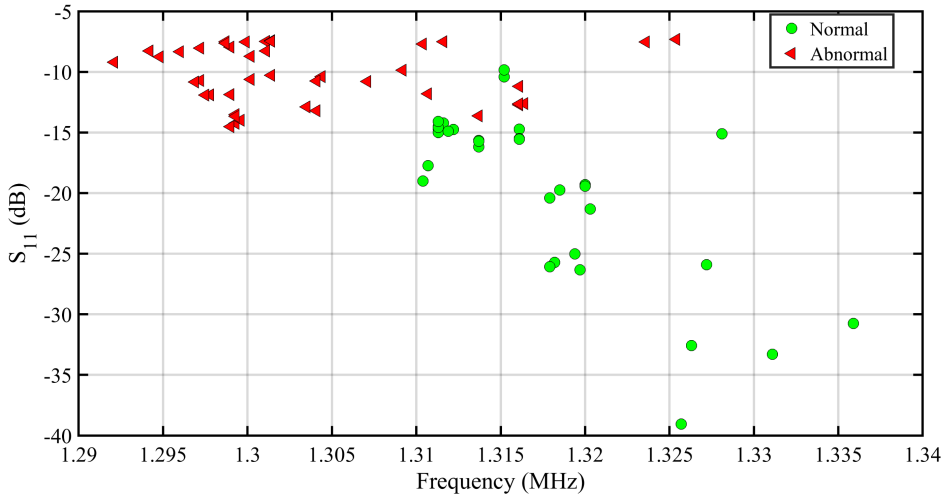


Figure 8.8: Results of classification between normal and abnormal breast phantoms using using knowledge based approach.

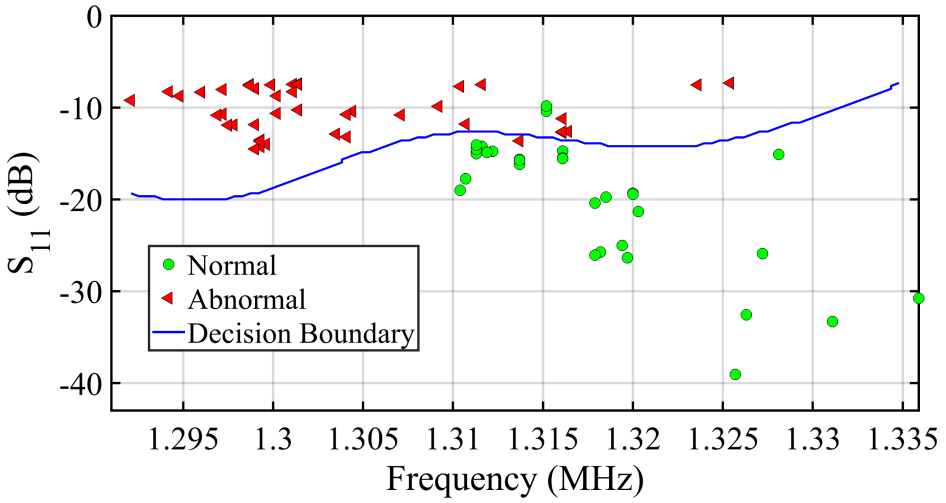


Figure 8.9: Results of classification between normal and abnormal breast phantoms using using SVM.

## 8.6 Conclusion

In this chapter, we presented a near-field metasurface sensor with machine learning for microwave breast tumor detection. The sensor is metasurface was excited by a single port. The sensor was simulated with different sizes of normal and abnormal numerical realistic phantoms to see its capability for distinguishing between different sizes of normal and abnormal breast phantoms model. Analyzing the recorded data of the proposed sensor response using two classification models SVM and TD by training and testing improve the distinctions between different sizes of both cases normal and abnormal breast phantoms with an accuracy of 95.6% and 94.4% respectively using $\Delta$ of $S_{11}$ magnitude.

# Chapter 9

# Accomplished and Future Work

## 9.1 Accomplished Work

The following list include a summary of the work accomplished in this thesis:

1. A detailed analysis of a novel methodology for using the anonymous breast MRI datasets which were obtained from the University of Wisconsin online repository for construction of 3D realistic numerical breast phantoms in CST Microwave Studio was presented in this dissertation (**Chapter 2**).

2. A literature review study of the dielectric properties of normal and tumorous breast tissues in the microwave regime was presented in the (**Chapter 2**).

3. Introduced a concept of using Ultra-narrow band electrically *small single electric dipole* probe with the classification method (PCA) technique for breast tumors detection was presented and then verified numerically and experimentally (**Chapter 3**).

4. Introduced a concept of using an electrically *small single loop probe* which considered as a magnetic-dipole probe with classification PCA

technique for breast tumors detection was presented and verified numerically and experimentally (**Chapter 4**).

5. A method for enhancing the sensitivity area of the detection systems was proposed using *4-element identical printed dipole* antenna array fed with a single port (**Chapter 5**).

6. A method for improving the sensitivity area of the detection systems was proposed using *4-element identical loop* antenna array fed with a single port (**Chapter 6**).

7. A near-field *metasurface* sensor comprising an array of *8×8 electrically-small resonating elements* for detecting early stage breast tumors was presented (**Chapter 7**).

8. introduced a concept of using machine learning technique for numerically estimating the sensitivity, specificity and accuracy of the developed system for discriminating between different sizes and classes normal and abnormal breast phantoms (**Chapter 8**).

## 9.2 List of Publications


[1] M. A. Aldhaeebi,T. S. Almoneef, A. Ali, Z. Ren and O. M. Ramahi, "Near Field Breast Tumor Detection Using Ultra-Narrow Band Probe with Machine Learning Techniques," *Scientific Report*, vol. 8, pp.12607, 2018 **(Accepted)**.

[2] M. A. Aldhaeebi,T. S. Almoneef and O. M. Ramahi, "Near-field Sensors with Machine Learning for Breast Tumor Detection," *Journal of Computational Vision and Imaging Systems*, vol. 4, pp.3–3, 2018**(Accepted)**.

[3] M. A. Aldhaeebi,T. S. Almoneef,H. Attia and O. M. Ramahi, "Electrically Small Magnetic Probe with PCA for Near-Field Microwave Breast Tumors Detection," *Progress In Electromagnetics Research*,vol. 84, pp. 177–186, 2019 **(Accepted)**.

[4] M. A. Aldhaeebi,T. S. Almoneef,H. Attia and O. M. Ramahi, "Near-field Microwave Loop Array Sensor for Breast Tumor Detection," *IEEE Sensors Journal*,vol. 19, pp. 11867–11872, 2019 **(Accepted)**.

[5] M. A. Aldhaeebi,S. Bamatraf and O. M. Ramahi, "Challenges with Machine Learning for Microwave Breast Tumor detection," *Journal of Computational Vision and Imaging Systems*, vol. 4, pp.1–1, 2019**(Accepted)**.

[6] M. A. Aldhaeebi,T. S. Almoneef, S. Bamatraf and O. M. Ramahi, "Near-Field Metasurface Sensor for Detecting Early Stage Breast Tumors," *IEEE Sensors Journal*, 2019 **(Submitted)**.

[7] M. A. Aldhaeebi, K. Alzoubi,T. S. Almoneef, S. Bamatraf,H. Attia and O. M. Ramahi, "Review of Microwaves Techniques for Breast Cancer Detection," *IEEE Access*, 2019 **(Submitted)**.

[8] M. A. Aldhaeebi,T. S. Almoneef and O. M. Ramahi, "Near-field Microwave Breast Cancer Detection using Electrically Small Sensors and Machine Intelligence," in *2018 IEEE Indian Conference on Antennas and Propogation (InCAP)*. IEEE, 2018, pp. 1-2**(Conference)**.

[9] M. A. Aldhaeebi, T. S. Almoneef and O. M. Ramahi, "Probes with Machine Learning for Breast Tumor Detection," in *2018 Advances in Breast Cancer Research:Towards Precision Therapy*. ABCR, 2018, pp. 1-2**(Conference)**.

[10] M. A. Aldhaeebi, T. S. Almoneef and O. M. Ramahi, "Near-Field Probes with Machine Learning for Breast Tumor Detection," in *4 th Annual RVH IGNITE Research Conference and Workshops*. RVH IGNITE Research, 2018, pp. 1-2**(Conference)**.

[11] M. A. Aldhaeebi, S. Bamatraf, T. S. Almoneef and O. M. Ramahi, "Near-field Electrically Small Sensors Array with PCA for Microwave Breast Tumor Detection," in *2019 IEEE International Symposium on Antennas and Propagation and USNC-URSI Radio Science Meeting*. IEEE, 2019, pp. 1007-1008 **(Conference)**.

[12] M. A. Aldhaeebi, S. Bamatraf, and O. M. Ramahi, "Breast Tumor Diagnosis using Machine Learning with Microwave Probes," in *2019 IEEE ICOICE*. IEEE, 2019 **(Conference)**.

[13] O. M. Ramahi, M. A. Aldhaeebi and T. S. Almoneef. Breast cancer detection using near-field probes with machine learning techniques. *US Non-Provisional Patent Application No. 16283204* **(Patent)**.

## 9.3 Future Work

1. **Analyze and compare** different ways to improve the sensitivity of microwave sensors
2. **Extend** the array sensor method introduced in (**Chapter 5 & 6**) by combining loop and dipole arrays that could further improve the microwave detection system. In (**Chapter 5**) only 4-element identical electrically small dipole antenna array excited by a single port is studied as a microwave sensor. In (**Chapter 6**) only 4-element identical electrically small loop antenna array excited by a single port is studied as a microwave sensor however the combination between two loop and dipole sensors excited by a single port can be used to further improve the sensitivity area of the microwave sensor.
3. **Extend** the metasurface sensor presented in (**Chapter 7**) by adding one additional diploe in the middle of the loop to have two cross dipoles to form cross-polarized arrays which will further enhance the sensitivity of the microwave detection system
4. **Extend** the proposed methods of using one metasurface sensor presented in (**Chapter 7 & 8**) for breast tumor detection by using five metasurface sensors which cover the whole breast and therefore eliminating the use of mechanical motors to move the sensor all over the breast.
5. **Extend** the developed machine learning logarithms presented in (**Chapter 8**) to filter irrelevant features of the breast.

6. **Develop** a portable detection system. Integration of the standalone VNA and the sensor into one miniaturized unit. The VNA circuitry will be positioned at the back of the sensor and will be connected with a laptop. The machine learning and other algorithms will be embedded within the VNA software in a laptop. Finally, the detection decision will be transmitted to the laptop.

7. **Performing** clinical trial test in Grand River Hospital to experimentally validate our device.

# References


[1] American Cancer Society. Cancer facts and figures 2019 @ONLINE, 2019.

[2] Lulu Wang. Early diagnosis of breast cancer. *sensors*, 17(7):1572, 2017.

[3] Wendie A Berg, Lorena Gutierrez, Moriel S NessAiver, W Bradford Carter, Mythreyi Bhargavan, Rebecca S Lewis, and Olga B Ioffe. Diagnostic accuracy of mammography, clinical examination, us, and mr imaging in preoperative assessment of breast cancer. *Radiology*, 233(3):830–849, 2004.

[4] Independent UK Panel on Breast Cancer Screening et al. The benefits and harms of breast cancer screening: an independent review. *The Lancet*, 380(9855):1778–1786, 2012.

[5] Amy Berrington de Gonzalez and Sarah Darby. Risk of cancer from diagnostic x-rays: estimates for the uk and 14 other countries. *The lancet*, 363(9406):345–351, 2004.

[6] Cécile M Ronckers, Christine A Erdmann, and Charles E Land. Radiation and breast cancer: a review of current evidence. *Breast Cancer Research*, 7(1):21, 2004.

[7] Debmalya Barh. *Omics Approaches in Breast Cancer: Towards Next-Generation Diagnosis, Prognosis and Therapy*. Springer, 2014.

[8] Angela Moore. The practice of breast ultrasound: Techniques, findings, differential diagnosis. *Ultrasound in Medicine and Biology*, 36(2):358, 2010.

[9] Rupali Sood, Anne F Rositch, Delaram Shakoor, Emily Ambinder, Kara-Lee Pool, Erica Pollack, Daniel J Mollura, Lisa A Mullen, and Susan C Harvey. Ultrasound for breast cancer detection globally: A systematic review and meta-analysis. *Journal of global oncology*, 5:1–17, 2019.

[10] Sollip Kwon and Seungjun Lee. Recent advances in microwave imaging for breast cancer detection. *International journal of biomedical imaging*, 2016, 2016.

[11] Susan G Orel and Mitchell D Schnall. Mr imaging of the breast for the detection, diagnosis, and staging of breast cancer. *Radiology*, 220(1):13–30, 2001.

[12] Elise C Fear, Susan C Hagness, Paul M Meaney, Michal Okoniewski, and Maria A Stuchly. Enhancing breast tumor detection with near-field imaging. *IEEE Microwave magazine*, 3(1):48–56, 2002.

[13] Lawrence E Larsen and John H Jacobi. Medical applications of microwave imaging. Technical report, INSTITUTE OF ELECTRICAL AND ELECTRONICS ENGINEERS INC NEW YORK, 1985.

[14] Raquel Cruz Conceição, Johan Jacob Mohr, and Martin O'Halloran. *An introduction to microwave imaging for breast cancer detection*. Springer, 2016.

[15] Ahmed M Hassan and Magda El-Shenawee. Review of electromagnetic techniques for breast cancer detection. *IEEE Reviews in Biomedical Engineering*, 4:103–118, 2011.

[16] S Mouty, B Bocquet, R Ringot, N Rocourt, and P Devos. Microwave radiometric imaging (mwi) for the characterisation of breast tumours. *The European Physical Journal Applied Physics*, 10(1):73–78, 2000.

[17] Xiong Wang, Hao Xin, Daniel Bauer, and Russell Witte. Microwave induced thermal acoustic imaging modeling for potential breast cancer detection. In *Antennas and Propagation (APSURSI), 2011 IEEE International Symposium on*, pages 722–725. IEEE, 2011.

[18] Jian Song, Zhiqin Zhao, Jiangniu Wu, Xiaozhang Zhu, Zaiping Nie, and Qing-Huo Liu. Thermo-acoustic imaging for different breast tissues in microwave induced thermo-acoustic tomography system. In *Antennas and Propagation Society International Symposium (APSURSI), 2013 IEEE*, pages 2032–2033. IEEE, 2013.

[19] Chritian Pichot, Luis Jofre, Guillaume Peronnet, and Jean Bolomey. Active microwave imaging of inhomogeneous bodies. *IEEE transactions on antennas and propagation*, 33(4):416–425, 1985.

[20] WC Chew. Imaging and inverse problems in electromagnetics. *Advances in Computational Electrodynamics: The Finite-Difference Time-Domain Method*, pages 653–702, 1998.

[21] Paul M Meaney, Margaret W Fanning, Dun Li, Steven P Poplack, and Keith D Paulsen. A clinical prototype for active microwave imaging of the breast. *IEEE Transactions on Microwave Theory and Techniques*, 48(11):1841–1853, 2000.

[22] Steven P Poplack, Tor D Tosteson, Wendy A Wells, Brian W Pogue, Paul M Meaney, Alexander Hartov, Christine A Kogel, Sandra K Soho, Jennifer J Gibson, and Keith D Paulsen. Electromagnetic breast imaging: results of a pilot study in women with abnormal mammograms. *Radiology*, 243(2):350–359, 2007.

[23] Paul M Meaney, Margaret W Fanning, Timothy Raynolds, Colleen J Fox, Qianqian Fang, Christine A Kogel, Steven P Poplack, and Keith D Paulsen. Initial clinical experience with microwave breast imaging in women with normal mammography. *Academic radiology*, 14(2):207–218, 2007.

[24] Steven P Poplack, Keith D Paulsen, Alexander Hartov, Paul M Meaney, Brian W Pogue, Tor D Tosteson, Margaret R Grove, Sandra K Soho, and Wendy A Wells. Electromagnetic breast imaging: average tissue property values in women with negative clinical findings. *Radiology*, 231(2):571–580, 2004.

[25] Paul M Meaney, Keith D Paulsen, and Margaret W Fanning. Microwave imaging for breast cancer detection: preliminary experience. pages 308–319, 2000.

[26] Paul M Meaney, Margaret W Fanning, Roberta M di Florio-Alexander, Peter A Kaufman, Shireen D Geimer, Tian Zhou, and Keith D Paulsen. Microwave tomography in the context of complex breast cancer imaging. pages 3398–3401, 2010.

[27] Natalia K Nikolova. Microwave imaging for breast cancer. *IEEE microwave magazine*, 12(7):78–94, 2011.

[28] Dun Li, Paul M Meaney, Timothy Raynolds, Sarah A Pendergrass, Margaret W Fanning, and Keith D Paulsen. Parallel-detection microwave spectroscopy system for breast imaging. *Review of Scientific Instruments*, 75(7):2305–2313, 2004.

[29] Elise C Fear, Paul M Meaney, and Maria A Stuchly. Microwaves for breast cancer detection. *IEEE potentials*, 22(1):12–18, 2003.

[30] Paul M Meaney, Keith D Paulsen, Alexander Hartov, and Robert K Crane. An active microwave imaging system for reconstruction of 2-d

electrical property distributions. *IEEE Transactions on Biomedical Engineering*, 42(10):1017–1026, 1995.

[31] Elise Fear, Andrew Low, Jeff Sill, and Maria A Stuchly. Microwave system for breast tumor detection: Experimental concept evaluation. In *Antennas and Propagation Society International Symposium, 2002. IEEE*, volume 1, pages 819–822. IEEE, 2002.

[32] Shakti K Davis, Xu Li, Essex J Bond, Susan C Hagness, and Barry D Van Veen. Frequency-domain penalized least-squares beamformer design for early detection of breast cancer via microwave imaging. In *Sensor Array and Multichannel Signal Processing Workshop Proceedings, 2002*, pages 120–124. IEEE, 2002.

[33] Dun Li, Paul M Meaney, and Keith D Paulsen. Conformal microwave imaging for breast cancer detection. *IEEE Transactions on Microwave Theory and Techniques*, 51(4):1179–1186, 2003.

[34] Alexander E Bulyshev, Serguei Y Semenov, Alexander E Souvorov, Robert H Svenson, Alexei G Nazarov, Yuri E Sizov, and George P Tatsis. Computational modeling of three-dimensional microwave tomography of breast cancer. *IEEE Transactions on Biomedical Engineering*, 48(9):1053–1056, 2001.

[35] Ki-Chul Kwon, Young-Tae Lim, Chul-Ho Kim, Nam Kim, Chan Park, Kwan-Hee Yoo, Seong-Ho Son, and Soon-Ik Jeon. Microwave tomography analysis system for breast tumor detection. *Journal of medical systems*, 36(3):1757–1767, 2012.

[36] Serguei Semenov. Microwave tomography: review of the progress towards clinical applications. *Philosophical Transactions of the Royal Society of London A: Mathematical, Physical and Engineering Sciences*, 367(1900):3021–3042, 2009.

[37] Alexander E Bulyshev, Serguei Y Semenov, Alexander E Souvorov, Robert H Svenson, Alexei G Nazarov, Yuri E Sizov, and George P Tatsis. Computational modeling of three-dimensional microwave tomography of breast cancer. *IEEE Transactions on Biomedical Engineering*, 48(9):1053–1056, 2001.

[38] Paul M Meaney, Margaret W Fanning, Dun Li, Steven P Poplack, and Keith D Paulsen. A clinical prototype for active microwave imaging of the breast. *IEEE Transactions on Microwave Theory and Techniques*, 48(11):1841–1853, 2000.

[39] Seong-Ho Son, Nikolai Simonov, Hyuk-Je Kim, Jong-Moon Lee, and Soon-Ik Jeon. Preclinical prototype development of a microwave tomography system for breast cancer detection. *ETRI journal*, 32(6):901–910, 2010.

[40] Soon-Ik Jeon, Bo-Ra Kim, and Seong-Ho Son. Clinical trial of microwave tomography imaging. In *URSI Asia-Pacific Radio Science Conference (URSI AP-RASC)*, pages 1–2. IEEE, 2016.

[41] Jack E Bridges. Non-invasive system for breast cancer detection, January 6 1998. US Patent 5,704,355.

[42] Xu Li and Susan C Hagness. A confocal microwave imaging algorithm for breast cancer detection. *IEEE Microwave and wireless components letters*, 11(3):130–132, 2001.

[43] Emily Porter. Microwave breast tumor detection: simulation and design of experiments with tissue phantoms. In *Masters Abstracts International*, volume 49, 2010.

[44] Lulu Wang. Microwave sensors for breast cancer detection. *Sensors*, 18(2):655, 2018.

[45] Maciej Klemm, Ian Craddock, Jack Leendertz, Alan Preece, and Ralph Benjamin. Experimental and clinical results of breast cancer detection using uwb microwave radar. In *Antennas and Propagation Society International Symposium, 2008. AP-S 2008. IEEE*, pages 1–4. IEEE, 2008.

[46] Vitaliy Zhurbenko, Tonny Rubæk, Viktor Krozer, and Peter Meincke. Design and realisation of a microwave three-dimensional imaging system with application to breast-cancer detection. *IET microwaves, antennas & propagation*, 4(12):2200–2211, 2010.

[47] Elise C Fear, J Bourqui, C Curtis, D Mew, B Docktor, and C Romano. Microwave breast imaging with a monostatic radar-based system: A study of application to patients. *IEEE transactions on microwave theory and techniques*, 61(5):2119–2128, 2013.

[48] Benjamin R Lavoie, Michal Okoniewski, and Elise C Fear. Estimating the effective permittivity for reconstructing accurate microwave-radar images. *PloS one*, 11(9):e0160849, 2016.

[49] Emily Porter, Mark Coates, and Milica Popović. An early clinical study of time-domain microwave radar for breast health monitoring. *IEEE Transactions on Biomedical Engineering*, 63(3):530–539, 2016.

[50] Alan W Preece, Ian Craddock, Mike Shere, Lyn Jones, and Helen L Winton. Maria m4: clinical evaluation of a prototype ultrawideband radar scanner for breast cancer detection. *Journal of Medical Imaging*, 3(3):033502, 2016.

[51] Yoshihiko Kuwahara, Saori Miura, Yusuke Nishina, Kaishi Mukumoto, Hiroyuki Ogura, and Harumi Sakahara. Clinical test of microwave mammography. In *2013 IEEE Antennas and Propagation Society International Symposium (APSURSI)*, pages 2028–2029. IEEE, 2013.

[52] Yoshihiko Kuwahara. Microwave imaging for early breast cancer detection. *Breast Imaging: New Perspectives in*, page 45, 2017.

[53] Fan Yang, Lin Sun, Zhenhua Hu, Huihai Wang, Dan Pan, Rui Wu, Xiaofeng Zhang, Yifan Chen, and Qingfeng Zhang. A large-scale clinical trial of radar-based microwave breast imaging for asian women: Phase i. In *2017 IEEE International Symposium on Antennas and Propagation & USNC/URSI National Radio Science Meeting*, pages 781–783. IEEE, 2017.

[54] Hang Song, Shinsuke Sasada, Takayuki Kadoya, Morihito Okada, Koji Arihiro, Xia Xiao, and Takamaro Kikkawa. Detectability of breast tumor by a hand-held impulse-radar detector: performance evaluation and pilot clinical study. *Scientific reports*, 7(1):16353, 2017.

[55] Soumya Prakash Rana, Maitreyee Dey, Gianluigi Tiberi, Lorenzo Sani, Alessandro Vispa, Giovanni Raspa, Michele Duranti, Mohammad Ghavami, and Sandra Dudley. Machine learning approaches for automated lesion detection in microwave breast imaging clinical data. *Scientific reports*, 9(1):10510, 2019.

[56] Earl Zastrow, Shakti K Davis, and Susan C Hagness. Safety assessment of breast cancer detection via ultrawideband microwave radar operating in pulsed-radiation mode. *Microwave and Optical Technology Letters*, 49(1):221–225, 2007.

[57] David W Winters, Essex J Bond, Barry D Van Veen, and Susan C Hagness. Estimation of the frequency-dependent average dielectric properties of breast tissue using a time-domain inverse scattering technique. *IEEE Transactions on Antennas and Propagation*, 54(11):3517–3528, 2006.

[58] UWCEM. Breast phantom repository@ONLINE, August 2017.

[59] E Zastrow, SK Davis, M Lazebnik, F Kelcz, BD Van Veem, and SC Hagness. Database of 3d grid-based numerical breast phantoms for use in computational electromagnetics simulations@ONLINE, 2017.

[60] CST. Computer simulation technology. cst computer simulation technology ag@ONLINE, September 2017.

[61] eHealthMD. Breast anatomy@ONLINE.

[62] DT Ramsay, JC Kent, RA Hartmann, and PE Hartmann. Anatomy of the lactating human breast redefined with ultrasound imaging. *Journal of anatomy*, 206(6):525–534, 2005.

[63] David M Pozar. *Microwave engineering*. John Wiley & Sons, 2009.

[64] Natalia K Nikolova. Microwave imaging for breast cancer. *IEEE microwave magazine*, 12(7):78–94, 2011.

[65] SS Chaudhary, RK Mishra, Arvind Swarup, and Joy M Thomas. Dielectric properties of normal & malignant human breast tissues at radiowave & microwave frequencies. 1984.

[66] Andrzej J Surowiec, Stanislaw S Stuchly, J Robin Barr, and AASA Swarup. Dielectric properties of breast carcinoma and the surrounding tissues. *IEEE Transactions on Biomedical Engineering*, 35(4):257–263, 1988.

[67] AM Campbell and DV Land. Dielectric properties of female human breast tissue measured in vitro at 3.2 ghz. *Physics in medicine and biology*, 37(1):193, 1992.

[68] William T Joines, Yang Zhang, Chenxing Li, and Randy L Jirtle. The measured electrical properties of normal and malignant human tissues from 50 to 900 mhz. *Medical physics*, 21(4):547–550, 1994.

[69] Jin Wook Choi, Jeiwon Cho, Yangsoo Lee, Jounghwa Yim, Byoungjoong Kang, Ki Keun Oh, Woo Hee Jung, Hee Jung Kim, Changyul Cheon, Hy-De Lee, et al. Microwave detection of metastasized breast cancer cells in the lymph node; potential application for sentinel lymphadenectomy. *Breast cancer research and treatment*, 86(2):107–115, 2004.

[70] Mariya Lazebnik, Dijana Popovic, Leah McCartney, Cynthia B Watkins, Mary J Lindstrom, Josephine Harter, Sarah Sewall, Travis Ogilvie, Anthony Magliocco, Tara M Breslin, et al. A large-scale study of the ultrawideband microwave dielectric properties of normal, benign and malignant breast tissues obtained from cancer surgeries. *Physics in medicine and biology*, 52(20):6093, 2007.

[71] Ryan J Halter, Tian Zhou, Paul M Meaney, Alex Hartov, Richard J Barth Jr, Kari M Rosenkranz, Wendy A Wells, Christine A Kogel, Andrea Borsic, Elizabeth J Rizzo, et al. The correlation of in vivo and ex vivo tissue dielectric properties to validate electromagnetic breast imaging: initial clinical experience. *Physiological measurement*, 30(6):S121, 2009.

[72] Takumi Sugitani, Shin-ichi Kubota, Shin-ichiro Kuroki, Kenta Sogo, Koji Arihiro, Morihito Okada, Takayuki Kadoya, Michihiro Hide, Miyo Oda, and Takamaro Kikkawa. Complex permittivities of breast tumor tissues obtained from cancer surgeries. *Applied Physics Letters*, 104(25):253702, 2014.

[73] A Martellosio, M Pasian, M Bozzi, L Perregrini, A Mazzanti, F Svelto, PE Summers, G Renne, and M Bellomi. 0.5–50 ghz dielectric characterisation of breast cancer tissues. *Electronics Letters*, 51(13):974–975, 2015.

[74] Andrea Martellosio, Marco Pasian, Maurizio Bozzi, Luca Perregrini, Andrea Mazzanti, Francesco Svelto, Paul Eugene Summers, Giuseppe Renne, Lorenzo Preda, and Massimo Bellomi. Dielectric properties characterization from 0.5 to 50 ghz of breast cancer tissues. *IEEE Transactions on Microwave Theory and Techniques*, 65(3):998–1011, 2017.

[75] Yiou Cheng and Minghuan Fu. Dielectric properties for non-invasive detection of normal, benign, and malignant breast tissues using microwave theories. *Thoracic cancer*, 9(4):459–465, 2018.

[76] Mousa Hussein, Falah Awwad, Dwija Jithin, Husain El Hasasna, Khawlah Athamneh, and Rabah Iratni. Breast cancer cells exhibits specific dielectric signature in vitro using the open-ended coaxial probe technique from 200 mhz to 13.6 ghz. *Scientific reports*, 9(1):4681, 2019.

[77] JR Mallard and DG Lawn. Dielectric absorption of microwaves in human tissues. *Nature*, 213(5071):28–30, 1967.

[78] Saqib Salahuddin, Emily Porter, Paul M Meaney, and Martin O'Halloran. Effect of logarithmic and linear frequency scales on parametric modelling of tissue dielectric data. *Biomedical physics & engineering express*, 3(1):015020, 2017.

[79] Declan O'Loughlin, Martin O'Halloran, Brian M Moloney, Martin Glavin, Edward Jones, and M Adnan Elahi. Microwave breast imaging: Clinical advances and remaining challenges. *IEEE Transactions on Biomedical Engineering*, 65(11):2580–2590, 2018.

[80] Paul M Meaney, Andrew P Gregory, Neil R Epstein, and Keith D Paulsen. Microwave open-ended coaxial dielectric probe: interpretation of the sensing volume re-visited. *BMC medical physics*, 14(1):3, 2014.

[81] Emily Porter and Martin O'Halloran. Investigation of histology region in dielectric measurements of heterogeneous tissues. *IEEE Transactions on Antennas and Propagation*, 65(10):5541–5552, 2017.

[82] Saqib Salahuddin, Alessandra La Gioia, Muhammad Adnan Elahi, Emily Porter, Martin O'Halloran, and Atif Shahzad. Comparison of in-vivo and ex-vivo dielectric properties of biological tissues. In *2017 International Conference on Electromagnetics in Advanced Applications (ICEAA)*, pages 582–585. IEEE, 2017.

[83] American College of Radiology et al. American college of radiology. breast imaging reporting and data system, 2013.

[84] Earl Zastrow, Shakti K Davis, Mariya Lazebnik, Frederick Kelcz, Barry D Van Veen, and Susan C Hagness. Development of anatomically realistic numerical breast phantoms with accurate dielectric properties for modeling microwave interactions with the human breast. *IEEE Transactions on Biomedical Engineering*, 55(12):2792–2800, 2008.

[85] MATLAB. Matlab program@ONLINE, September 2017.

[86] Mariya Lazebnik, Leah McCartney, Dijana Popovic, Cynthia B Watkins, Mary J Lindstrom, Josephine Harter, Sarah Sewall, Anthony Magliocco, John H Booske, Michal Okoniewski, et al. A large-scale study of the ultrawideband microwave dielectric properties of normal breast tissue obtained from reduction surgeries. *Physics in medicine and biology*, 52(10):2637, 2007.

[87] Steven M Anlage, Vladimir V Talanov, and Andrew R Schwartz. Principles of near-field microwave microscopy. In *Scanning probe microscopy*, pages 215–253. Springer, 2007.

[88] Richard A Kleismit and Marian K Kazimierczuk. Evanescent microwave sensor scanning for detection of sub-surface defects in wires. In *Electrical Insulation Conference and Electrical Manufacturing & Coil Winding Conference, 2001. Proceedings*, pages 245–250. IEEE, 2001.

[89] Zhao Ren, Muhammed S Boybay, and Omar M Ramahi. Near-field probes for subsurface detection using split-ring resonators. *IEEE Transactions on Microwave Theory and Techniques*, 59(2):488–495, 2011.

[90] Wael Saleh and Nasser Qaddoumi. Potential of near-field microwave imaging in breast cancer detection utilizing tapered rectangular waveguide probes. *Computers & Electrical Engineering*, 35(4):587–593, 2009.

[91] Huiyu Zhang, Soon Yim Tan, and Hong Siang Tan. A novel method for microwave breast cancer detection. In *Microwave Conference, 2008. APMC 2008. Asia-Pacific*, pages 1–4. IEEE, 2008.

[92] Veronika Gazhonova. *3D Automated Breast Volume Sonography: A Practical Guide*. Springer, 2016.

[93] Jeon-Hor Chen, Siwa Chan, Dah-Cherng Yeh, Peter T Fwu, Muqing Lin, and Min-Ying Su. Response of bilateral breasts to the endogenous hormonal fluctuation in a menstrual cycle evaluated using 3d mri. *Magnetic resonance imaging*, 31(4):538–544, 2013.

[94] Mark Richardson. Principal component analysis. *URL: http://people. maths. ox. ac. uk/richardsonm/SignalProcPCA. pdf (last access: 3.5. 2013). Aleš Hladnik Dr., Ass. Prof., Chair of Information and Graphic Arts Technology, Faculty of Natural Sciences and Engineering, University of Ljubljana, Slovenia ales. hladnik@ ntf. uni-lj. si*, 2009.

[95] Hervé Abdi and Lynne J Williams. Principal component analysis. *Wiley interdisciplinary reviews: computational statistics*, 2(4):433–459, 2010.

[96] Richard Torrealba-Melendez, Jose Luis Olvera-Cervantes, and Alonso Corona-Chavez. Uwb microwave radar imaging for detection and discrimination of benign and malignant breast tumors using circularly polarized antennas. In *Wireless and Microwave Technology Conference (WAMICON), 2014 IEEE 15th Annual*, pages 1–3. IEEE, 2014.

[97] Yu Yuan, Cory Wyatt, Paolo Maccarini, Paul Stauffer, Oana Craciunescu, James MacFall, Mark Dewhirst, and Shiva K Das. A heterogeneous human tissue mimicking phantom for rf heating and mri thermal monitoring verification. *Physics in Medicine & Biology*, 57(7):2021, 2012.

[98] Emily Porter, Jules Fakhoury, Razvan Oprisor, Mark Coates, and Milica Popović. Improved tissue phantoms for experimental validation of microwave breast cancer detection. In *Antennas and Propagation (EuCAP), 2010 Proceedings of the Fourth European Conference on*, pages 1–5. IEEE, 2010.

[99] Mariya Lazebnik, Ernest L Madsen, Gary R Frank, and Susan C Hagness. Tissue-mimicking phantom materials for narrowband and ultrawideband microwave applications. *Physics in Medicine & Biology*, 50(18):4245, 2005.

[100] Ian T Jolliffe and Jorge Cadima. Principal component analysis: a review and recent developments. *Phil. Trans. R. Soc. A*, 374(2065):20150202, 2016.

[101] Fan Yang, Lin Sun, Zhenhua Hu, Huihai Wang, Dan Pan, Rui Wu, Xiaofeng Zhang, Yifan Chen, and Qingfeng Zhang. A large-scale clinical trial of radar-based microwave breast imaging for asian women:

Phase i. In *2017 IEEE International Symposium on Antennas and Propagation & USNC/URSI National Radio Science Meeting*, pages 781–783. IEEE, 2017.

[102] Ikram Khuda. A comprehensive review on design and development of human breast phantoms for ultra-wide band breast cancer imaging systems. *Engineering Journal*, 21(3):183–206, Jun. 2017.

[103] K. E. Michaelsen, V. Krishnaswamy, A. Shenoy, E. Jordan, B. Pogue, and K. D. Paulsen. Anthropomorphic breast phantoms with physiological water, lipid, and hemoglobin content for near-infrared spectral tomography. *Journal of biomedical optics*, 19(2):026012, 2014.

[104] S Raghavan and V Rajeshkumar. An overview of metamaterials in biomedical applications. In *PIERS Proceedings*, pages 368–371, 2013.

[105] Yohan Lee, Sun-Je Kim, Hyeonsoo Park, and Byoungho Lee. Metamaterials and metasurfaces for sensor applications. *Sensors*, 17(8):1726, 2017.

[106] Z Zhu, H Liu, D Wang, YX Li, CY Guan, H Zhang, and JH Shi. Coherent control of double deflected anomalous modes in ultrathin trapezoid-shaped slit metasurface. *Scientific reports*, 6:37476, 2016.

[107] Maged A Aldhaeebi, Thamer S Almoneef, Abdulbaset Ali, Zhao Ren, and Omar M Ramahi. Near field breast tumor detection using ultra-narrow band probe with machine learning techniques. *Scientific Report*, 8(1):12607.

[108] Maged A Aldhaeebi, Thamer S Almoneef, Hussein Attia, and Omar M Ramahi. Electrically small magnetic probe with pca for near-field microwave breast tumors detection. *Progress In Electromagnetics Research*, 84:177–186.

[109] Maged A Aldhaeebi, Thamer S Almoneef, Hussein Attia, and Omar M Ramahi. Near-field microwave loop array sensor for breast tumor detection. *IEEE Sensors Journal*, 19(24):11867–11872, 2019.

[110] Md Mahmud, Mohammad Islam, Norbahiah Misran, Ali Almutairi, and Mengu Cho. Ultra-wideband (uwb) antenna sensor based microwave breast imaging: A review. *Sensors*, 18(9):2951, 2018.

[111] Malyhe Jalilvand, Xuyang Li, Lukasz Zwirello, and Thomas Zwick. Ultra wideband compact near-field imaging system for breast cancer detection. *IET Microwaves, Antennas & Propagation*, 9(10):1009–1014, 2015.

[112] Mahrukh Khan and Deb Chatteqee. Uwb microwave sensor array characterization for early detection of breast cancer. In *Applied Electromagnetics Conference (AEMC), 2015 IEEE*, pages 1–2. IEEE, 2015.

[113] Declan O'Loughlin, Martin O'Halloran, Brian M Moloney, Martin Glavin, Edward Jones, and M Adnan Elahi. Microwave breast imaging: Clinical advances and remaining challenges. *IEEE Transactions on Biomedical Engineering*, 65(11):2580–2590, 2018.

[114] Elise C Fear, Xu Li, Susan C Hagness, and Maria A Stuchly. Confocal microwave imaging for breast cancer detection: Localization of tumors in three dimensions. *IEEE Transactions on Biomedical Engineering*, 49(8):812–822, 2002.

[115] NR Epstein, PM Meaney, and KD Paulsen. 3d parallel-detection microwave tomography for clinical breast imaging. *Review of Scientific Instruments*, 85(12):124704, 2014.

[116] M Klemm, D Gibbins, J Leendertz, T Horseman, AW Preece, R Benjamin, and IJ Craddock. Development and testing of a 60-element uwb

conformal array for breast cancer imaging. In *Antennas and Propagation (EUCAP), Proceedings of the 5th European Conference on*, pages 3077–3079. IEEE, May 2011.

[117] Robert Trevethan. Sensitivity, specificity, and predictive values: foundations, pliabilities, and pitfalls in research and practice. *Frontiers in public health*, 5:307, 2017.

[118] Rajul Parikh, Annie Mathai, Shefali Parikh, G Chandra Sekhar, and Ravi Thomas. Understanding and using sensitivity, specificity and predictive values. *Indian journal of ophthalmology*, 56(1):45, 2008.

[119] D Byrne, M O'Halloran, E Jones, and M Glavin. Support vector machine-based ultrawideband breast cancer detection system. *Journal of Electromagnetic Waves and Applications*, 25(13):1807–1816, 2011.

[120] Dallan Byrne, Martin O'Halloran, Martin Glavin, and Edward Jones. Breast cancer detection based on differential ultrawideband microwave radar. *Progress In Electromagnetics Research M*, 20:231–242, 2011.

[121] Saleh Ali AlShehri, Sabira Khatun, Adznan B Jantan, Raja Syamsul Azmir Raja Abdullah, Rozi Mahmud, and Zaiki Awang. Experimental breast tumor detection using nn-based uwb imaging. *Progress In Electromagnetics Research*, 111:447–465, 2011.

[122] Raquel C Conceição, Hugo Medeiros, Martin ÓHalloran, Diego Rodriguez-Herrera, Daniel Flores-Tapia, and Stephen Pistorius. Svm-based classification of breast tumour phantoms using a uwb radar prototype system. In *General Assembly and Scientific Symposium (URSI GASS), 2014 XXXIth URSI*, pages 1–4. IEEE, 2014.

[123] Alireza Osareh and Bita Shadgar. Machine learning techniques to diagnose breast cancer. In *Health Informatics and Bioinformatics (HI-*

*BIT), 2010 5th International Symposium on*, pages 114–120. IEEE, 2010.

[124] Adam Santorelli, Yunpeng Li, Emily Porter, Milica Popović, and Mark Coates. Investigation of classification algorithms for a prototype microwave breast cancer monitor. In *Antennas and Propagation (EuCAP), 2014 8th European Conference on*, pages 320–324. IEEE, 2014.

[125] Marggie Jones, Dallan Byrne, Brian McGinley, Fearghal Morgan, Martin Glavin, Edward Jones, Martin ÓHalloran, and Raquel C Conceição. Classification and monitoring of early stage breast cancer using ultra wide band radar. In *The Eighth International Conference on Systems (ICONS), International Academy, Research, and Industry Association (IARIA)*, pages 46–51, 2013.

[126] RC Conceicao, M ÓHalloran, M Glavin, and E Jones. Evaluation of features and classifiers for classification of early-stage breast cancer. *Journal of Electromagnetic Waves and Applications*, 25(1):1–14, 2011.

[127] Mohammad Taheri. Enhanced breast cancer classification with automatic thresholding using support vector machine and harris corner detection. 2017.

[128] Raquel Cruz Conceicao, Martin ÓHalloran, Edward Jones, and Martin Glavin. Investigation of classifiers for early-stage breast cancer based on radar target signatures. *Progress In Electromagnetics Research*, 105:295–311, 2010.

[129] Shakti K Davis, Barry D Van Veen, Susan C Hagness, and Frederick Kelcz. Breast tumor characterization based on ultrawideband microwave backscatter. *IEEE transactions on biomedical engineering*, 55(1):237–246, 2008.

[130] Paolo Rocca, Federico Viani, Massimo Donelli, Manuel Benedetti, and Andrea Massa. An integration between svm classifiers and multi-resolution techniques for early breast cancer detection. In *Antennas and Propagation Society International Symposium, 2008. AP-S 2008. IEEE*, pages 1–4. IEEE, 2008.

[131] Mehmet Fatih Akay. Support vector machines combined with feature selection for breast cancer diagnosis. *Expert systems with applications*, 36(2):3240–3247, 2009.

[132] Saleh Ali AlShehri and Sabira Khatun. Uwb imaging for breastr cancer detection using neural network. *Progress In Electromagnetics Research C*, 7:79–93, 2009.

[133] Y Rejani and S Thamarai Selvi. Early detection of breast cancer using svm classifier technique. *arXiv preprint arXiv:0912.2314*, 2009.

[134] Federico Viani, Paul Meaney, Paolo Rocca, Renzo Azaro, Massimo Donelli, Giacomo Oliveri, and Andrea Massa. Numerical validation and experimental results of a multi-resolution svm-based classification procedure for breast imaging. In *Antennas and Propagation Society International Symposium, 2009. APSURSI'09. IEEE*, pages 1–4. IEEE, 2009.

[135] RC Conceição, M ÓHalloran, D Byrne, E Jones, and M Glavin. Tumor classification using radar target signatures. In *PIERS Proceedings*, pages 346–349, 2010.

[136] RR Janghel, Anupam Shukla, Ritu Tiwari, and Rahul Kala. Breast cancer diagnosis using artificial neural network models. In *Information Sciences and Interaction Sciences (ICIS), 2010 3rd International Conference on*, pages 89–94. IEEE, 2010.

[137] Raquel Cruz Conceição, Martin ÓHalloran, Martin Glavin, and Edward Jones. Support vector machines for the classification of early-stage breast cancer based on radar target signatures. *Progress In Electromagnetics Research B*, 23:311–327, 2010.

[138] Raquel Cruz Conceição, Martin ÓHalloran, Edward Jones, and Martin Glavin. Investigation of classifiers for early-stage breast cancer based on radar target signatures. *Progress In Electromagnetics Research*, 105:295–311, 2010.

[139] Younis M Abbosh, Ammar F Yahya, and Amin Abbosh. Neural networks for the detection and localization of breast cancer. In *Communications and Information Technology (ICCIT), 2011 International Conference on*, pages 156–159. IEEE, 2011.

[140] Saleh Ali AlShehri, Sabira Khatun, Adznan B Jantan, Raja Syamsul Azmir Raja Abdullah, Rozi Mahmud, and Zaiki Awang. Experimental breast tumor detection using nn-based uwb imaging. *Progress In Electromagnetics Research*, 111:447–465, 2011.

[141] Raquel Cruz Conceição, Martin ÓHalloran, Martin Glavin, and Edward Jones. Effects of dielectric heterogeneity in the performance of breast tumour classifiers. *Progress In Electromagnetics Research M*, 17:73–86, 2011.

[142] Martin ÓHalloran, Seamus Cawley, Brian McGinley, Raquel Cruz Conceicao, Fearghal Morgan, Edward Jones, and Martin Glavin. Evolving spiking neural network topologies for breast cancer classification in a dielectrically heterogeneous breast. *Progress In Electromagnetics Research Letters*, 25:153–162, 2011.

[143] Ammar F Yahya, Younis M Abbosh, and Amin Abbosh. Microwave imaging method employing wavelet transform and neural networks

for breast cancer detection. In *Microwave Conference Proceedings (APMC), 2011 Asia-Pacific*, pages 1418–1421. IEEE, 2011.

[144] U Rajendra Acharya, Eddie Yin-Kwee Ng, Jen-Hong Tan, and S Vinitha Sree. Thermography based breast cancer detection using texture features and support vector machine. *Journal of medical systems*, 36(3):1503–1510, 2012.

[145] M Al Sharkawy, M Sharkas, and D Ragab. Breast cancer detection using support vector machine technique applied on extracted electromagnetic waves. In *ACES*, volume 27, 2012.

[146] Raquel C Conceição, Martin ÓHalloran, Ricardo M Capote, Cláudia S Ferreira, Nuno Matela, Hugo A Ferreira, Martin Glavin, Edward Jones, and Pedro Almeida. Development of breast and tumour models for simulation of novel multimodal pem-uwb technique for detection and classification of breast tumours. In *Nuclear Science Symposium and Medical Imaging Conference (NSS/MIC), 2012 IEEE*, pages 2769–2772. IEEE, 2012.

[147] RC Conceição, H Medeiros, M ÓHalloran, D Rodriguez-Herrera, D Flores-Tapia, and S Pistorius. Initial classification of breast tumour phantoms using a uwb radar prototype. In *Electromagnetics in Advanced Applications (ICEAA), 2013 International Conference on*, pages 720–723. IEEE, 2013.

[148] McGinley B Morgan F Glavin M Jones E ÓHalloran M Conceição Jones M, Byrne D. Classification and monitoring of early stage breast cancer using ultra wideband radar. In *The Eighth International Conference on Systems (ICONS)*, pages 46–51. International Academy, Research, and Industry Association, 2013.

[149] Samaneh Aminikhanghahi, Sung Shin, Wei Wang, Seong H Son, and Soon I Jeon. An optimized support vector machine classifier to ex-

tract abnormal features from breast microwave tomography data. In *Proceedings of the 2014 Conference on Research in Adaptive and Convergent Systems*, pages 111–115. ACM, 2014.

[150] Samaneh Aminikhanghahi, Wei Wang, Sung Shin, Seong H Son, and Soon I Jeon. Effective tumor feature extraction for smart phone based microwave tomography breast cancer screening. In *Proceedings of the 29th Annual ACM Symposium on Applied Computing*, pages 674–679. ACM, 2014.

[151] Blair D Fleet, Jinyao Yan, David B Knoester, Meng Yao, John R Deller, and Erik D Goodman. Breast cancer detection using haralick features of images reconstructed from ultra wideband microwave scans. In *Workshop on Clinical Image-Based Procedures*, pages 9–16. Springer, 2014.

[152] Raquel C Conceição, Hugo Medeiros, Martin ÓHalloran, Diego Rodriguez-Herrera, Daniel Flores-Tapia, and Stephen Pistorius. Svm-based classification of breast tumour phantoms using a uwb radar prototype system. In *General Assembly and Scientific Symposium (URSI GASS), 2014 XXXIth URSI*, pages 1–4. IEEE, 2014.

[153] Adam Santorelli, Emily Porter, Evgeny Kirshin, Yi Jun Liu, and Milica Popovic. Investigation of classifiers for tumor detection with an experimental time-domain breast screening system. *Progress In Electromagnetics Research*, 144:45–57, 2014.

[154] Adam Santorelli, Yunpeng Li, Emily Porter, Milica Popović, and Mark Coates. Investigation of classification algorithms for a prototype microwave breast cancer monitor. In *Antennas and Propagation (EuCAP), 2014 8th European Conference on*, pages 320–324. IEEE, 2014.

[155] Yunpeng Li, Adam Santorelli, Olivier Laforest, and Mark Coates. Cost-sensitive ensemble classifiers for microwave breast cancer detection. In *Acoustics, Speech and Signal Processing (ICASSP), 2015 IEEE International Conference on*, pages 952–956. IEEE, 2015.

[156] Chih-Wei Hsu, Chih-Chung Chang, Chih-Jen Lin, et al. A practical guide to support vector classification. 2003.

[157] Asa Ben-Hur and Jason Weston. A user's guide to support vector machines. In *Data mining techniques for the life sciences*, pages 223–239. Springer, 2010.

[158] Nick Guenther and Matthias Schonlau. Support vector machines. *The Stata Journal*, 16(4):917–937, 2016.

[159] Marti A. Hearst, Susan T Dumais, Edgar Osuna, John Platt, and Bernhard Scholkopf. Support vector machines. *IEEE Intelligent Systems and their applications*, 13(4):18–28, 1998.

[160] Alex M Andrew. An introduction to support vector machines and other kernel-based learning methods by nello christianini and john shawe-taylor. *Robotica*, 18(6):687–689, 2000.

[161] Nusaibah Kh Al-Salihy and Turgay Ibrikci. Classifying breast cancer by using decision tree algorithms. In *Proceedings of the 6th International Conference on Software and Computer Applications*, pages 144–148. ACM, 2017.

[162] E Venkatesan and T Velmurugan. Performance analysis of decision tree algorithms for breast cancer classification. *Indian Journal of Science and Technology*, 8(29):1–8, 2015.

[163] Chintan Shah and Anjali G Jivani. Comparison of data mining classification algorithms for breast cancer prediction. In *2013 Fourth Inter-*

*national Conference on Computing, Communications and Networking Technologies (ICCCNT)*, pages 1–4. IEEE, 2013.